ESA Climate Change Initiative (CCI)

Greenland Ice Sheet (GIS) Essential Climate Variable (ECV)

Product Validation and Intercomparison Report (PVIR)

Science &Project Lead: René Forsberg
DTU Space, Copenhagen, Denmark
rf@space.dtu.dk

Technical Officer: Marcus Engdahl
ESA ESRIN, Frascati, Italy
Marcus.engdahl@esa.int

Consortium:
Danish Meteorological Institute (DMI)
DTU-Space, Department of Geodynamics (DTU-GDK)
DTU-Space, Department of Microwaves and Remote Sensing (DTU-MRS)
ENVironmental Earth Observation IT GmbH (ENVEO)
Geological Survey of Denmark and Greenland (GEUS)
Nansen Environmental and Remote Sensing Center (NERSC)
Niels Bohr Institute (NBI)
Science [&] Technology AS (S[&]T)
TechnischeUniversität Dresden (TUDr)
University of Leeds, School of Earth and Environment (UL)

To be cited as:

GIS_cci Consortium,et al., Product Validation and Intercomparison Report (PVIR) *for the Greenland_Ice_Sheet_cciproject of ESA's Climate Change Initiative, version 3.0, 25 July 2018.*

Available from: http://www.esa-icesheets-cci.org/

Signatures page

Prepared by	Louise Sørensen Lead Author	2018-07-25
Issued by	Kenneth Hauglund Project Manager	2018-07-25
Checked by	René Forsberg Science Leader	2018-07-25
Approved by	Marcus Engdahl ESA Technical Officer	

Table of Contents

Change Log

Issue	Author	Affected Section	Reason/Description	Status
0.1	D. Evensberget	All	Created Skeleton Document.	Released to consortium
1.2	M. Langer Andersen	All	Finished version	Sent to S[&]T 8/4/2015
1.3	D. Evensberget	All	Minor edits	Released to ESA
1.4	M. Langer Andersen	Section 2.5 Table 2-1 Section 3.1.3.1.3 Figure 12 Section 4.4.1.8 Figure 17	Added note on REAPER availability Removed outdated description, Indicated radar sensor for time periods Repaired mangled symbols in formula Added note on GPS uncertainties Corrected misprint in image caption Corrected image caption	Released to ESA
2.0	Louise Sørensen	1.1, 1.2, 1.3 2.5 and 2.6 6 All	Updated for Phase 2, Year 1: Included title and text for ref. to Phase 2 contract and SoW, and updated applicable and reference documents Added section on SEC Cryosat validation with recommendations Added chapter 6 for GMB Updated typography/ error corrections	Released to ESA on 2016-06-20
2.1	Louise Sørensen	2.5, Figure 2.5-1 5.6	Updated after ESA review: Enlarged Figure 2.5-1 for readability Added description on recommended improvements for GLL	Released to ESA on 2016-09-28
2.2	Louise S. Sørensen Anne M. Solgaard Andreas Groh Louise S. Sørensen	2.5 3.4.3 6.2 6.3 7	Updated for Year 2, data product release March 2017: Included SEC validation figure 2.5-2 with description Included updated validation of time series of Upernavik. Figures updated for GMB. Extended time series compared to v. 2.1. Added reference to publication 2017 Added 2 references to publications 2017	Released to ESA on 2017-06-09
2.3	Louise S. Sørensen Sebastian Simonsen Anne M Solgaard Anders Kusk	2.5 3.4.3	Update acc to ESA RIDs: - Section 2.5 - added a few sentences describing the findings of Simonsen & Sørensen. Included a zoom-in of histogram in Fig. 2.5-2. - Added discussion on the source of the apparent negative bias in the IV measurements.	Released to ESA on 2017-08-16
3.0	Sebastian Simonsen Daniele Fantin	2.6 3.2 2+3+4+5	Update for Year 3: Added section 2.6 AltiKa validation Added section 3.2 on Opt-IV validation Minor editorials and cross-references	Released to ESA on 2018-07-25

Acronyms

Acronym	Explanation
ALOS	Advanced Land Observing Satellite
ASAR	Advanced SAR
ASTER	Advanced Spaceborne Thermal Emission and Reflection Radiometer
CFL	Calving Front Location
DARD	Data Access Requirements Document
DEM	Digital Elevation Model
ECV	Essential Climate Variable
ENVISAT	ESA Environmental satellite
EO	Earth Observation
ERS	European Remote-sensing Satellite
ESA	European Space Agency
ETM+	Enhanced Thematic Mapper plus
GMB	Gravimetric Mass Balance
GIS	Geographic Information System
GIS_cci	Greenland_Ice_Sheet_cci project, short form
GrIS	Greenland Ice Sheet
GLL	Grounding Line Location
GRACE	Gravity Recovery and Climate Experiment
GRACE SDS	GRACE Science Data System
InSAR	Interferometric SAR
IS	Ice Sheets
IV	Ice Velocity
LANDSAT	Land Remote Sensing Satellite
NASA	National Aeronautic and Space Administration
OptIV	Optical Ice Velocity
PALSAR	Phased Array type L-band Synthetic Aperture Radar
PG	Product Generation
PSD	Product Specification Document
PV	Product Validation
PVP	Product Validation Plan
RA	Radar Altimeter
ROI	Region Of Interest
RR	Round Robin
SEC	Surface elevation Change
SAR	Synthetic Aperture Radar
SNR	Signal-to-noise ratio
TM	Thematic Mapper
URD	User Requirement Document

1 Introduction

1.1 Purpose and Scope

This document, the Product Validation and Inter-comparison Report (PVIR), is updated regularly for Phase 2 for the "Greenland_Ice_Sheet_cci" (GIS_cci) project in accordance to Contract [AD1] and Statement of Work [AD2].

This PVIR document is hence based on the Phase 1 PVIR document [RD2] of the "Ice_Sheets_cci" project.

The PVIR document is part of Task 4 Product Generation deliverables, with deliverable id; D4.1.

The GIS_cci Science Team has assessed the ECV data products in the Climate Research Data Package. An intercomparison of the ECV data products with products from other missions and other R&D initiatives has been carried out.

This document describes the results of the validation and inter-comparison exercises, and quantifies accuracy of the derived products against the validation data and comparable alternative satellite-based products generated by international projects.

The PVIR gives a complete report of the activities executed to assessment of the quality of the generated ECV prototype products and the results achieved.

1.2 Document Structure

This document comprises five parts describing each of the parameters of the Ice Sheets Essential Climate Variable (ECV). Each ECV has its own chapter as seen below

- Surface Elevation Change (SEC);
- Ice velocity (IV);
- Calving Front Location (CFL);
- Grounding line location (GLL);
- Gravimetric Mass Balance (GMB).

Each ECV chapter describes includes

- a description of all in situ observations used for product validation;
- a description of alternative products from other initiatives used for product inter-comparison;
- a description of the quality control procedures applied for the selection of the most appropriate validation data and a characterisation of the errors and biases associated to them;
- a detailed analysis of the uncertainty associated to the independent validation data;
- a description of the match-up analyses performed on the derived ECV products against the selected spatially and temporally coincident in situ observations;
- a detailed analysis of the uncertainty of the ECV products with reference to the independent validation data;
- recommendations for fixing errors and/or improving the overall product quality;

In the interest of brevity, references are given to other project documentation when possible.

1.3 Applicable and Reference Documents

Table 1-1: List of Applicable Documents

No	Doc. Id	Doc. Title	Date	Issue/ Revision/ Version
AD1	ESA/Contract No. 4000112228/15/I-NB, and its Appendix 1	Phase 2 of the ESA Climate Change Initiative, Greenland_IceSheet_cci	2015.04.14	-
AD2	CCI-PRGM-EOPS-SW-12-0012 Appendix 2 to contract.	Climate Change Initiative – SoW Phase 2	2014.06.11	Issue 1 Revision 3
AD3	CCI-PRGM-EOPS-TN-12-0031	CCI System Requirements	2013.06.13	Version 1
AD4	CCI-PRGM-EOPS-TN-13-0009	Data Standards Requirements for CCI Data Producers	2013.05.24	Version 1.1

Table 1-2: List of Reference Documents

No	Doc. Id	Doc. Title	Date	Issue/ Revision/ Version
RD1	ESRIN/Contract No. 4000104815/11/I-NB	Phase 1 of the ESA Climate Change Initiative, Ice_Sheets_cci	2012.02.	
RD2	ST-DTU-ESA-ISCCI-PVIR-001	Product Validation and Inter-comparison Report (PVIR), for Phase 1	2015.05.27	1.4
RD3	ST-DTU-ESA-GISCCI-URD-001	User Requirement Document (URD)		
RD4	ST-DTU-ESA-GISCCI-PSD-001	Product Specification Document (PSD)		
RD5	ST-DTU-ESA-GISCCI-DARD-001	Data Access Requirement Document (DARD)		
RD6a	ST-DTU-ESA-GISCCI-ATBD-001	Algorithm Theoretical Baseline Document (ATBD)		
RD6b	ST-DTU-ESA-GISCCI-ATBD-002	Algorithm Theoretical Baseline Document (ATBD), Round Robin Exercise		
RD7	ST-DTU-ESA-GISCCI-CECR-001	Comprehensive Error Characterisation Report (CECR)		
RD8	ST-DTU-ESA-GISCCI-SSD-001	System Specification Document (SSD)		
RD9	ST-DTU-ESA-GISCCI-SVR-001	System Verification Report (SVR)		
RD10	ST-DTU-ESA-GISCCI-PUG-001	Product User Guide (PUG)		
RD11	ST-DTU-ESA-GISCCI-PVIR-001	Product Validation and Inter-comparison Report (PVIR)		
RD12	ST-DTU-ESA-GISCCI-CAR-001	Climate Assessment Report (CAR)		

Note: If not provided, the reference applies to the latest released Issue/Revision/Version

2 Surface Elevation Change (SEC)

This chapter gives a complete report of the activities carried out to assess the quality of the SEC products.

2.1 Sources of independent validation data

This section gives the sources of independent validation data considered for the SEC product validation.

2.1.1 In-situ observational data

Due to the significantly smaller horizontal and vertical errors associated with laser data compared to radar data (Brenner et al., 2007), the SEC trends are validated against elevation change trends derived from airborne laser-scanner data acquired with the Airborne Topographic Mapper (ATM). This is done in NASA's Operation IceBridge (Krabill, 2014). The ATM data are acquired seasonally in the months April to June, and on a nearly yearly basis starting in 1993. The ATM instrument is mounted on-board an aircraft, usually the NASA DC-8 or P3-B, and typically flown at an altitude of 450 m. Given a 30 degree swath width, the laser pulses illuminate an approximately 250 m wide path on the ground. Each pulse has a footprint diameter of 1 to 3 m.

The elevation change trends used in the validation are generated from the IceBridge ATM L1B Elevation and Return Strength (version 2) product (Krabill, 2010). This is done in points where trajectories from two years overlap, either along-track or as cross-overs. The horizontal separation distance for such overlaps to occur is 200 m. This produces elevation changes in discrete points; they have a spatial resolution of 250 x 250 m, and the locations are given as latitude and longitude relative to the WGS-84 ellipsoid.

2.1.2 Alternative products

A number of other products could have been used for validating the Ice_Sheets_cci SEC product: Laser altimetry data from NASA's Ice, Cloud, and land Elevation Satellite (ICESat), or airborne laser-scanner data from the NASA Land, Vegetation, and Ice Sensor (LVIS) or acquired in the Programme for Monitoring of the Greenland Ice Sheet (PROMICE) or ESA's CryoSat Validation Experiment (CryoVEx) campaigns (Blair and Hofton, 2012; Geological Survey of Denmark and Greenland, 2015; Skourup, 2011).

Sørensen et al. (2011) published surface elevation changes over the Greenland Ice Sheet generated from 2003 – 2008 ICESat data. This was done using three different methods, exploiting the satellite's repeat tracks. Method number 3 is found to be optimal, and this was used as the foundation for the repeat-track module developed for the Ice_Sheets_cci SEC derivation. A dataset therefore already exists, which may be usable for validating the SEC trends from radar altimetry data generated here; Sørensen et al. (2015) have generated an ICESat SEC trend for the period 2003 – 2009 and compared with Envisat data in that same period.

The advantage of airborne laser-scanner campaigns is the repeat passes over regions undergoing significant surface changes, both in time and space. Therefore, most such data are acquired over the ice margin, where the largest SEC occurs. Several flights over the interior also exist, making such data feasible for validation of the Ice_Sheets_cci product.

2.2 Selection of independent validation data

This section describes which considerations were taken in selecting the most appropriate validation data.

2.2.1 Validation data selection criteria

The availability of repeat trajectories from airborne laser-scanner data opens to the possibility of generating elevation changes as NASA have done with the ATM data. We decided to use these, as the datasets are publically available, preventing us from introducing errors if we generated such values ourselves. ICESat data were not used due to the radar trends being generated from a similar technique.

2.2.2 Validation data errors and biases

Errors in ATM data arise from a number of sources, such as the pitch, roll, and yaw of the aircraft and instrument, as well as multi-path effects. The latter arises when the direct path of the signal is blocked, thus increasing the travel time of the respective laser pulse and decreasing the resulting elevation estimate. The effect of the aircraft inertial navigation system pitch cancels when averaging and smoothing the observations, while the roll induces a cross-track error. Krabill et al, (2002) considered repeat ATM flights in 1993/1998 and 1994/1999 and found the effects to produce SEC errors up to 1 cm/yr. Atmospheric errors are on the same order of magnitude, and thus vertical errors are typically less than 10 cm.

2.2.3 Validation data uncertainty

The validation data uncertainty are associated with errors from the surface roughness in the area in which the trend is derived, particularly along the ice margin where significant changes may occur within the 200 m distance used for overlapping trajectories. Furthermore, a low number of estimation points reduce the accuracy of the generated trend.

2.3 Validation procedure

The area for the validation is Jakobshavn Isbræ, as stated in the PVP. The validation is carried out using the GRAVSOFT GEOGRID routine (Forsberg and Tscherning, 2008). GEOGRID inputs two datasets, here ATM and radar SEC trends with spatial resolutions of 250 x 250 m and 5 x 5 km, respectively. A given search radius is applied to find ATM data within this distance of each radar point. A weighted means approach, based on the 20 nearest ATM data in each quadrant surrounding the radar point, is used to generate an ATM SEC estimate at this location. The value is subtracted from the radar estimate, and the mean and standard deviation (STD) hereof are computed. So are the minimum and maximum differences.

Three different radii are chosen due to the finer spatial resolution of the ATM data relative to radar data: 500 m, 2 km, and 5 km. Footprints of the latter can be as large as 36 km in diameter, particularly over regions with steep topography, as is the case for the area by Jakobshavn Isbræ (Brenner et al, 1983; Levinsen et al, 2015b).

The Ice_Sheets_cci trends are generated from both ERS and Envisat data, and as five-year running means. Therefore, three different observation periods are analysed: 1998 – 2002, 2001 – 2005, and 2006 – 2010. They reflect the availability of data, so that the former period covers where only ERS-2 data are used, the latter where only Envisat are used, and the middle one where the two datasets are used in conjunction. Due to the overlap of ERS-2 and Envisat data occurring in 2002, the five-year period from 2000 - 2004, or perhaps 1999 - 2003, might have been better. However, due to few ATM data, this was not possible.

The ATM trends for three observation periods are shown in Figure 2-1 to Figure 2-3. A lowering of the Jakobshavn's trunk becomes increasingly pronounced with time.

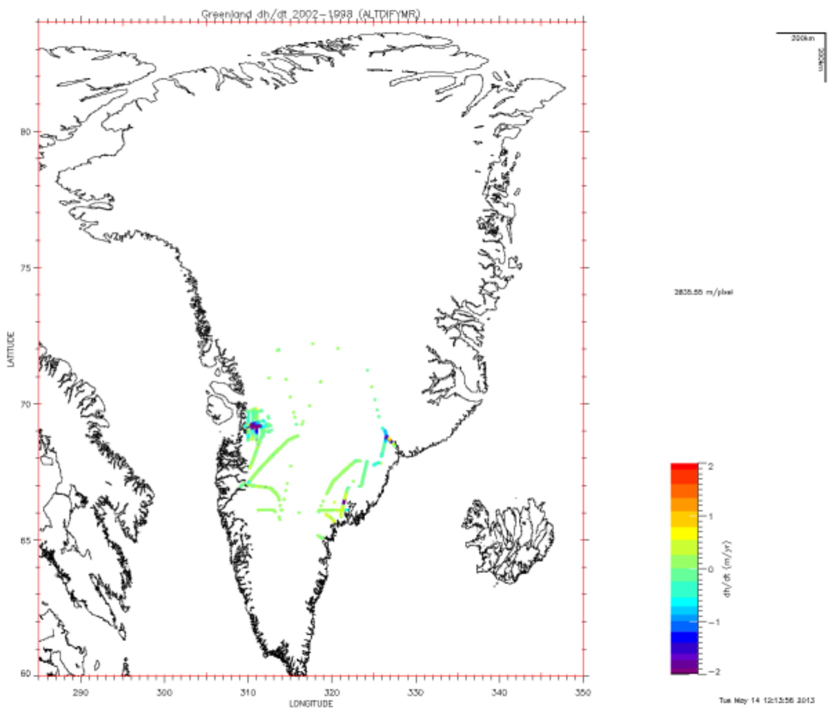

Figure 2-1: ATM surface elevation change trends generated from repeat flights in 1998 and 2002 (Krabill, 2014).

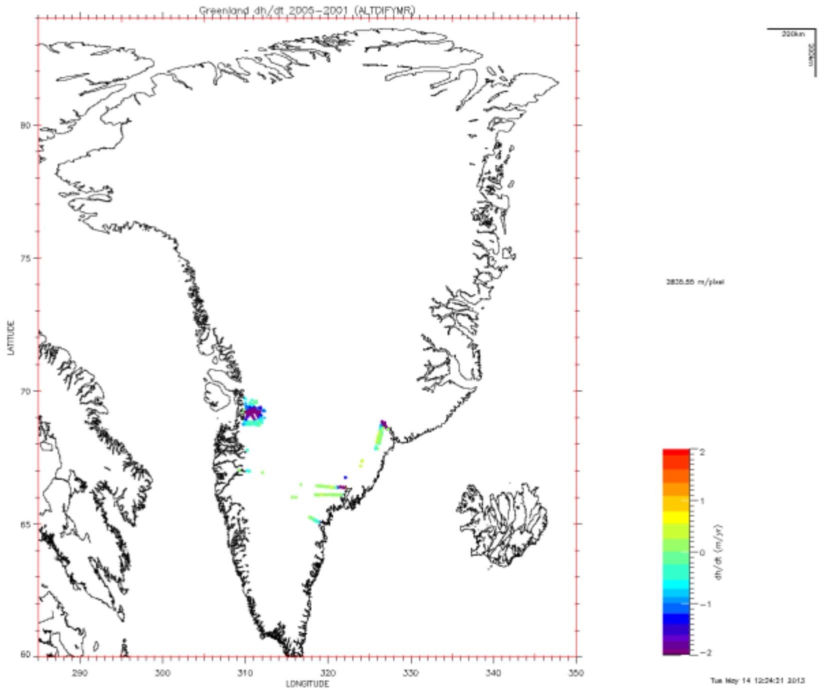

Figure 2-2: ATM surface elevation change trends generated from repeat flights in 2001 and 2005 (Krabill, 2014).

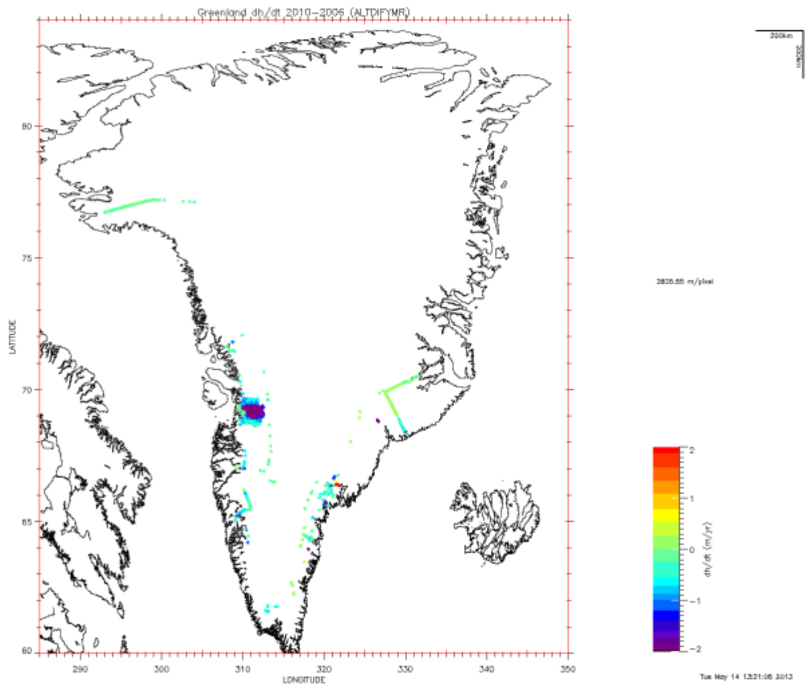

Figure 2-3: ATM surface elevation change trends generated from repeat flights in 2006 and 2010 (Krabill, 2014).

2.4 Validation procedure outcome

The statistics describing the validation results are presented in Table 2-1 to Table 2-3 for the 500 m, 2 km, and 5 km search radii, respectively. The SEC differences are visualised for each time period in Figure 2-4 to Figure 2-6; the values are overlain on the Digital Elevation Model (DEM) developed by Levinsen et al, (2015b).

The statistics reveal, and are affected by, a number of things: The 500 m search radius yields few overlapping points, which significantly biases the statistics towards a higher mean and STD. Furthermore, this radius yields few overlap over the drainage basin where the largest surface changes occur. This may also be attributed to slope-induced errors in radar data (Brenner et al. 1983; Roemer et al. 2007), which relocate the measurements up-slope from nadir and cause surface depressions such as the bottom of troughs and narrow valleys to be missed. The result is few radar measurements inside the glacier trunk. Finally, the statistics are biased by the spatial distribution of ATM SEC points in time. This is particularly noticeable for the period 2001 – 2005, at which point the mass loss over the glacier greatly increased (Howat et al, 2011); an increase, which may not be fully reflected in the statistics due to the few overlaps in space.

All in all, it is clear that the largest differences between radar and validation data exist over the glacier trunk. In spite of this, both the mean and STD are low relative to the min and max offsets. This is particularly noticeable for the 500 m search radius. It shows that radar data are indeed capable of resolving SEC even at the margin of the ice sheet, as also demonstrated by Levinsen et al, (2015a). This is found both for separate ERS-2 and Envisat data, as well as when observations from the two instruments are used in conjunction. The merging thereby seems to have produced reliable SEC trends.

Table 2-1: Validation results where *diff* = $dH/dt_{RA} - dH/dt_{ATM}$. Search radius for overlapping elevation changes: 500 m.

Period	# of points	mean(diff) [m/yr]	STD(diff) [m/yr]	min(diff) [m/yr]	max(diff) [m/yr]
1998 – 2002	23	-0.16	0.25	-0.92	0.16
2001 – 2005	10	0.77	1.10	-0.25	3.62
2006 - 2010	37	0.60	0.82	-0.63	3.53

Table 2-2: Validation results where *diff* = $dH/dt_{RA} - dH/dt_{ATM}$. Search radius for overlapping elevation changes: 2 km.

Period	# of points	mean(diff) [m/yr]	STD(diff) [m/yr]	min(diff) [m/yr]	Max(diff) [m/yr]
1998 – 2002	89	0.21	1.73	-0.92	14.00
2001 – 2005	35	0.63	0.95	-0.25	3.62
2006 - 2010	144	0.56	0.90	-0.68	4.26

Table 2-3: Validation results where *diff* = $dH/dt_{RA} - dH/dt_{ATM}$. Search radius for overlapping elevation changes: 5 km.

Period	# of points	mean(diff) [m/yr]	STD(diff) [m/yr]	min(diff) [m/yr]	max(diff) [m/yr]
1998 – 2002	315	0.10	1.29	-0.92	14.00
2001 – 2005	152	0.49	0.78	-0.27	3.62
2006 - 2010	315	0.36	0.82	-0.82	4.28

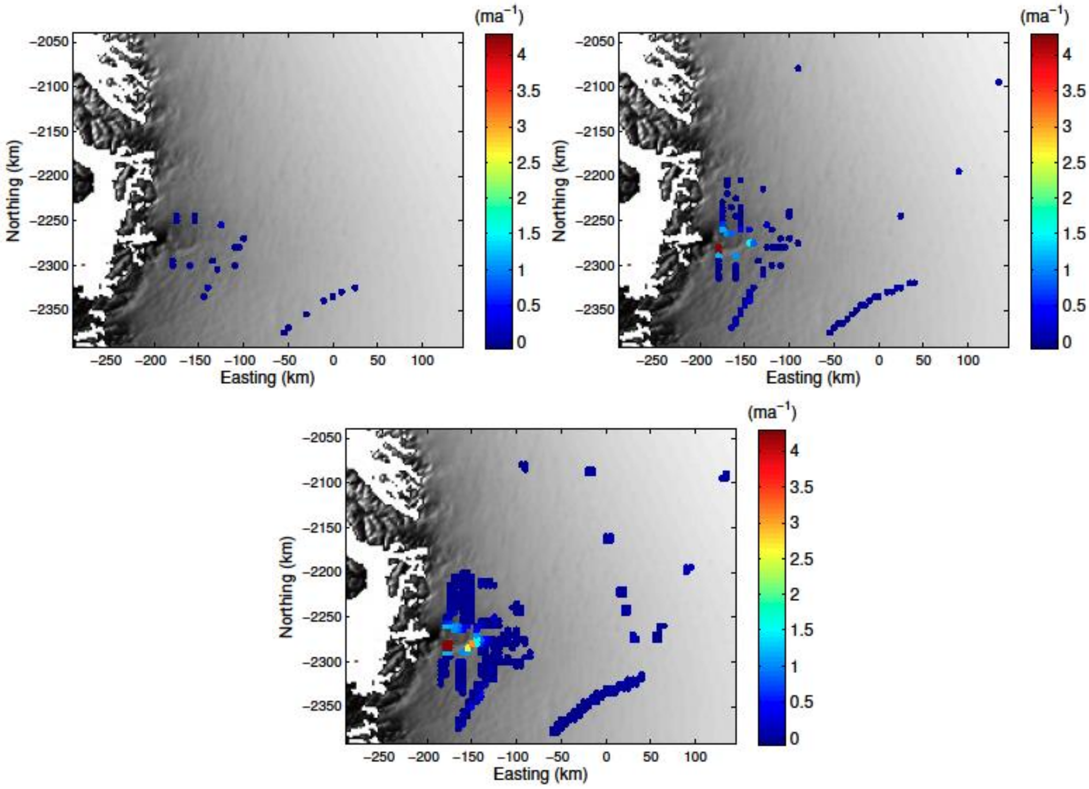

Figure 2-4: Validation results, i.e. *diff* = $dH/dt_{RA} - dH/dt_{ATM}$, over JakobshavnIsbræ for the period 1998 – 2002. Top left: radius = 500 m; top right: radius = 2 km; bottom: radius = 5 km. The values are overlain the DEM developed by Levinsen et al. (2015b).

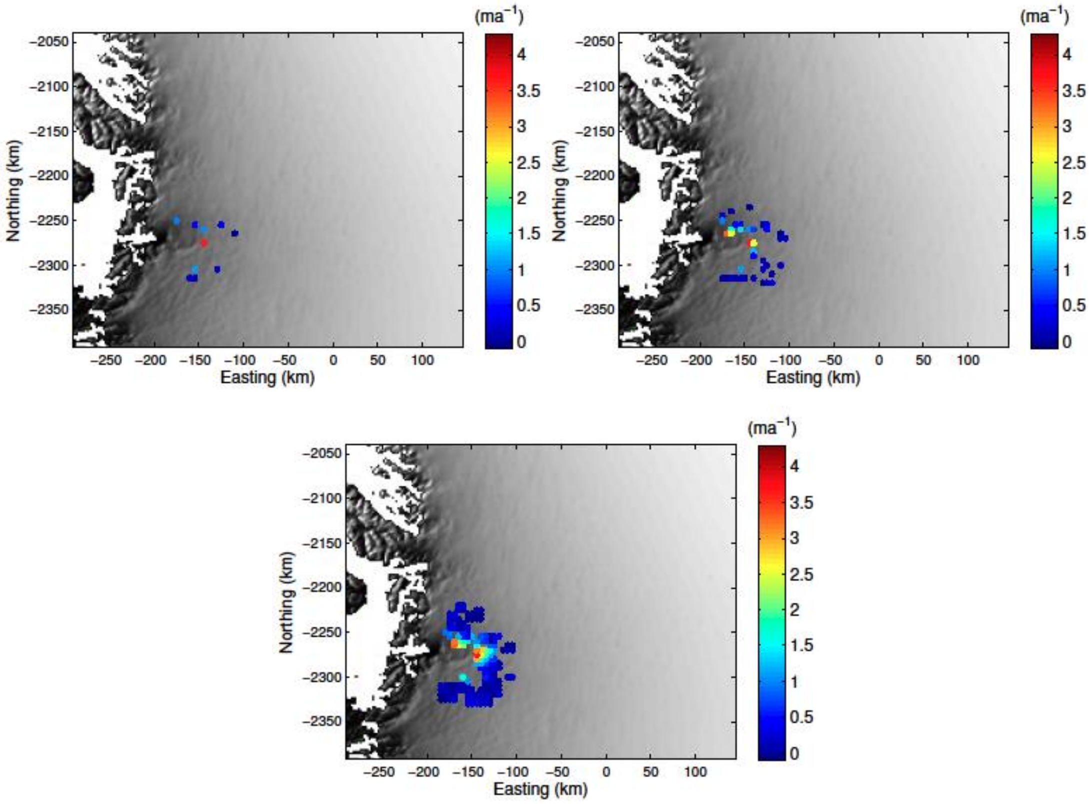

Figure 2-5: Validation results, i.e. *diff* = dH/dt_{RA} – dH/dt_{ATM}, over JakobshavnIsbræ for the period 2001 – 2005. Top left: radius = 500 m; top right: radius = 2 km; bottom: radius = 5 km. The values are overlain the DEM developed by Levinsen et al. (2015b).

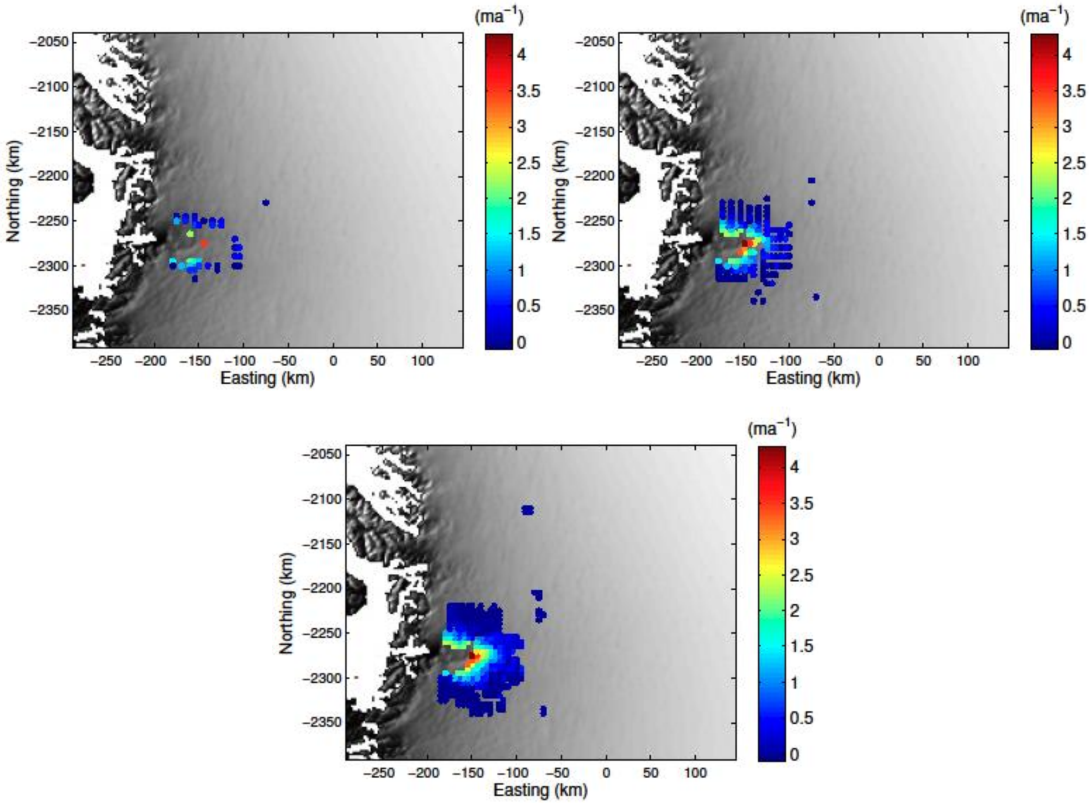

Figure 2-6: Validation results, i.e. *diff* = dH/dt_{RA} – dH/dt_{ATM}, over JakobshavnIsbræ for the period 2006 – 2010. Top left: radius = 500 m; top right: radius = 2 km; bottom: radius = 5 km. The values are overlain the DEM developed by Levinsen et al. (2015b).

2.5 CryoSat validation

CryoSat data have been validated within the recently completed ESA CryoVal Land Ice Study (Cryoval-LI study, ESTEC, Malcolm Davidson). Several validation exercises were carried out for different retrackers/processors for absolute elevations while a round-robin was conducted for elevation changes from and different data sets (from different institutes, including ESA).A summary of all results can be found in the document UoE/UoL_ESA_CRYOLIV_WP5 "Conclusions and Recommendations", dated April 20, 2016.

The CryoVal study generally confirmed that the accuracy of CryoSat data was at the 10-15 cm level rms, with little bias; however some retrackers showed significantly poorer performance. For elevation change accuracies, bias errors are of less importance, and the CryoVal study confirmed CryoSat performance at the few cm/yr level when integrated over larger regions (10's of km). However, melt events, such as the Greenland-wide rainfall of July 2012, are a source of systematic errors which can only partly be recovered with current retrackers. The CCI choice of standards ESA baseline B L2I product as a base for the SEC estimation is therefore upgraded to the improved Baseline C product, currently just released. The performance of the Baseline C product is corresponding to the "best" RR-retracker in the CryoVal study.

An example of the comparison between IceBridge data and the "best" CryoSat results can be seen in Figure 2-7.

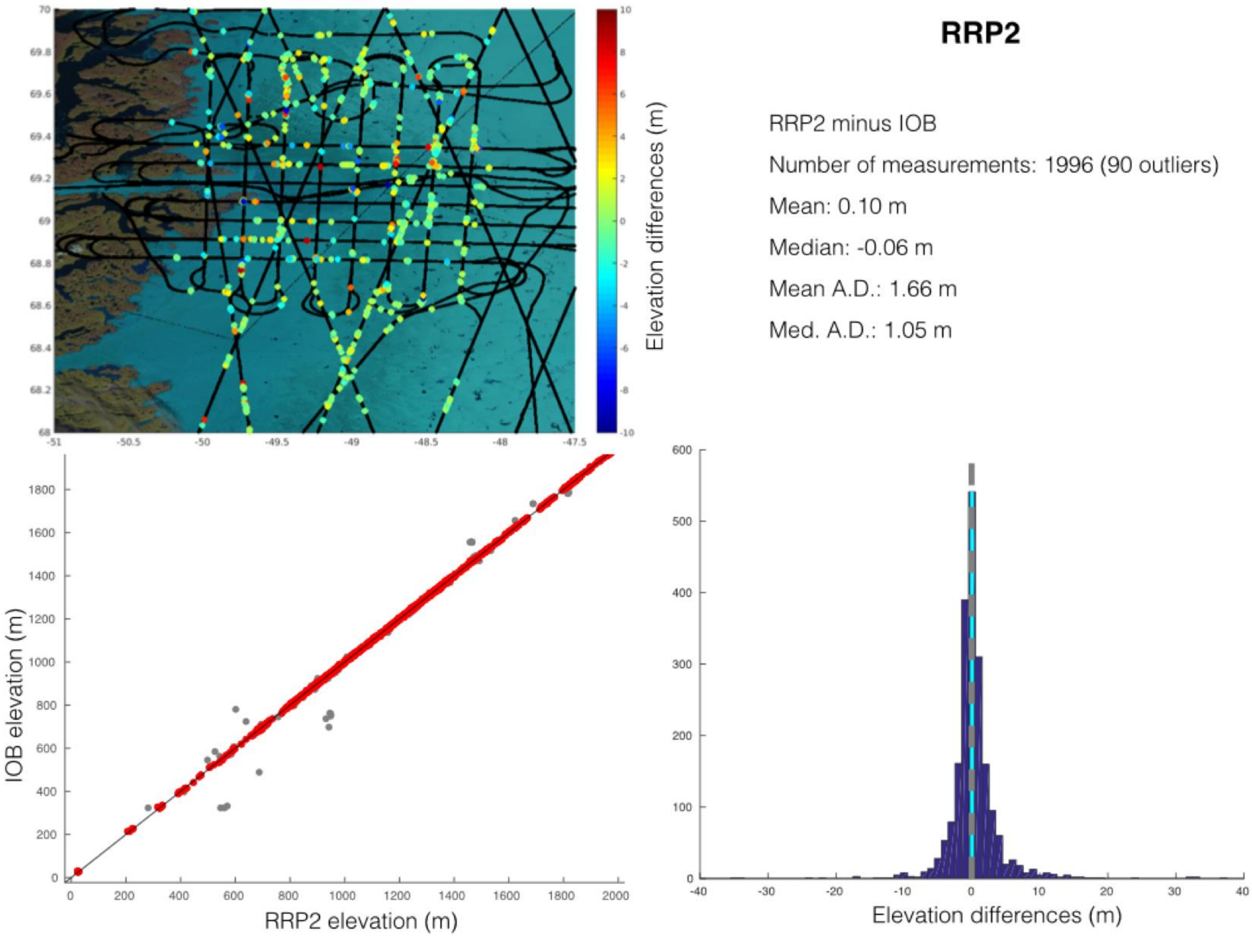

Figure 2-7. Example of fit of CryoSat data relative to OIB elevation data in the Jakobshavn Isbræ region.

Recently, a thorough comparison between elevation changes derived from CS2 and Operation Icebridge data, has been carried out for the entire Greenland Ice Sheet. This work was a crucial part of the algorithm selection for deriving CS2 elevation changes. The work has been presented in Simonsen and Sørensen (2017), and Figure 2-8 shows the differences in elevation changes between the CS2 product and repeated flight lines of Operation Icebridge ATM data (Krabill, 2014). The ATM data are described in Sect 2.3.

In Simonsen and Sørensen (2017), eight different least squares models (LSMs) were applied to derive elevation change from Cryosat-2 data, and the results were validated against Operation IceBridge LiDAR data. The best performing approach for CryoSat-2's Low Resolution Mode area was shown to be one (LSM8) including only the correlation between changes in heights and the Leading edge width (LeW) waveform parameter. Furthermore the best result for the LRM area is found when including a geolocation of the radar return based on the point of closest approach (found in the GIMP DEM (Howat et al., 2014) to do an independent relocation before solving the LSM.

The comparison between the CryoSat-2 and OIB elevation changes found in the SARIn mode area of the Greenland Ice Sheet was found to the LSM (LSM5) which is estimating the elevation change by correcting for correlations between changes in height and both the backscatter and LeW waveform parameters. More details on all the tested LSMs and their performance can be found in Simonsen and Sørensen (2017).

The SEC ECVs from CryoSat-2 in the Greenland Ice Sheet CCI is generated from the LSM5 algorithm for all of Greenland, as this method provides the best performance in an ice-sheet-wide sense. Furthermore, the CCI SEC product is based on baseline C data.

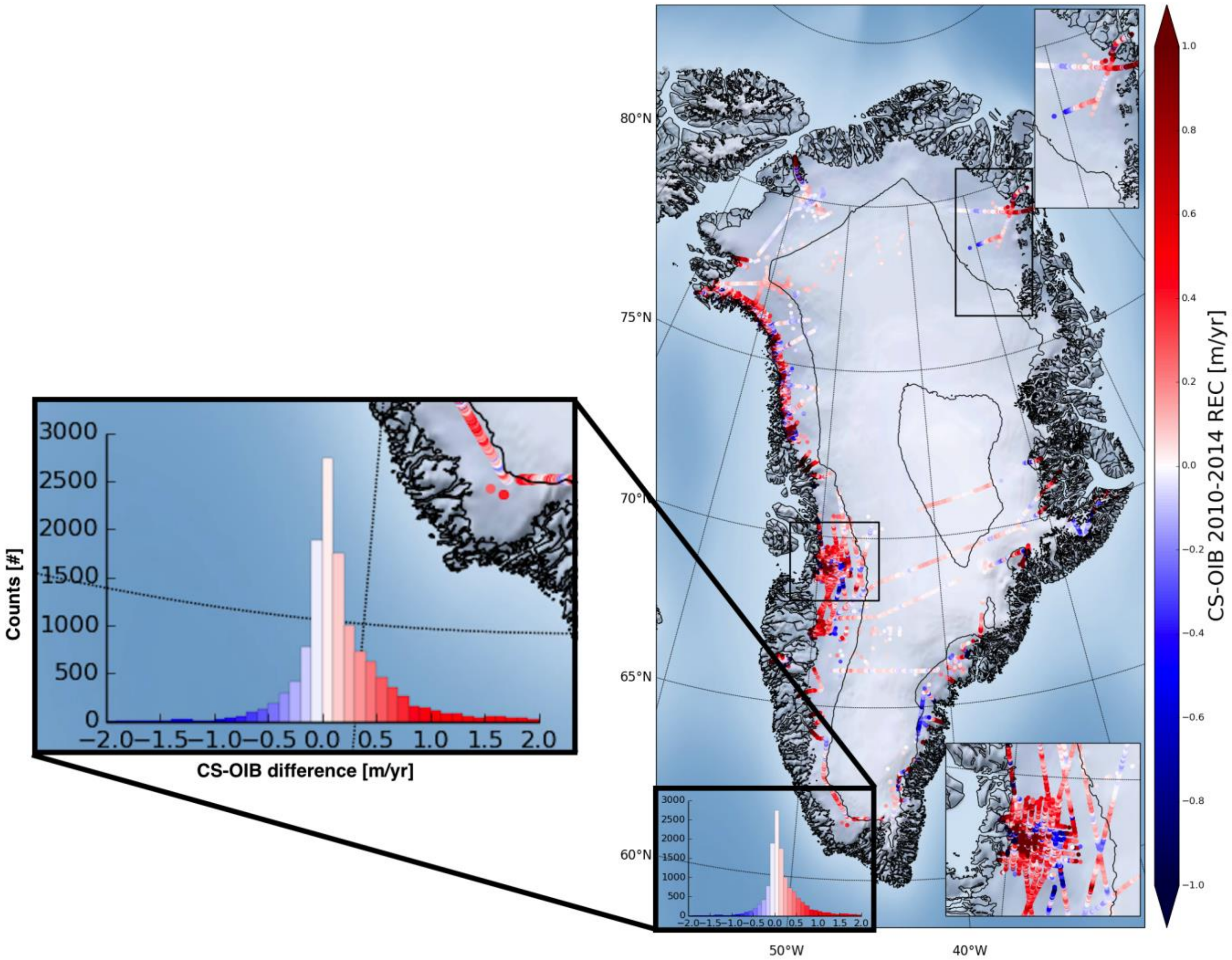

Figure 2-8: Elevation change difference between a Cryosat-2 elevation change product and the Operation IceBridge ATM elevation change. The histogram in the lower left corner shows the distribution of the differences between the Cryosat-2 and Operation IceBridge elevation changes at 0.1 m yr−1 bins. This figure is taken from Simonsen and Sørensen (2017).

2.6 AltiKa validation

The France/Indian satellite SARAL and its Ka-band altimeter AltiKa has been utilized to provide an experimental SEC product for the GrIS. This product has been validated against Operation IceBridge ATM data. The AltiKa SEC product differs from Crysat-2 by being a merged product of XO and LSM methods. Therefore, the validation has been performed on both the XO and LSM methods in addition to a validation of the final product. Figure 2.6-1 shows the data coverage of the merged product and the inter-comparison to Operation IceBridge. The Operation IceBridge data provides 38185 observations within 2.5 km of a ALtiKa SEC grid point. These points are used to evaluate the median difference and the standard derivation, which is found to be -0.007 m/yr and 0.278 m/yr, respectively.

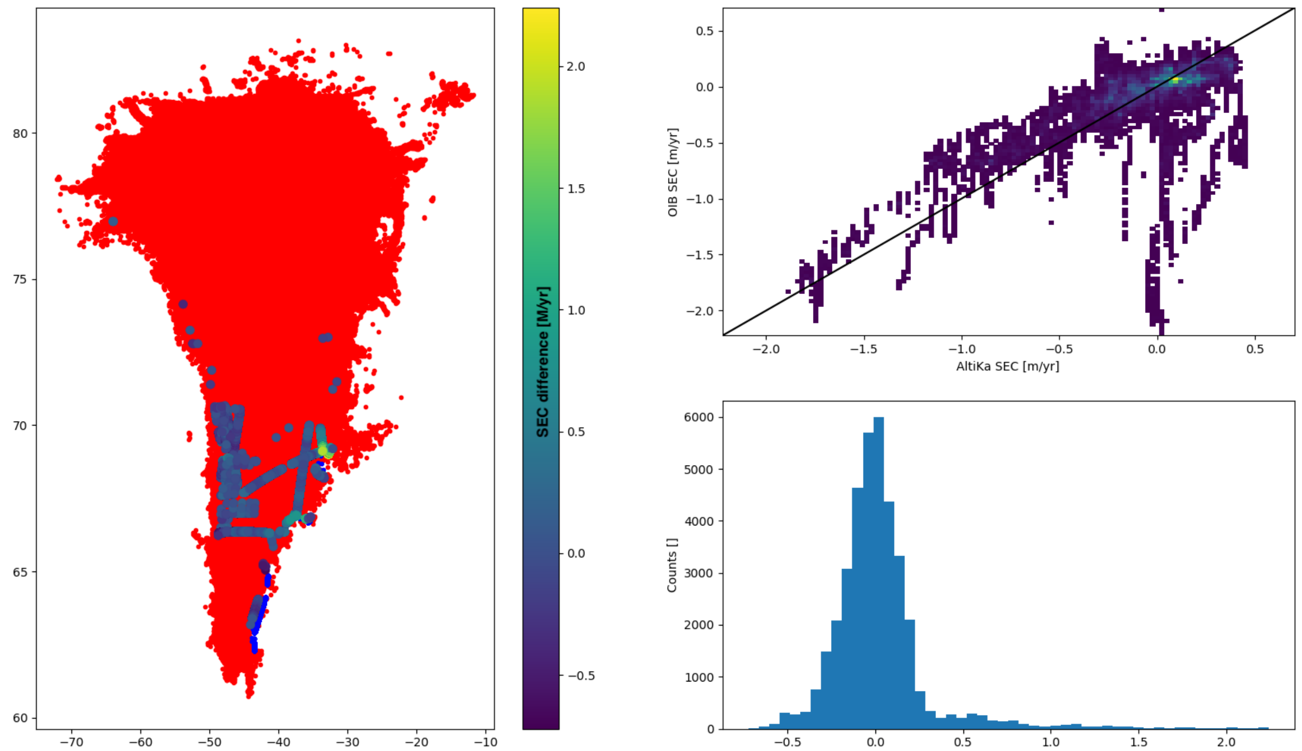

Figure 2-9: Inter-comparison of 2013-2016 operation IceBridge (OIB) SEC estimates and the merged AltiKa-SEC product derived for the same period in time. The upper right panel show the correlation between absolute OIB SEC and AltiKa SEC estimates.

2.7 Recommendations for product improvement

One key issue for improving the SEC accuracy is related to the retracking of radar data: A number of studies have shown that such observations need to be adjusted for all three waveform parameters, i.e. the backscatter coefficient, leading edge width, and trailing edge slope, to ensure the highest accuracy (e.g. Khvorostovsky, 2012; Legresy et al, 2005). Such an adjustment is performed for data retracked with the ICE-2, while the validated SEC trends are generated from the ICE-1, which only corrects for backscatter (Legresy et al, 2005; Wingham et al, 1986).

The ICE-1 retracker has been selected in spite of the applied ERS REAPER data having been retracked with both this as well as the ICE-2. However, as the latter results are currently subject to large biases and noise, care must be taken when assessing the data quality (Steven Baker, pers. comm., September 2014). Therefore, due to a wish of preventing errors from retracking the radar data differently, the ICE-1 was preferred. When improved ERS REAPER data are available in a future release, it is suggested to change the retracker.At present though, no reprocessing of ICE-2 retracked REAPER data is planned as far as the consortium are aware.

For CryoSat, the non-repeat orbit means that processing is more efficient by taking block averages, after suitable regression for waveform slope and tail parameters. A 5 km resolution grid size approach seems optimal, but great care must be taken at the mode switch border between LRM and SARIn. Details of the selected method have been outlined in the ATBD document.

A similar method might also improve older altimetry, and experiments have been ongoing. However, drifting orbits combined with repeat orbit periods make the method susceptible to aliasing when too small cells are used. Work will be ongoing to estimate adaptability of the method.

3 Ice Velocity (IV)

This chapter gives a summary of the activities carried out to assess the quality of both Radar and Optical Ice Velocity products.

3.1 Radar IV

We evaluate five radar products for accuracy by validating the radar-derived speeds against in-situ GPS measurements from various campaigns. The five radar products are listed in Figure 3-1**Error! Reference source not found.**. The temporal coverage is shown in and the spatial coverage is shown in through Figure 3-6. In this chapter the products will be referred to with the names listed in Table 3-1**Error! Reference source not found.**.

Table 3-1: Overview of radar products evaluated in this document.

Name	Time period(s)	Number of time period(s)
Greenland Margin (GRL_MARGIN_1995_1996) Sensor: ERS-2 Method: offset-tracking	03-Sep-1995 - 29-Mar-1996	1
Northern Basins (NBA_1991_1992) Sensor: ERS-1 Method: offset-tracking	29-Dec-1991 - 22-Mar-1992	1
PALSAR Greenland Margin (PALSAR_2006_2011) Sensor: ERS-2 Method: offset-tracking	20-Dec-2006 - 04-Jun-2007 07-Sep-2007 - 28-Dec-2007 15-Sep-2008 - 11-Mar-2009 28-Sep-2009 - 06-Mar-2010 13-Nov-2010 - 17-Mar-2011	5
Upernavik time series (UPE_1992_2010) Sensor: ERS-2 Method: offset-tracking	02-Jan-1992 - 23-Jan-1992 04-Sep-1992 - 09-Oct-1992 25-Jan-1993 - 01-Mar-1993 01-Mar-1993 - 05-Apr-1993 26-Mar-1995 - 30-Apr-1995 29-Mar-1995 - 03-May-1995 06-May-1995 - 10-Jun-1995 05-Feb-1996 - 15-Apr-1996 15-Apr-1996 - 20-May-1996 28-Nov-2002 - 02-Jan-2003 01-Dec-2002 - 05-Jan-2003 02-Jan-2003 - 06-Feb-2003 05-Jan-2003 - 09-Feb-2003 18-Jan-2003 - 22-Feb-2003 06-Feb-2003 - 13-Mar-2003 25-Feb-2003 - 01-Apr-2003 12-Jun-2003 - 17-Jul-2003 16-Nov-2003 - 21-Dec-2003 10-Jun-2004 - 15-Jul-2004 13-Jun-2004 - 18-Jul-2004 15-Jul-2004 - 19-Aug-2004 18-Jul-2004 - 22-Aug-2004 07-Sep-2004 - 12-Oct-2004 02-Dec-2004 - 06-Jan-2005 17-Mar-2005 - 21-Apr-2005 20-Mar-2005 - 24-Apr-2005 08-Sep-2005 - 13-Oct-2005 13-Oct-2005 - 17-Nov-2005 05-Dec-2005 - 09-Jan-2006 07-Jan-2006 - 11-Feb-2006 12-Jan-2006 - 16-Feb-2006 11-Feb-2006 - 18-Mar-2006 16-Feb-2006 - 23-Mar-2006 18-Mar-2006 - 22-Apr-2006 22-Apr-2006 - 27-May-2006 27-May-2006 - 01-Jul-2006 01-Jul-2006 - 05-Aug-2006 06-Jul-2006 - 10-Aug-2006 09-Jul-2006 - 13-Aug-2006	84

	10-Aug-2006 - 14-Sep-2006 13-Aug-2006 - 17-Sep-2006 20-Nov-2006 - 25-Dec-2006 23-Nov-2006 - 28-Dec-2006 23-Dec-2006 - 27-Jan-2007 25-Dec-2006 - 29-Jan-2007 01-Feb-2007 - 08-Mar-2007 05-Mar-2007 - 09-Apr-2007 08-Mar-2007 - 12-Apr-2007 09-Apr-2007 - 14-May-2007 18-Jun-2007 - 23-Jul-2007 21-Jun-2007 - 26-Jul-2007 24-Jun-2007 - 29-Jul-2007 21-Jul-2007 - 25-Aug-2007 26-Jul-2007 - 30-Aug-2007 29-Jul-2007 - 02-Sep-2007 11-Nov-2007 - 16-Dec-2007 08-Dec-2007 - 12-Jan-2008 16-Dec-2007 - 20-Jan-2008 14-Jan-2008 - 18-Feb-2008 20-Jan-2008 - 24-Feb-2008 01-May-2008 - 05-Jun-2008 05-Jun-2008 - 10-Jul-2008 08-Jun-2008 - 13-Jul-2008 10-Jul-2008 - 14-Aug-2008 17-Aug-2008 - 21-Sep-2008 13-Sep-2008 - 18-Oct-2008 15-Sep-2008 - 20-Oct-2008 21-Sep-2008 - 26-Oct-2008 18-Oct-2008 - 22-Nov-2008 23-Oct-2008 - 27-Nov-2008 27-Nov-2008 - 01-Jan-2009 29-Dec-2008 - 02-Feb-2009 01-Jan-2009 - 05-Feb-2009 13-Apr-2009 - 18-May-2009 25-Jun-2009 - 30-Jul-2009 30-Jul-2009 - 03-Sep-2009 29-Aug-2009 - 03-Oct-2009 08-Oct-2009 - 12-Nov-2009 20-Nov-2009 - 27-Jan-2010 03-May-2010 - 07-Jun-2010 10-Jun-2010 - 15-Jul-2010 13-Jun-2010 - 18-Jul-2010 12-Jul-2010 - 16-Aug-2010 18-Jul-2010 - 22-Aug-2010	
Jakobshavn time series (JKB_2002_2010) **Sensor: ENVISAT-ASAR** **Method: offset-tracking**	15-Dec-2002 - 19-Jan-2003 19-Jan-2003 - 07-Feb-2003 07-Feb-2003 - 14-Mar-2003 14-Mar-2003 - 12-Jun-2003 12-Jun-2003 - 17-Jul-2003 17-Jul-2003 - 19-Dec-2003 19-Dec-2003 - 16-Jul-2004 16-Jul-2004 - 01-Aug-2004 01-Aug-2004 - 25-Aug-2005 25-Aug-2005 - 12-Jan-2006 12-Jan-2006 - 16-Feb-2006 16-Feb-2006 - 23-Mar-2006 23-Mar-2006 - 27-Apr-2006 27-Apr-2006 - 06-Jul-2006 06-Jul-2006 - 10-Aug-2006 10-Aug-2006 - 28-Dec-2006 28-Dec-2006 - 01-Feb-2007 01-Feb-2007 - 08-Mar-2007 08-Mar-2007 - 12-Apr-2007 12-Apr-2007 - 17-May-2007 17-May-2007 - 21-Jun-2007 21-Jun-2007 - 26-Jul-2007 26-Jul-2007 - 30-Aug-2007 30-Aug-2007 - 04-Nov-2007 04-Nov-2007 - 09-Dec-2007 09-Dec-2007 - 17-Jan-2008 17-Jan-2008 - 21-Feb-2008 21-Feb-2008 - 14-Aug-2008 14-Aug-2008 - 23-Oct-2008	46

	23-Oct-2008 - 27-Nov-2008 27-Nov-2008 - 01-Jan-2009 01-Jan-2009 - 05-Feb-2009 05-Feb-2009 - 12-Mar-2009 12-Mar-2009 - 16-Apr-2009 16-Apr-2009 - 21-May-2009 21-May-2009 - 25-Jun-2009 25-Jun-2009 - 30-Jul-2009 30-Jul-2009 - 03-Sep-2009 03-Sep-2009 - 08-Oct-2009 08-Oct-2009 - 12-Nov-2009 12-Nov-2009 - 20-Jan-2010 20-Jan-2010 - 24-Feb-2010 24-Feb-2010 - 31-Mar-2010 31-Mar-2010 - 15-Jul-2010 15-Jul-2010 - 19-Aug-2010 19-Aug-2010 - 23-Sep-2010	

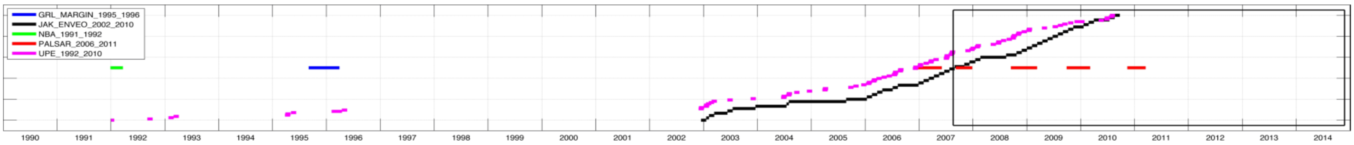

Figure 3-1: Temporal overview of radar products validated. Black rectangle indicates time period of available GPS data.

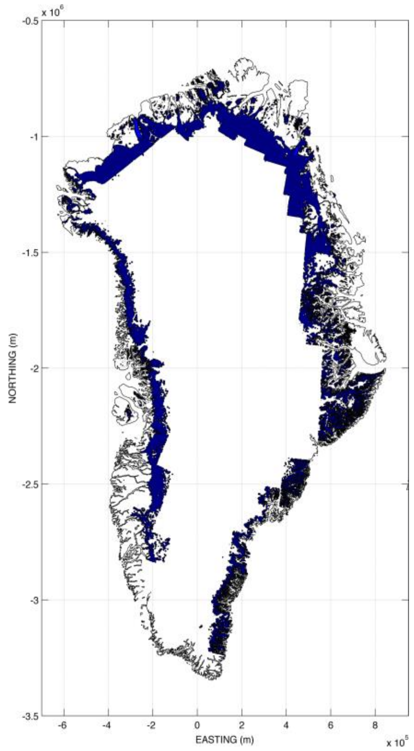

Figure 3-2: Spatial coverage of the GRL_MARGIN_1995_1996 product, one time window.

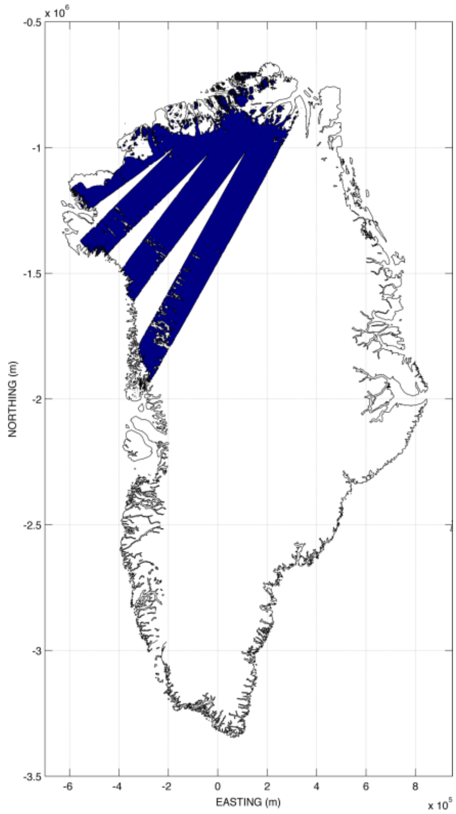

Figure 3-3: Spatial coverage of the NBA_1991_1992 product, one time window.

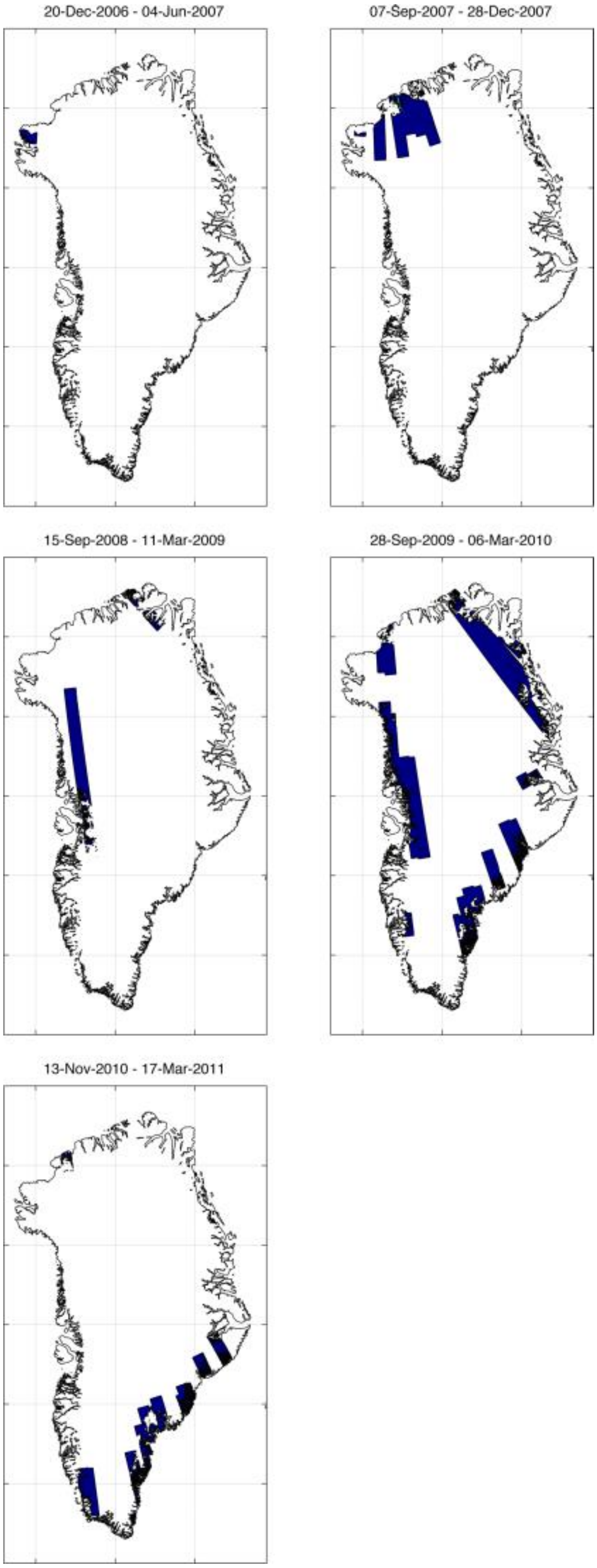

Figure 3-4: Spatial coverage of the PALSAR_2006_2011 product, five time windows.

The Upernavik timeseries contains 84 time windows with data content ranging from zero to 50370 points (20 Nov.-2009 to 27. Jan 2010), shown in Figure 3.5.

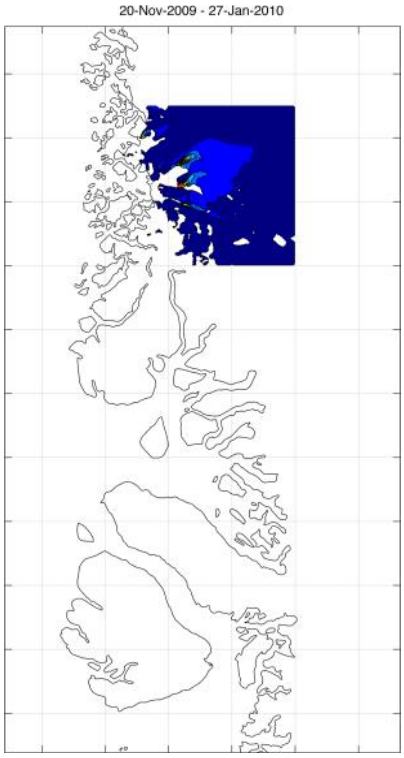

Figure 3-5: Coverage of the Upernavik, West Greenland, time series at the time window of maximum coverage, 20. Nov 2009 to 27. Jan 2010.

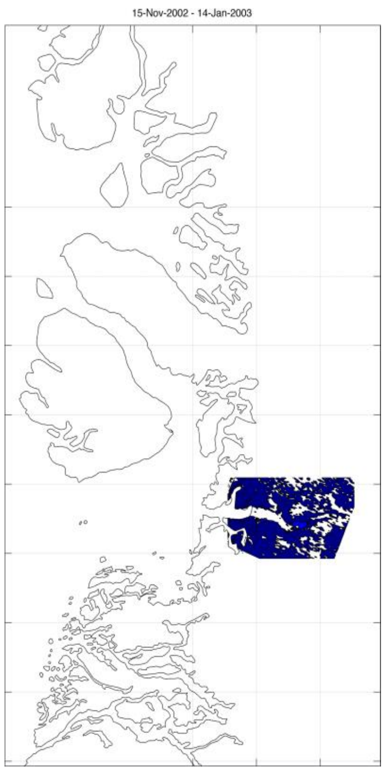

Figure 3-6: Coverage of the Jakobshavn, West Greenland, time series at the time window of maximum coverage, 15. Nov 2002 – 14. Jan 2003.

Table 3-2**Error! Reference source not found.** shows the content of the IV product .nc files, where **N** is the number of time periods available in product, and **m** and **n** are the dimensions of the m x n (in normal matrix notation) data arrays.

Table 3-2: List of variables in IV product .nc files

Name	Dimension	Comment
'crs'	-	Information on coordinate projection.
'y'	m x 1	y-axis coordinate values [m]
'x'	1 x n	x-axis coordinate values [m]
'time'	N x 1	Midpoint of acquisition dates [days since 1/1/1990 00:00:00]
'time_bnds'	2 x N	Acquisition dates [days since 1/1/1990 00:00:00]
'alt'	m x n	Elevation above WGS84 ellipsoide [m]
'land_ice_surface_east_velocity'	m x n	Ice flow velocity, Easting direction [m/d]
'land_ice_surface_north_velocity'	m x n x N	Ice flow velocity, Northern direction [m/d]
'land_ice_surface_east_velocity_std'	m x n x N	Std error on ice flow velocity, Eastern direction [m/d]
'land_ice_surface_north_velocity_std'	m x n x N	Std error on ice flow velocity, Northern direction [m/d]

3.1.1 Sources of independent validation data

Sources used in the validation are exclusively in-situ ice flow velocity observations carried out by use of Global Positioning System (GPS) receivers deployed in five different scientific campaigns.

Identifying GPS data sets that overlap with the radar product spatially and temporally is challenging. For this analysis, data from five sources have been retrieved.

Alternate sources are historical, manual surveying results. While these may be available in non-digitized form, they will typically be outside the temporal coverage of the radar products and carry too high uncertainties to be applicable.

3.1.1.1 In-situ observational data

The temporal coverage of the five available GPS data sets is shown in Figure 3-7 and listed in Table 3-3 **Error! Reference source not found.**

Table 3-3: List of GPS data sets used for validation

Source/ PI/Institution	Location	Total data vol. available (daily mean values)	Comment
Geological Survey of Denmark and Greenland (GEUS)	Greenland margin	8722	Data from GPS instruments mounted on the automatic weather stations (AWSs) in the PROMICE monitoring programme.
Ice2sea	Select outlet glaciers	7739	Data from GPS instruments deployed on select outlet glacier in the EU project “Ice2sea” with the main purpose of calibrating/validating glacier flow models. See Ahlstrøm et al., 2012.
IVEL	Select outlet glaciers	5090	Data from GEUS project “IVEL”, in which seasonal velocity changes of selected

			outlet glaciers from the Greenland Ice Sheet are monitored continuously with in situ, transmitting GPS to quantify uncertainties in ice flux calculations based on remote sensing.
University of Alaska	JakobshavnIsbræ	836	Data from GPS instruments deployed by Martin Truffer et al., University of Alaska, Fairbanks, to monitor velocity changes at JakobshavnIsbræ.
DTU Space	Upernavik Glacier Complex	228	Data from GPS instruments deployed by S. A. Khan, DTU Space, to monitor velocity changes at Upernavik Glacier.

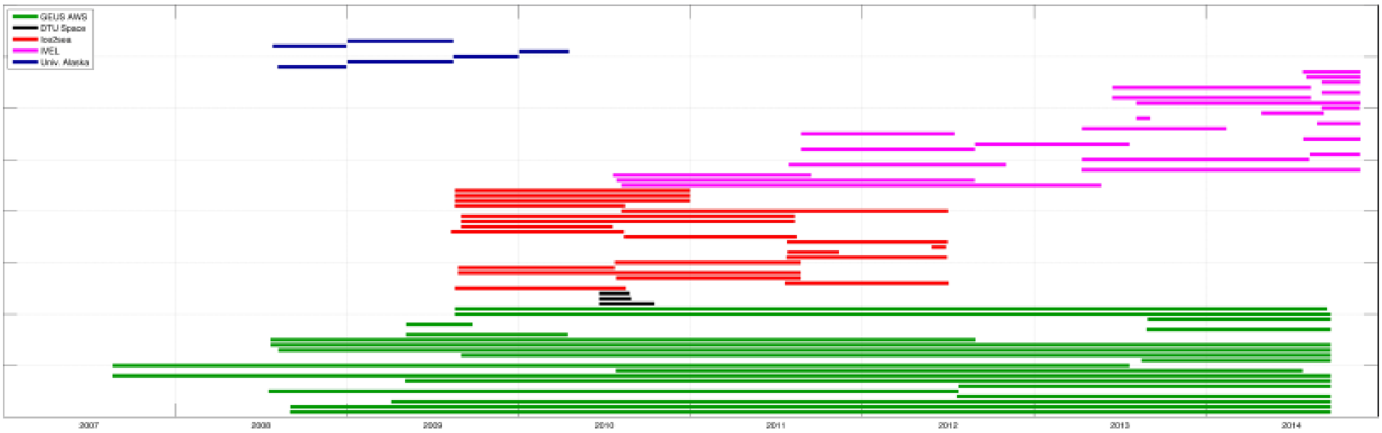

Figure 3-7: Temporal overview of GPS data sets available for the validation procedure. Each bar represents an instrument deployment.

3.1.1.2 Alternative products

Unpublished GPS data sets overlapping spatially and temporally may exist that are not known to the ESA CCI project participants.

Historical manual surveying results are judged to carry too high uncertainties, and typically predate the radar products.

3.1.2 Selection of independent validation data

3.1.2.1 Validation data selection criteria

The GPS data sets are scarce, therefore all available, published data which could be obtained within the time available for the validation process is included.

3.1.2.2 Validation data errors and biases

The GPS data used is not known to exhibit any bias.

3.1.2.3 Validation data uncertainty

We assume uncertainties of 15 m (horizontal) and 30 m (vertical) on a single GPS measurement regardless of the source. These may be conservative estimates. Detailed discussion of the propagation of uncertainties of positions and velocities is presented in section 3.1.3.1.3.

3.1.3 Validation procedure

The validation procedure is divided into two main steps: First the validation data is processed; second, the comparison against the CCI IV product is carried out. The following subsections address these steps.

3.1.3.1 Processing of GPS data

The following section details the steps taken in preparing the validation data sets.

3.1.3.1.1 Initial processing of raw position GPS data

The objective of the data processing steps taken is the development of daily mean values, uniformly formatted across all GPS data sources. Daily mean speeds in m/d allow for practical comparison of the in-situ value with the radar product, interpolated at the same locations.

All GPS data is delivered as raw, processed positions from the sources. Some initial processing of the GPS data is therefore carried out before the detailed processing and computation of daily mean position values (3.1.3.1.2) that will be used for velocity calculations. These initial processing steps include:

1. The raw position data typically include measurements outside the intended deployment area, such as test data from the home lab or recordings from airports/camps prior to deployment. These irrelevant data points are first removed.
2. Frequently, a data file contains data from multiple deployments (i.e., the instrument has been moved while recording). In these cases, the data is cut into separate, continuous sections. Therefore, there is not necessarily a direct correspondence between the number of data files delivered from the contributor and number of files used for the validation.

3.1.3.1.2 Outlier removal and the derivation of daily mean velocity values

The process of identifying and removing outliers carry similarities between the five GPS data sets, but the varying nature of the instrument types used and the purpose of the deployments necessitates different processing steps to be taken for different data sets.

3.1.3.1.2.1 GEUS AWS

1. Lat/Lon-format position data are converted to a polar stereographic coordinate system with standard parallel 70°N and central meridian 45°W.
2. The AWS operates in two modes: "Winter" and "Summer" mode. In summer mode, hourly positions are recorded. In winter mode, daily positions are recorded when available. In some cases, the AWS has recorded identical positions for several subsequent days in winter mode. These repeated data points are removed.
3. Winter data points are already perceived as daily means. However, these carry a higher uncertainty. Outliers in the winter values are identified by comparing the distance moved per day to the expected travelling distance computed using a LLS modelled prediction. Points that have moved further than three times the median modelled distance are removed.

4. To remove outliers in the summer data (hourly positions), an 8-hr rolling window is applied. In each window, points falling outside 1 standard deviation of the mean position in the window are removed.
5. Daily mean values are computed for days that have 12 or more hourly values left after outliers are removed as described in (4). Days that do not meet this criterion are discarded.
6. The list of daily mean values is now filtered by the distance moved per day, as in (3). However, in this case the residual between the modelled and observed distance moved per day is considered and points with residuals falling outside the mean residual +/- the 25-75% interquartile range are removed.

An example from the west Greenland station KAN_L (lower Kangerlussuaq) is shown in Figure 3-8.

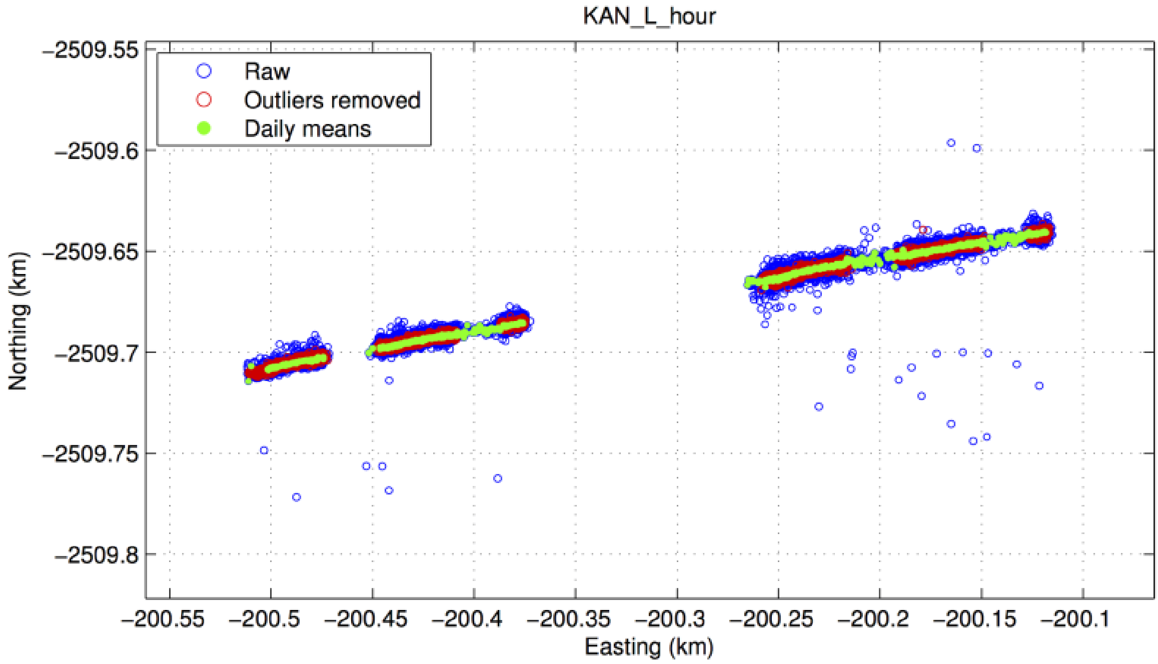

Figure 3-8: Outlier removal and development of daily mean velocities for the GEUS AWS "KAN_L". Green dots indicate the filtered data on which the speed calculation that will serve as validation of the radar products will be carried out.

3.1.3.1.2.2 Ice2sea

GPS data sets originating from the ice2sea project are first processed using the algorithm described in Den Ouden et al. (2010). The resulting data set contains hourly and 6-hourly mean position values that are then treated as follows:

1. Lat/Lon-format position data are converted to a polar stereographic coordinate system with standard parallel 70°N and central meridian 45°W.
2. Daily mean values are computed for days that have more than 12 (for hourly data) or 2 (for 6-hourly data) available. Days that do not meet this criterion are discarded.

3.1.3.1.2.3 IVEL

GPS receivers from the IVEL project transmit positions 2-7 times per day via Iridium link to GEUS depending on season and satellite coverage. The transmitted positions are processed as follows:

1. Lat/Lon-format position data are converted to a polar stereographic coordinate system with standard parallel 70°N and central meridian 45°W.
2. Obvious outliers are removed by comparing computed distance moved per day to distances expected based on the mean flow speed of the receiver in the last up to 30 days (i.e., highest

recorded speeds). Points travelling with a speed corresponding to more than three times this mean speed are discarded.

3. Less obvious outliers are removed by comparing distance travelled per day to a modelled expected travel distance per day derived from a 2.-order polynomial fitted to the data points remaining after (3). An envelope of accepted points is defined by the modelled expected travel distance +/- 50%. Points outside this envelope are discarded.

An example from the East Greenland IVEL station “HELHEIM” is shown in Figure 3-9.

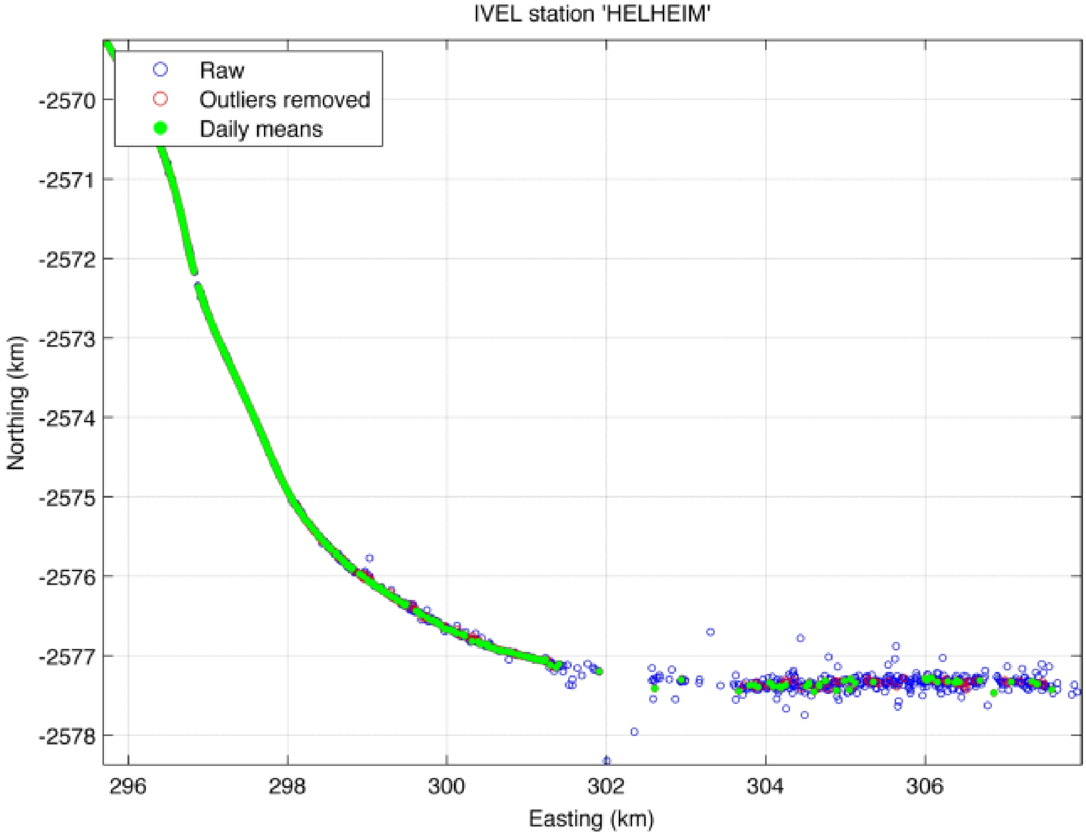

Figure 3-9: Outlier removal and development of daily mean velocities for the IVEL GPS station “HELHEIM”. Green dots indicate the filtered position data on which the speed calculation that will serve as validation of the radar products will be carried out.

3.1.3.1.2.4 DTU Space

GPS data from DTU Space deployment at the Upernavik glacier complex are delivered as daily mean positions from the source. These positions are processed as follows:

1. Lat/Lon-format position data are converted to a polar stereographic coordinate system with standard parallel 70°N and central meridian 45°W.

3.1.3.1.2.5 Univ. Alaska

GPS data from University of Alaska were recorded in “bursts” of one hour per day during which observations were made twice per minute.

1. Lat/Lon-format position data are converted to a polar stereographic coordinate system with standard parallel 70°N and central meridian 45°W.
2. All data points from a 1-hour burst are considered group wise. Points departing more than 2 standard deviations from the mean position in the group are considered outliers and are discarded.

3. The list of daily mean values is filtered by the distance moved per day by considering the residual between the observed distance moved per day and a LLS modelled expected distance moved per day. Points with residuals falling outside the mean residual +/- 2 times the 25-75% interquartile range are removed.

3.1.3.1.3 Uncertainties on GPS data

Uncertainties on all GPS positions are propagated to the daily means as:

$$\Delta x_{mean} = \sqrt{\frac{\sum_{n=1}^{N} \Delta x_n}{N^2}}$$

Where N is the number of measurements in the mean and Δx_n is the uncertainty on measurement number n, which is set to the values in section 3.1.2.3 for the three position components.

3.1.3.2 Interpolation of radar-derived products

The interpolation algorithm that produces the validation results is shown in the flowchart in Figure 3-10.

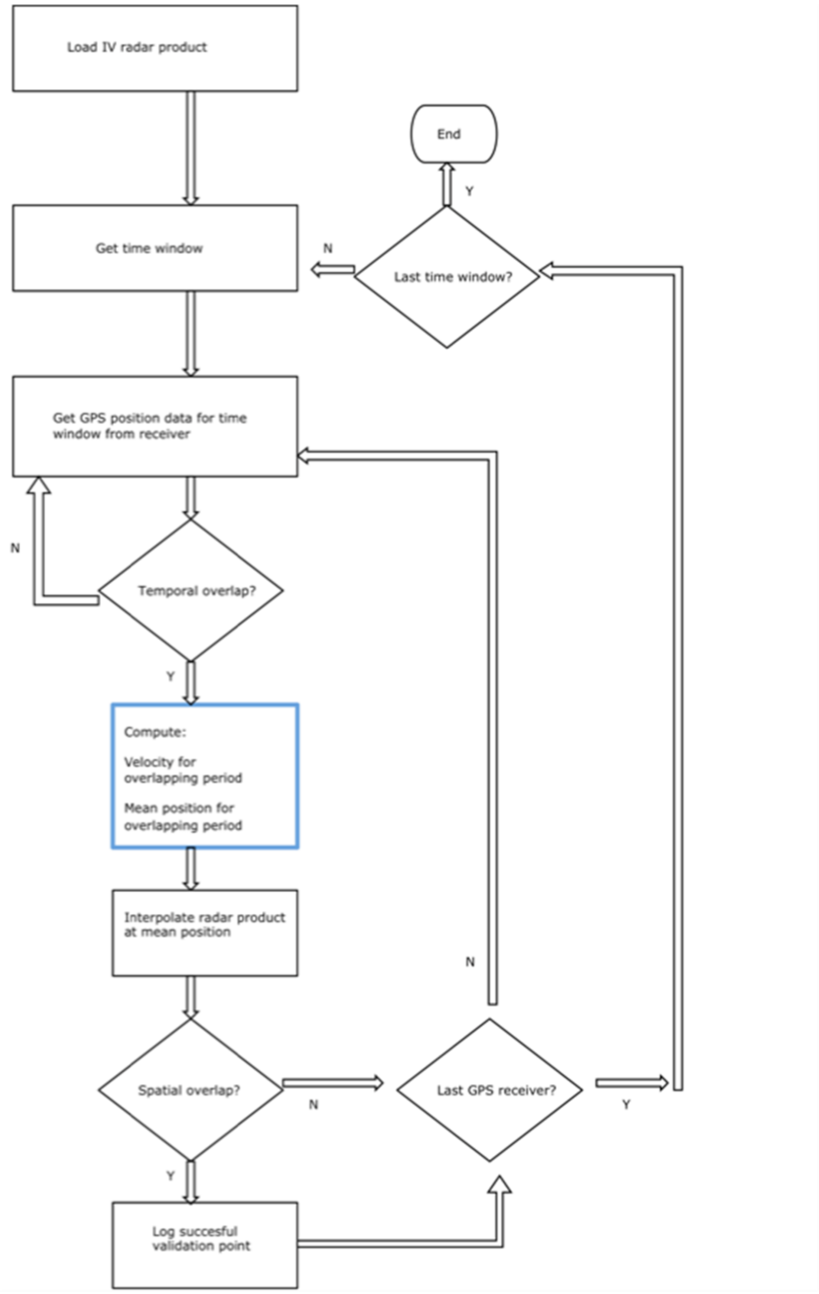

Figure 3-10: Flow chart showing the main steps in the validation algorithm.

3.1.3.3 GPS speed estimate

The flow speed derived in the blue process box in Figure 3-10 is computed as a weighted linear least squares fit of the Easting and Northing daily mean position components with the reciprocal position uncertainty as weights. An example is shown in Figure 3-11. Only the data points within the time window are considered in the fit and the estimated mean position.

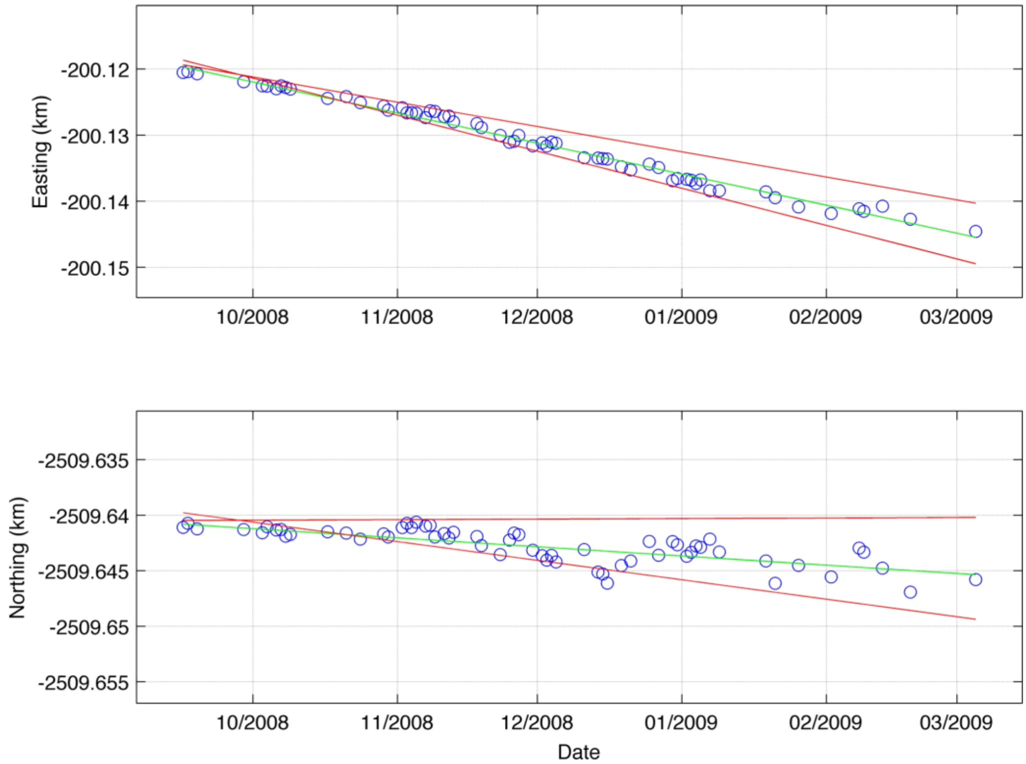

Figure 3-11: Example of weighted LLS fit to Northing and Easting components of GEUS AWS "KAN_L" located in West Greenland near Kangerlussuaq. Red lines indicate upper and lower bound uncertainties on the slope (i.e. the flow velocity in each component) derived from the pseudo-Monte Carlo method.

3.1.3.3.1 Uncertainty on the velocity estimate

Uncertainty on the velocity derived from the positions is estimated in a pseudo-Monte Carlo scheme. A random number of the relevant points (i.e., falling within an IV radar product time window) are perturbed by a random amount within the uncertainty bounds given in 3.1.2.3. The weighted LLS fit is then carried out thus estimating a perturbed velocity of the two components. This is repeated 1000 times, yielding 1000 randomly perturbed slope/intercept pairs. The velocity uncertainty bounds are then taken as the 5th and 95th percentile of the range of slope/intersects represented. In order to have symmetrical uncertainty bounds, the maximum value of the two is applied as both the upper and lower bound.

3.1.4 Validation procedure outcome

With the five available GPS validation data sets, two of the four CCI IV data sets can be validated. The Greenland Margin (GRL_MARGIN_1995_1996) and Northern Basins (NBA_1991_1992) both predate the GPS data series.

Of the two radar products that can be validated, there is spatial and temporal overlap in two of the five PALSAR acquisition windows (Figure 3-12) and in three of the 84 time periods in the Upernavik time series (Figure 3-13:).

The amounts of daily values used in the validation are listed in Table 3.4.

Table 3-4: List of number and type of daily GPS velocity values used in the validation of the four radar products.

	Total GPS data vol. used (daily values)			
Source/ PI/Institution	Greenland Margin (GRL_MARGIN_1995_1996)	Northern Basins (NBA_1991_1992)	PALSAR Greenland Margin (PALSAR_2006_2011)	Upernavik time series (UPE_1992_2010)
Geological Survey of Denmark and Greenland (GEUS)	0	0	187	25
Ice2sea	0	0	1302	174
IVEL	0	0	0	0
University of Alaska	0	0	147	0
DTU Space	0	0	0	0

3.1.4.1 PALSAR Greenland Margin (PALSAR_2006_2011)

Temporal and spatial overlap between the radar product (PALSAR_2006_2011) and the five available GPS sets exists in the last two of the five acquisition periods, i.e., 28. Sep–6. Mar 2010 and 13 Nov.-17. Mar. 2011 where three of the five GPS data sets contribute (GEUS AWS, ice2sea, and Univ. of Alaska). A scatterplot of the interpolated radar velocities at the mean GPS positions vs. the GPS speeds at those positions is shown in Figure 3-12: .

The fit statistics indicate a high correlation (R^2 = 0.98) between the radar and the GPS velocities. The offset between the two is small, ~7 cm/d, indicating no large systematic error. The slope of the fit line is slightly positive, suggesting a small proportional underestimation of the velocities in the radar product. However, five of the 13 points in the plot are within uncertainty consistent with the x=y line representing a perfect fit.

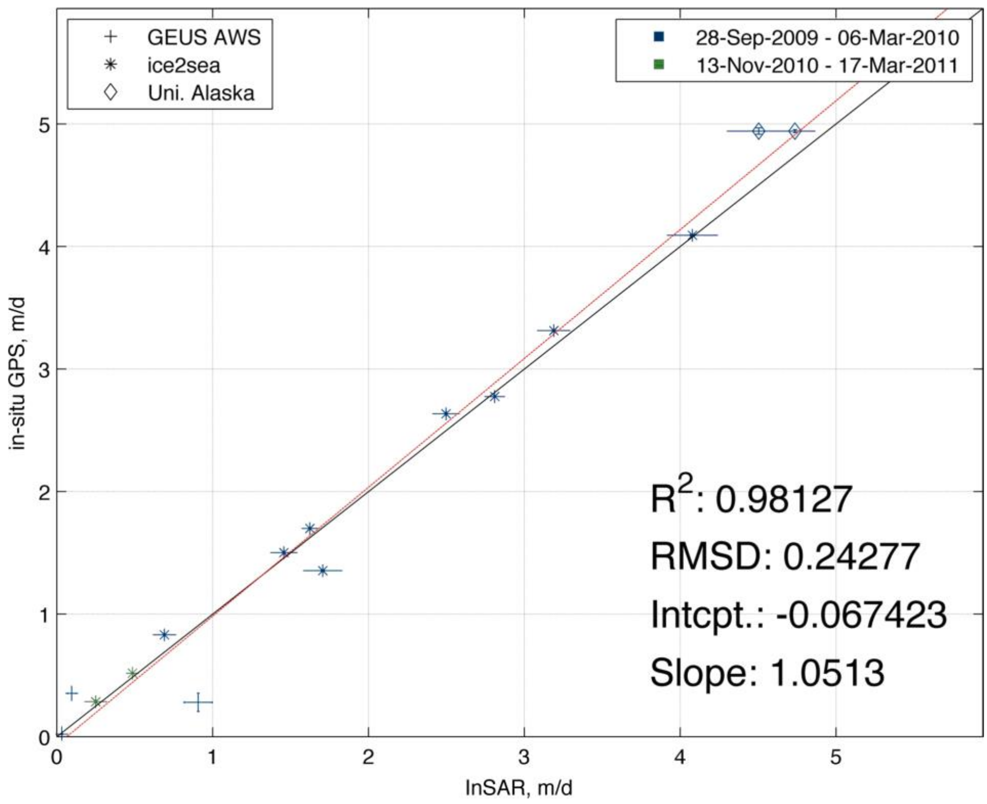

Figure 3-12: Results of the validation of the PALSAR 2006-2011 data set. Black line indicates y=x, i.e., perfect correspondence between inSAR and GPS velocities. Red line shows the fit of the data with statistics listed in the lower right corner. Uncertainties on the ice2sea and the University of Alaska are not visible in the plot because they are too small.

3.1.4.2 Upernavik time series (UPE_1992_2010)

Temporal and spatial overlap between the radar product (UPE_1992_2010) and the five available GPS sets exists in three of the 84 acquisition periods, i.e., 8. Oct. 2009–12.Nov. 2009, 20. Nov 2009-27. Jan 2010, and 18. Jul 2010-22. Aug. 2010. Two of the five GPS data sets contribute (GEUS AWS and ice2sea). A scatterplot of the interpolated radar velocities at the mean GPS positions vs. the GPS speeds at those positions is shown in Figure 3-13.

The fit statistics indicate a good correlation (R^2 = 0.95) between the radar and the GPS velocities. The offset between the two is ~34 cm/d, indicating some systematic error towards lower radar velocities. The slope of the fit line is smaller (still positive), suggesting a proportional overestimation of the velocities in the radar product. Two of the seven points in the plot are within radar uncertainty consistent with the x=y line representing a perfect fit.

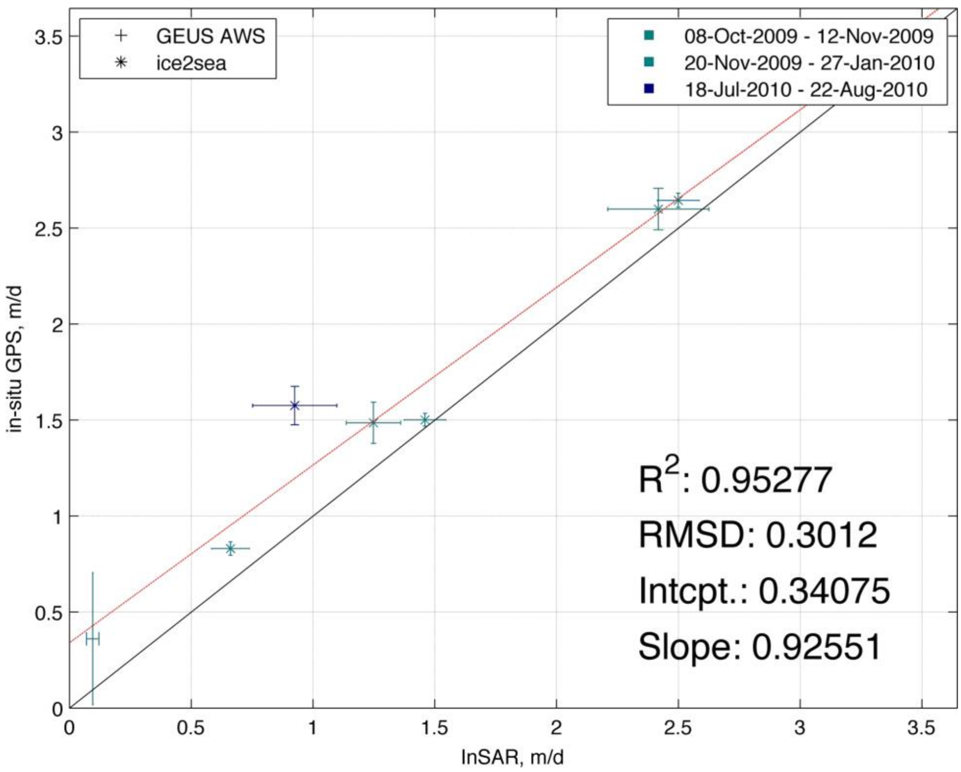

Figure 3-13: Results of the validation of the Upernavik 1992-2010 data set. Black line indicates y=x, i.e., perfect correspondence between inSAR and GPS velocities. Red line shows the fit of the data with statistics listed in the lower right corner.

3.1.4.3 Update: 9 major outlet glaciers: Upernavik time series 1992-2010

The data set 'Time series of 9 major outlet glaciers' was released March 2017 based on ERS and Envisat data. This is a new dataset and was produced using the interferometric post processing chain (IPP).

The GPS dataset described in Ahlstrøm et al, 2013 (equivalent to the Ice2Sea dataset) is applied in the comparison. Only the GPS time series from Upernavik in the dataset has both spatial and temporal overlap with the "Nine major outlet glaciers" –time series. The earlier version of the Upernavik time series was produced using SUSIE rather than IPP. This section is thus also an update of Section 3.4.2.

There are four radar IV maps from Upernavik which overlap temporally with the gps data: [3 Sep 2009 – 8 Oct 2009], [8 Oct 2009 – 12 Nov 2009], [13 Nov 2009 – 18 Nov 2009] and [18 Dec 2009 -22 Jan 2010] and of these four maps only maps [3 Sep 2009 – 8 Oct 2009] and [8 Oct 2009 – 12 Nov 2009] have spatial overlap with GPS2 and GPS3 –while there is no spatial overlap with GPS4, which is positioned furthest from the glacier front (See Figure 3-14).

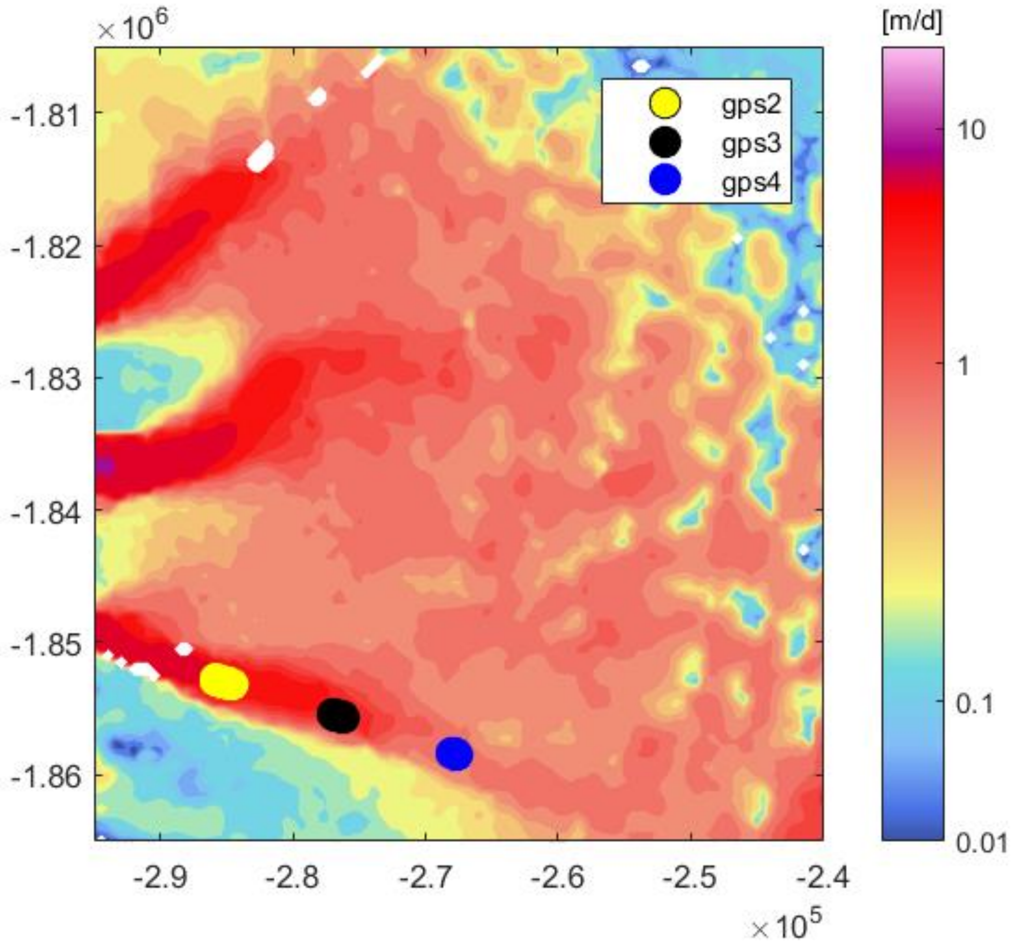

Figure 3-14: Map showing the positions of the three GPS timeseries applied in the comparison. The background ice velocity map is a composite of winter data from 1992.

A scatter plot of the interpolated radar velocities at the mean GPS positions vs the GPS speeds at those positions is shown in Figure 3.15. The fit statistics are also displayed on the figure -please note that there are only four points in the calculation. The relative difference between the GPS and radar data is between 7-9% and two out of four points are within the radar uncertainty consistent with the y=x line indicating perfect correspondence. . All four points are above the x=y line indicating that the radar based velocities are slower than the velocities derived from the GPS measurements. This was also seen in the old dataset derived using a different processor. There are no data points in the region of low velocities, which might explain why the fit is better for the new version of the dataset compared to the old.

Statistics based on four points is not very reliable. However, that aside the tendency of the radar product to be slower than the GPS derived velocities could result from the lower spatial resolution of the offset-tracking procedure due the relatively large size of the search window. At Upernavik, the size of the search window in the azimuth is large compared to the width of the glacier. If the search window thus includes slower moving ice due to a local gradient or unintentionally includes bedrock points, then a slower velocity is measured in the radar product.

A minor part of the difference could also arise from the comparison procedure itself. The GPS-derived velocities are calculated using a linear fit of the x and y positions vs time, whereas the radar derived velocity is the displacement between the two radar images. As the GPS moves downstream over the 35 day period the velocity generally increases and the best fit to position vs time may not be a linear fit. The differences arising from the comparison procedure are most likely small –of the order of centimetres per day as estimated by looking at the change in velocity over the movement of GPS2 during the 35 days. In order to explore the tendency of slower radar velocities compared to the GPS velocities, a smaller search window could be tested perhaps using data with a higher resolution e.g. from CosmoSkyMed and it could be looked into how the method for calculating the GPS derived velocities influences the comparison.

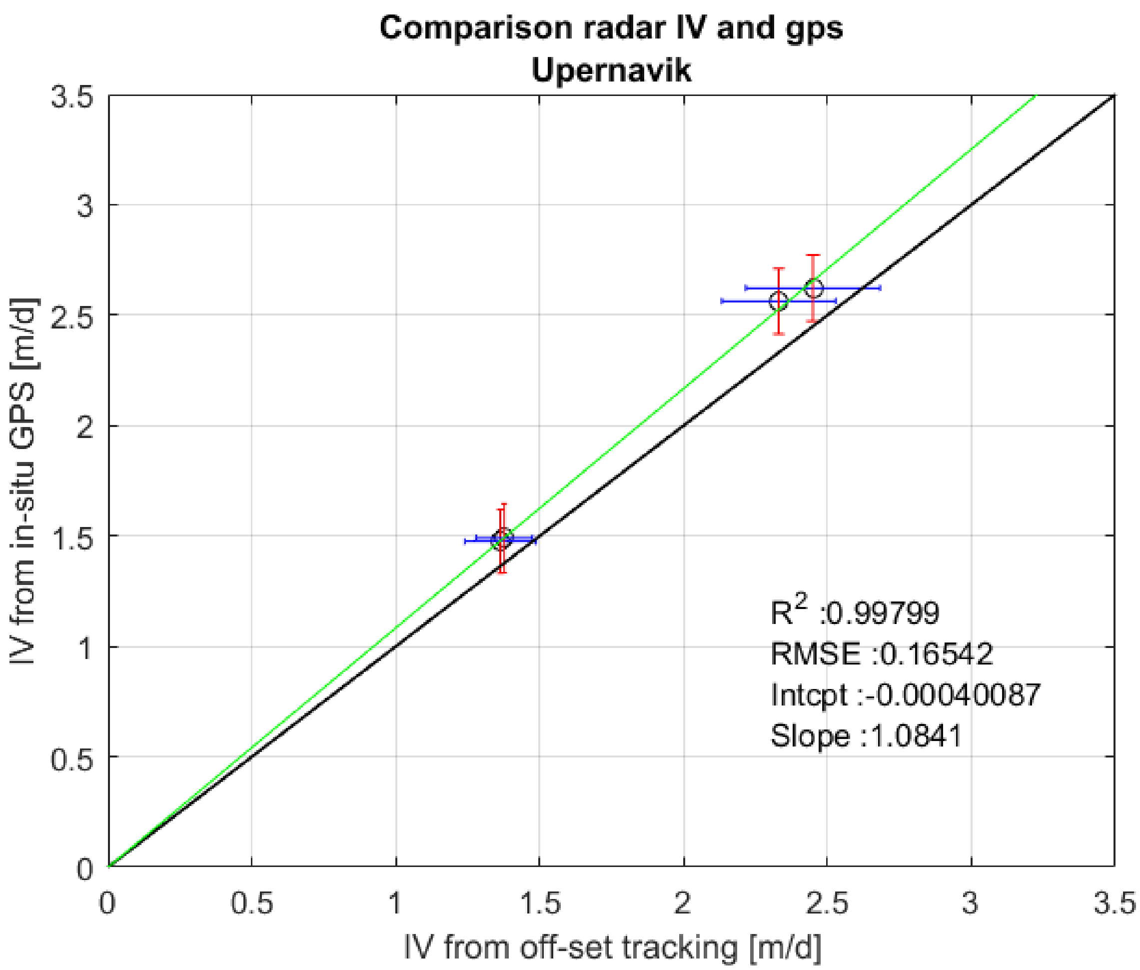

Figure 3-15: Results of the validation of the Upernavik 1992-2010 data set. Black line indicates y=x, i.e., perfect correspondence between inSAR and GPS velocities. Green line shows the fit of the data with statistics listed in the lower right corner.

3.1.4.4 Jakobshavn time series (JKB_2002_2010)

Temporal and spatial overlap between the radar product (JKB_2002_2010) and the five available GPS sets exists in one of the 46 acquisition periods, i.e., 30. Jul 2009 – 3. Sept. 2009. One of the five GPS data sets contribute (University of Alaska). A scatterplot of the interpolated radar velocities at the mean GPS positions vs. the GPS speeds at those positions is shown in Figure 3-16. Uncertainty on the radar-derived velocity is assumed to be 10%. The radar-derived velocity in the point is consistent within uncertainty with the GPS velocity.

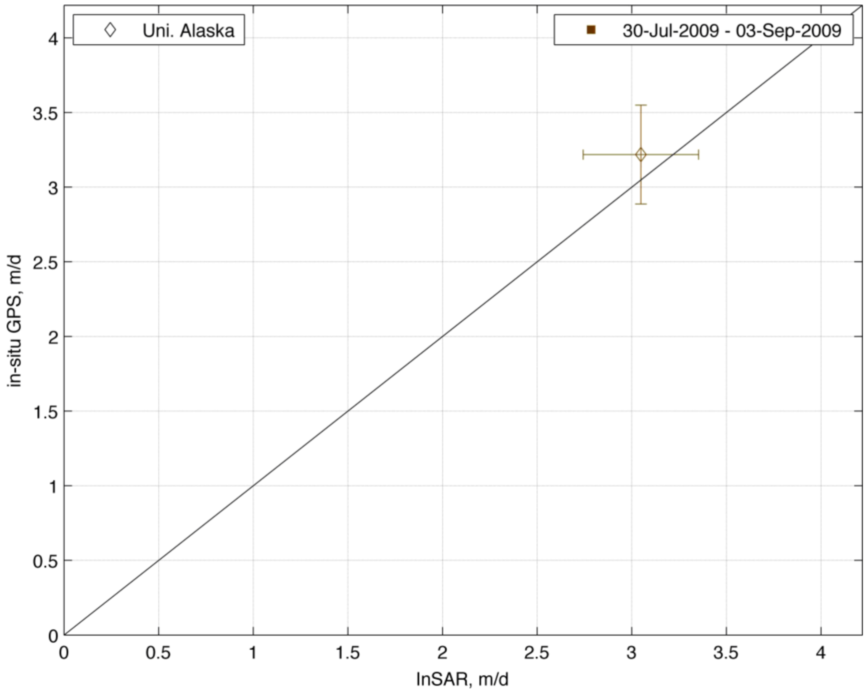

Figure 3-16: Result of the validation of the Jakobshavn 2002-2010 data set. Black line indicates y=x, i.e., perfect correspondence between inSAR and GPS velocities.

3.1.5 Recommendations for product improvement

The current IV products generally perform well, where in-situ data is available for comparison.

Velocities from the Upernavik 1992-2010 time series appear lower than the corresponding in-situ observations. However, due to the systematic nature of the offset, this can possibly be adjusted for in the processing algorithm in future product releases. Further analysis on this is recommended.

The uncertainty field associated with the Greenland ice margin 1995-1996 radar product (see **Error! Reference source not found.**Figure 3-1**Error! Reference source not found.**) includes points with very high uncertainties compared to the absolute velocities. Signal-to-noise ratio (SNR) values below one are found in the data set, especially pronounced in slow-moving areas in South/South East Greenland. It is recommended that these points be filtered from the data set.

3.1.6 Acknowledgements of data contributors for IV validation

ESA CCI wishes to acknowledge the following persons and institutions for providing in-situ GPS data for use in the IV validation work: S. A. Khan, DTU Space, Copenhagen and Martin Truffer, University of Alaska Fairbanks, USA.

3.2 Optical IV (OptIV)

This Section gives a summary of the activities carried out to assess the quality of Opt-IV products.

3.2.1 Sources of independent validation data

The 50m-resolution OptIV products have been validated against the following data sets:

1. SAR IV ECV, generated by ENVEO's team from Sentinel-1 data.
2. SAR IV PROMICE, generated by GEUS' team from Sentinel-1 data.
3. OptIV ENVEO, generated by ENVEO's team from Sentinel-2 data.

SAR PROMICE IV maps were produced from ESA Sentinel-1 SAR data and were provided by the Geological Survey of Denmark and Greenland (GEUS). The resolution of the data sets is 500m. It has been selected because it is a mature product, having being extensively validated, and because of its wide time period coverage. Indeed, the main criterion for the selection of the validation data sets was the overlapping of the time periods of optical and SAR IV products. In order to be compared with the other products, SAR PROMICE IV was interpolated to a resolution of 100m.

SAR IV ECV products were generated using ESA Sentinel-1 SAR data and were provided by ENVEO. The data sets contain only points along the flow line of the glacier and have a resolution of 250m.

The OptIV ENVEO product was generated using ESA Sentinel-2 data and was provided by ENVEO. The resolution of the product is 100m.

Both SAR IV ECV, SAR IV PROMICE and OptIV ENVEO products are provided on a polar stereographic grid (EPSG3413: Latitude of true scale 70N, Reference Longitude 45E). The horizontal velocity is provided in true meters per day, towards easting (x) and northing (y) direction of the grid.

The datasets used for validation are listed in Table 3-5**Error! Reference source not found.**.

Table 3-5: List of data sets used for validation

Name	Dataset	Time period(s)	Number of time period(s)
Academy Glacier **Sensor: Sentinel-2** **Method: offset-tracking**	OptIV ENVEO	20-30/07/2017	1
Hagen Glacier **Sensor: Sentinel-2** **Method: offset-tracking**	OptIV ENVEO	20-30/07/2017	1
Hagen Glacier **Sensor: Sentinel-1** **Method: offset-tracking**	SAR IV PROMICE	16/07/2017-08/08/2017, 10/07/2017-02/08/2017	2

3.2.1.1 In-situ observational data

A validation versus in-situ observational data was not possible. This was caused primarily by the scarce availability of in-situ GPS data.

3.2.2 Validation procedure outcome based on analysis of velocity vectors

A first validation test was performed by visualising the velocity vectors of all the 8 glaciers for which OptIV products were generated. The idea of velocity vector comes from classical physics, by representing the position and motion using vectors. Figure 3-17 - Figure 3-24 have been generated using the easting (x) and northing (y) components of the velocity, and averaging the velocity over 5x5 pixels “cells”. This last step was done for minimising the contribution of random noise. The vector arrows indicate the direction of the flow. A ‘by-eye’ evaluation of each figure shows that the flow directions of the optical products are consistent with expectations.

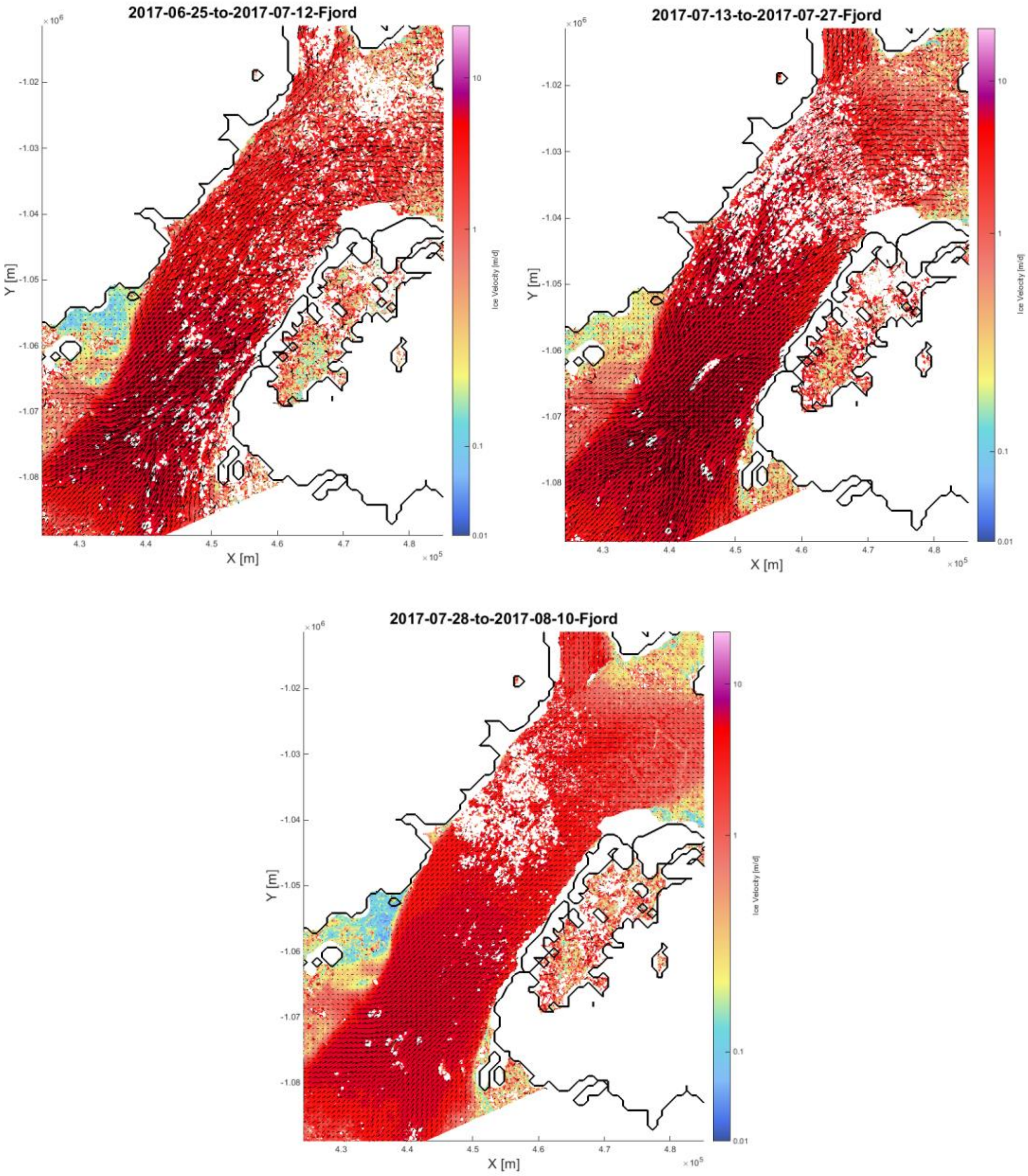

Figure 3-17: 79Fjord Glacier – Opt IV velocity vector plots for the following time periods: 25th June – 12th July 2017 (top left), 13th – 27th July 2017 (top right) and 28th July – 10th August 2017 (bottom).

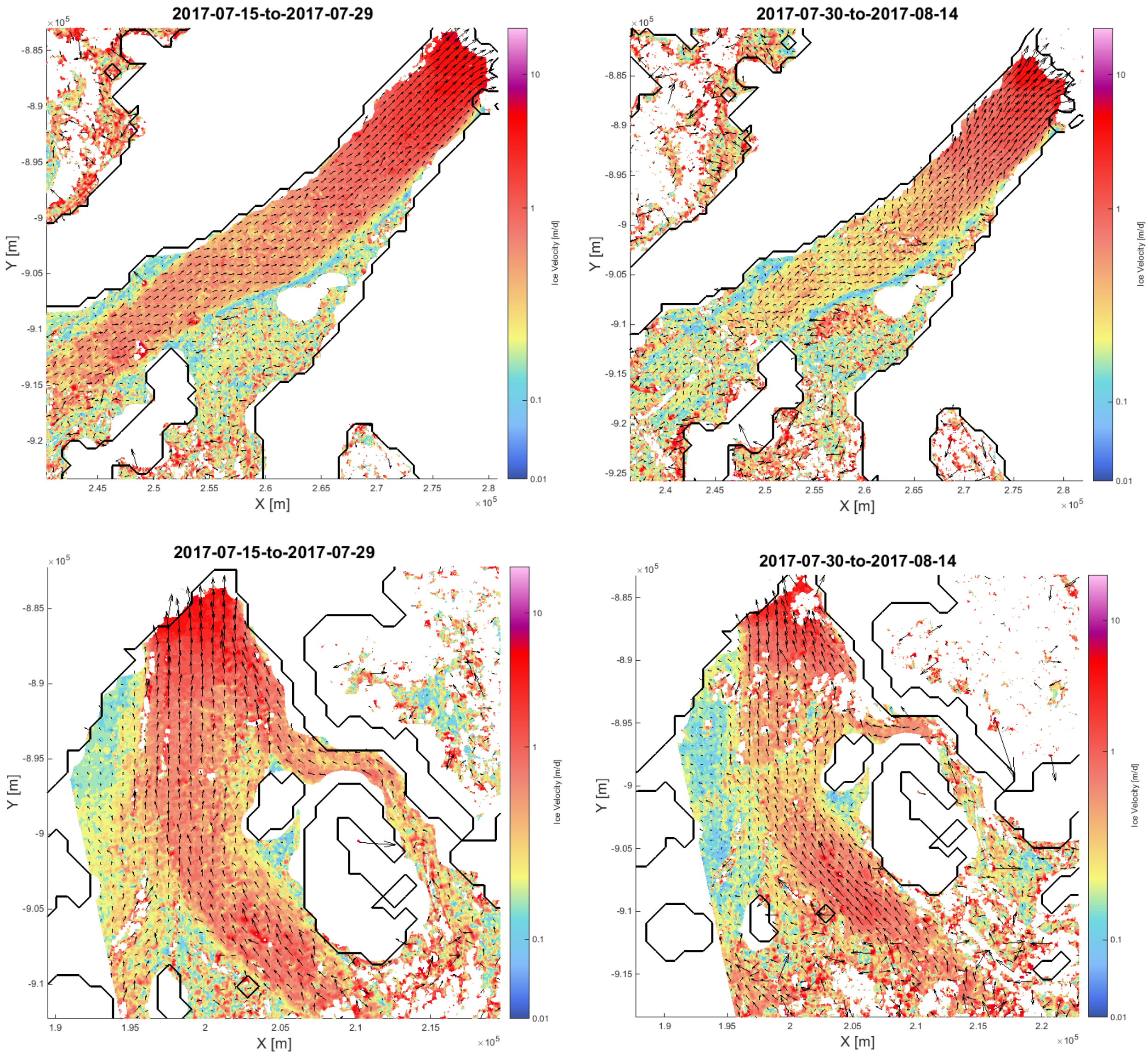

Figure 3-18: Hagen Glacier – Opt IV velocity vector plots for the following time periods: 15th – 29th July 2017 (Eastern area: top left, Northern area: bottom left), and 30th July – 14th August 2017 (Eastern area: top right, Northern area: bottom right).

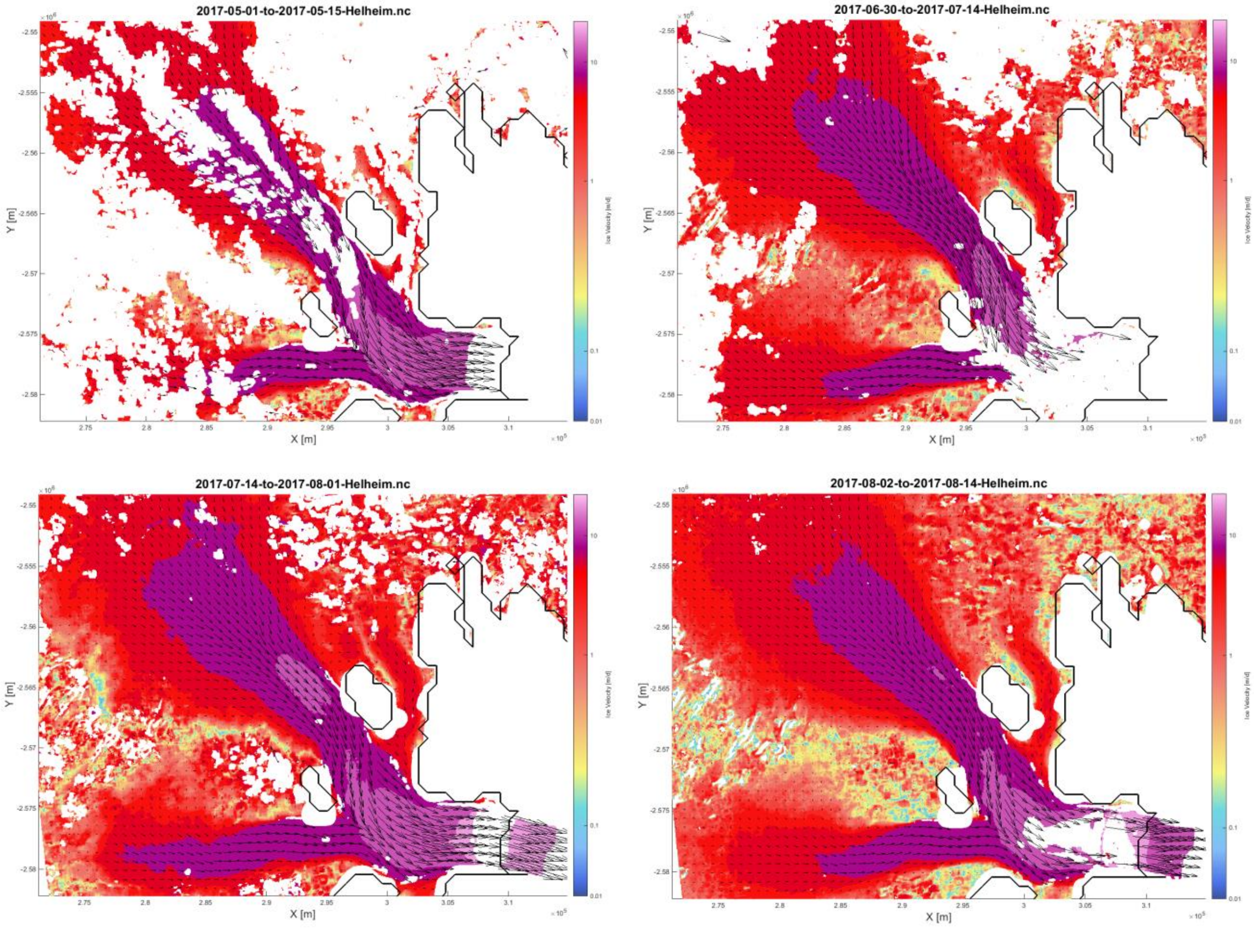

Figure 3-19: Helheim Glacier – Opt IV velocity vector plots for the following time periods: 1st – 15th May 2017 (top left), 30th May – 14th July 2017 (top right), 14th – 01st August 2017 (bottom left) and 2nd - 14th August 2017 (bottom right).

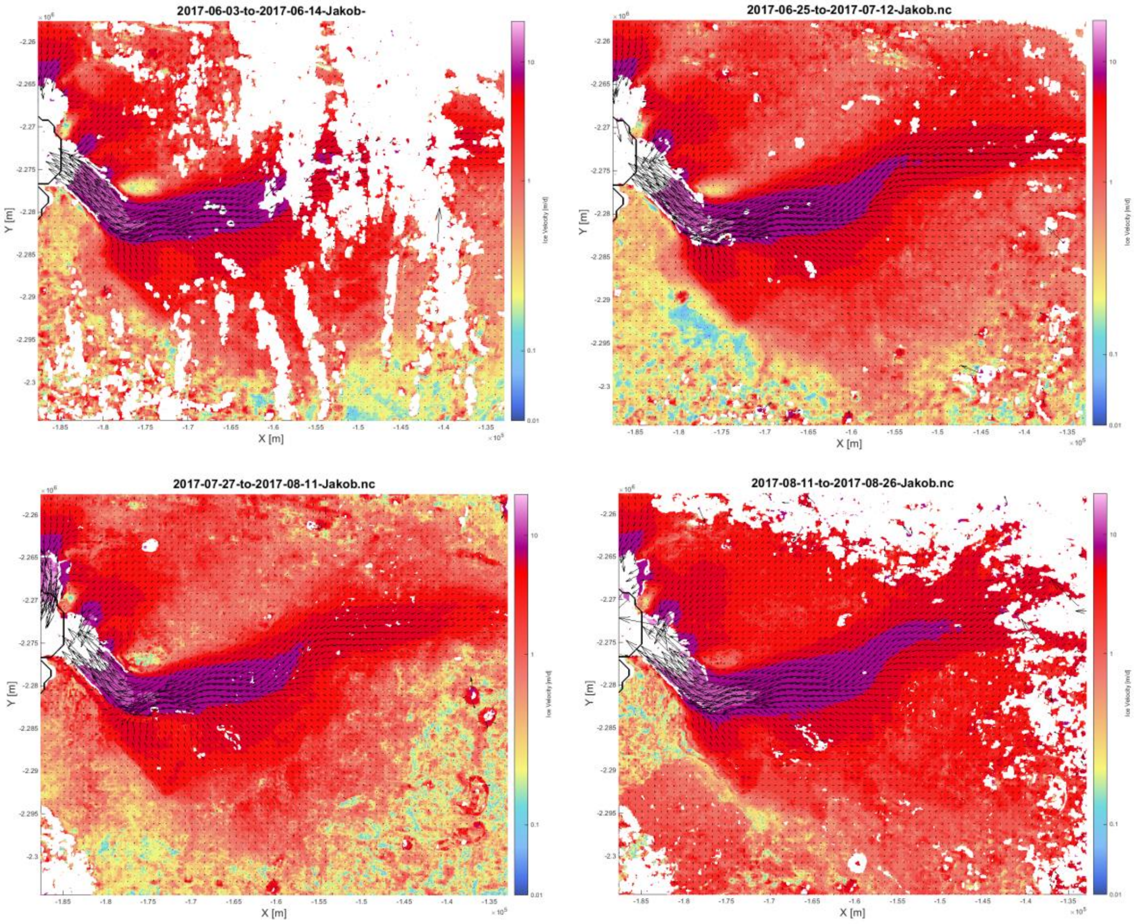

Figure 3-20: Jakobshavn Glacier – Opt IV velocity vector plots for the following time periods: 1st – 15th May 2017 (top left), 25th June – 12th July 2017 (top right), 27th July – 11th August 2017 (bottom left) and 11th – 26th August 2017 (bottom right).

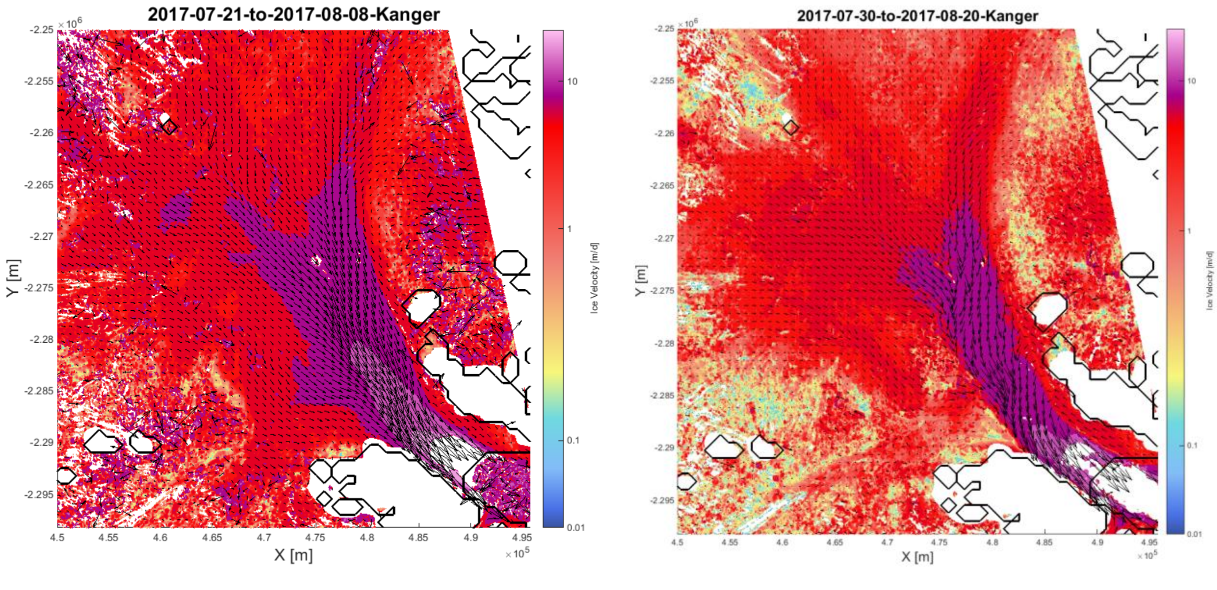

Figure 3-21: Kangerlussuaq Glacier – Opt IV velocity vector plots for the following time periods: 1st – 15th May 2017 (top left), 25th June – 12th July 2017 (top right), 27th July – 11th August 2017 (bottom left) and 11th – 26th August 2017 (bottom right).

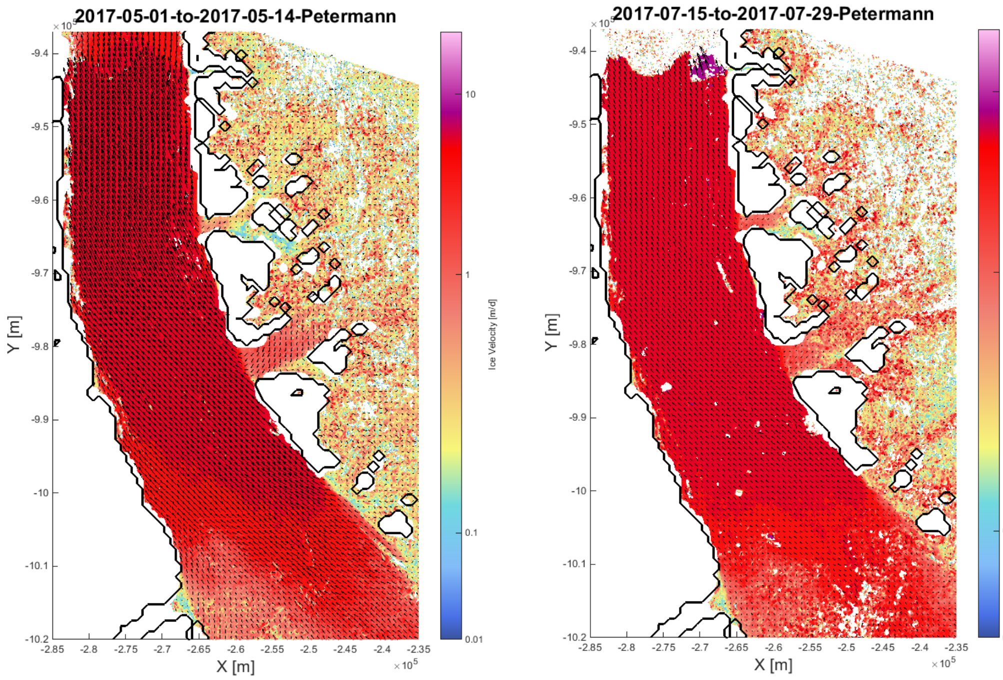

Figure 3-22: Petermann Glacier – Opt IV velocity vector plots for the following time periods: 1st – 14th May 2017 (left), 15th – 29th July 2017(right).

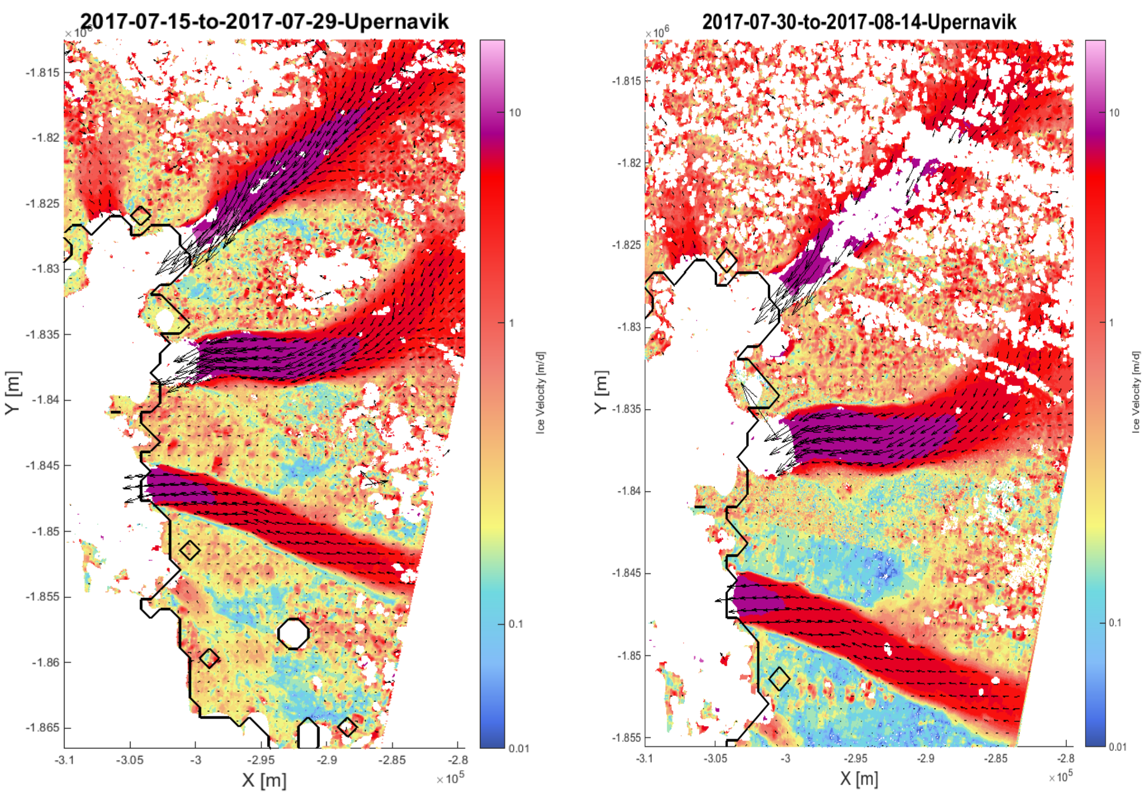

Figure 3-23: Upernavik Glacier – Opt IV velocity vector plots for the following time periods: 15th – 29th July 2017 (left), 30th July – 14th August 2017 (right).

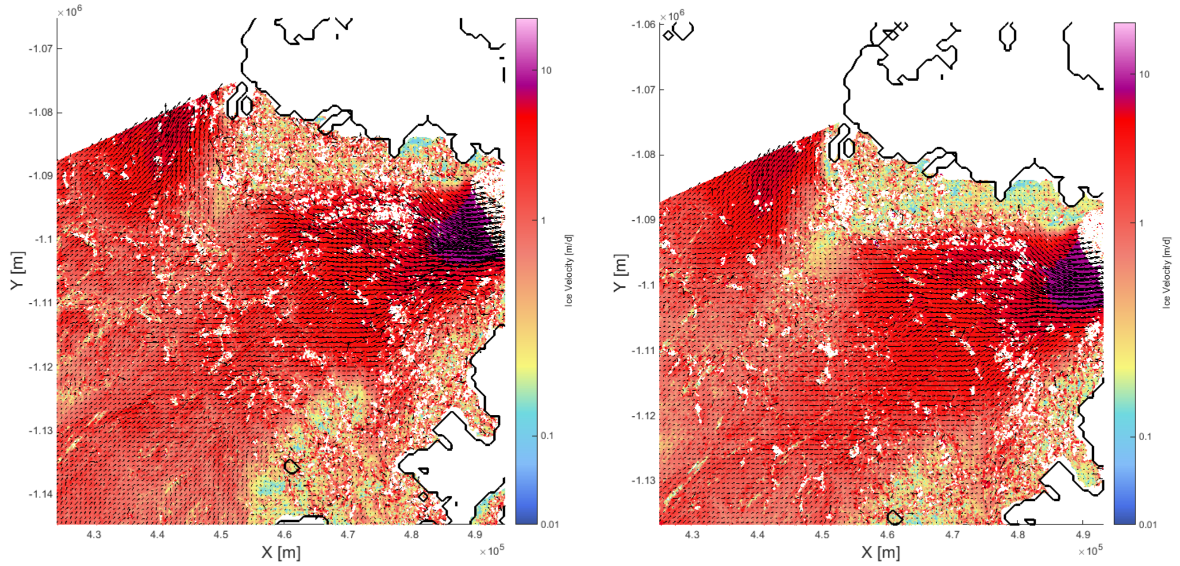

Figure 3-24: Zachariæ Glacier – Opt IV velocity vector plots for the following time periods: 25th June – 12th July 2017 (left), 13th – 27th July 2017 (right).

3.2.3 Validation procedure for validation using PROMICE SAR IV and ENVEO OptIV data products

The inter-comparison between S[&]T OptIV, PROMICE IV and ENVEO OptIV was based on:

- Scatterplots of OptIV product versus ENVEO OptIV velocity components within several Region Of Interests (ROI).
- Geographic distribution of differences of the products' velocity magnitudes.

The procedure followed to produce each scatterplot was the following:

- Projection of ENVEO OptIV and S[&]T OptIV into the same grid.
- Cropping of the pre-selected ROI.
- Visualisation of the scatterplot of the velocity component within the pre-selected ROI.

The procedure followed to produce the maps of $\Delta v_{mag} = v_{mag\,[SnT]} - v_{mag\,[data\,set]}$, where *data set* can be either ENVEO OptIV or PROMICE SAR IV, was the following:

- Projection of ENVEO OptIV, PROMICE IV and S[&]T OptIV products into the same grid.
- Interpolation of PROMICE IV to 100m resolution.
- Calculation and visualisation of Δv_{mag}.

The velocity components are defined as follows:

- v_e - The ice velocity in true meters per day in direction of the x-component of the grid defined by the map projection.
- v_n - The ice velocity in true meters per day in direction of the y-component of the grid defined by the map projection.

The analysis of the results can be found in Sections 3.2.4 and 3.2.5.

3.2.4 Validation procedure outcome vs ENVEO OptIV data product

This section details the outcomes of the validation activity performed for Hagen glacier using the ENVEO OptIV data set listed in Table 3-5. The validation outcome is presented in Figure 3-26 to Figure 3-29. Each figure is composed by two panels: the left one is a scatterplot of v_e, the right of v_n. For each velocity component, Opt IV ECV is plotted on the y-axis, with Enveo Opt IV on the x-axis. The two products cover the same time interval: 20th-30th July 2017. The ROIs on which the validation activity was performed are defined in Table 3-6.

For covering a broad variety of cases, ROIs have been selected in areas representing heterogeneous flow regimes (i.e. fast, slow, near calving front etc.). ROI 1 and ROI 2 define regions located inland: ROI 1 was selected along the flowing line of the glacier, while ROI 2 has a much larger extension (approximately 130 km²), in order to include stationary bodies, such as mountains and lakes. ROI 3 identifies an area located not far from the calving front. Finally, ROI 4 covers an area of the nearby Academy glacier, extending from the calving front inwards, for approximately 6 km². ROIs are fully characterized by the definition of their top left and bottom right corners (Table 3-6). The locations of the ROIs within Hagen and Academy glaciers are visualised in Figure 3-25.

In each figure the large majority of data points lies along or in the proximity of the red line y=x, which represent perfect correspondence between S[&]T OptIV and Enveo OptIV velocities. The small differences found in some of the plots are not considered so relevant to questioning the quality of the product. As a consequence, we can conclude that for each ROI the outcome of the validation is successful, showing good agreement between Opt IV and the validation data set velocity components.

Table 3-6: Hagen and Academy Glaciers - Top left and bottom right corners of the ROIs selected for the validation of the OptIV product versus ENVEO OptIV.

Name	Top left corner (lat, long)	Bottom right corner (lat, long)
ROI 1	(81°19’24’’, 28°58’40’’)	(81°18’54’’, 29°04’16’’)
ROI 2	(81°18’15’’, 29°27’31’’)	(81°09’55’’, 29°41’29’’)
ROI 3	(81°25’43’’, 27°36’05’’)	(81°24’53’’, 27°36’19’’)
ROI 4	(81°37’40’’,32°11’61’’)	(81°34’38’’,32°28’50’’)

Figure 3-25: Hagen Glacier – Visualization of the location of the ROIs listed in Table 3-6.

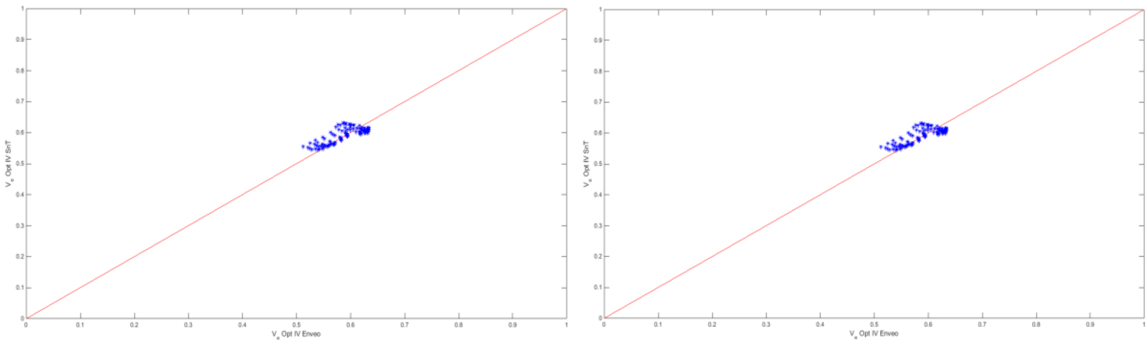

Figure 3-26: Hagen Glacier – Results of the validation of OptIV product versus ENVEO OptIV within ROI 1, for the time interval 20th -30th July 2017. The red line indicates y=x, i.e. perfect correspondence between S[&]T OptIV and Enveo OptIV velocities, expressed in m/day.

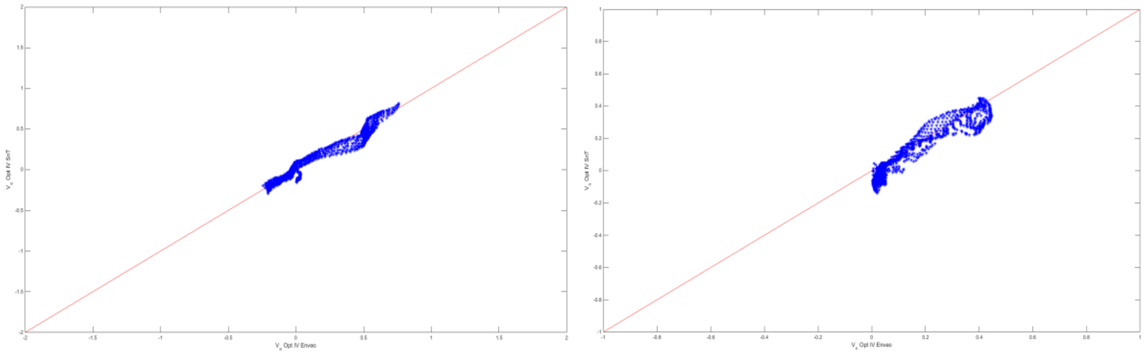

Figure 3-27: Hagen Glacier – Results of the validation of OptIV product versus ENVEO OptIV within ROI 2, for the time interval 20th -30th July 2017. The red line indicates y=x, i.e. perfect correspondence between S[&]T OptIV and Enveo OptIV velocities, expressed in m/day.

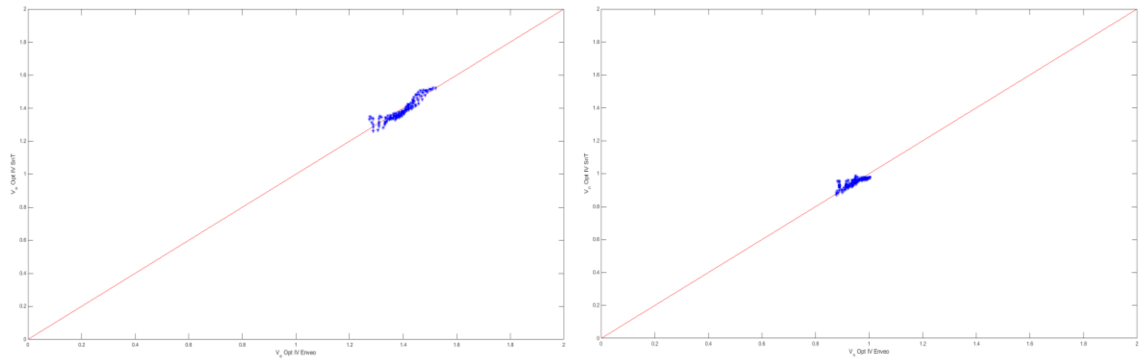

Figure 3-28: Hagen Glacier – Results of the validation of OptIV product versus ENVEO OptIV within ROI 3, for the time interval 20th -30th July 2017. The red line indicates y=x, i.e. perfect correspondence between S[&]T OptIV and Enveo OptIV velocities, expressed in m/day.

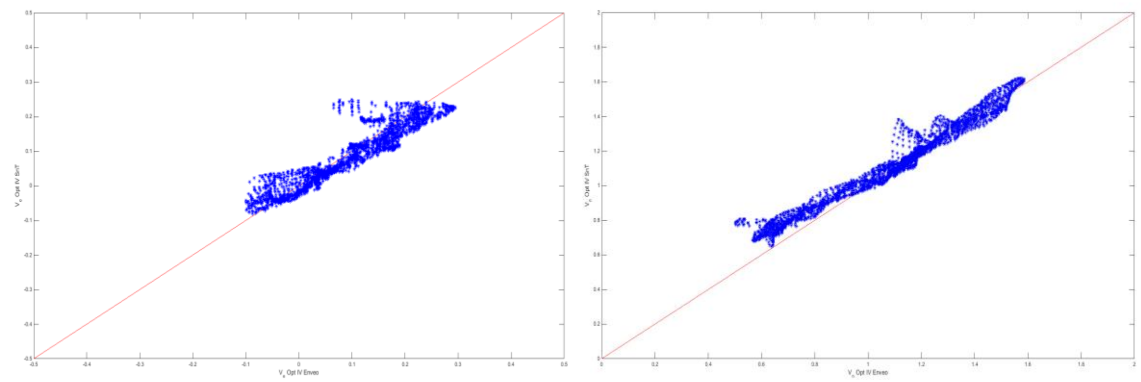

Figure 3-29: Hagen Glacier – Results of the validation of OptIV product versus ENVEO OptIV within ROI 4, for the time interval 20th -30th July 2017. The red line indicates y=x, i.e. perfect correspondence between S[&]T OptIV and Enveo OptIV velocities, expressed in m/day.

3.2.5 Validation procedure outcome vs ENVEO OptIV and PROMICE SAR IV data products

This section details the outcome of the validation activity performed on Opt IV ECV versus ENVEO OptIV and the two PROMICE SAR IV data sets listed in Table 3-5. The glacier taken into exam is Hagen. The Δv_{mag} maps are presented in Figure 3-30, Figure 3-31 and Figure 3-32. The colour scale adopted goes from blue to red. Dark blue and dark red correspond to a difference between the Opt IV ECV and the validation dataset of ±1 m/day (-1 if blue, +1 if red). The two colours gradually scale to green, which is reached when the two velocity magnitudes equal.

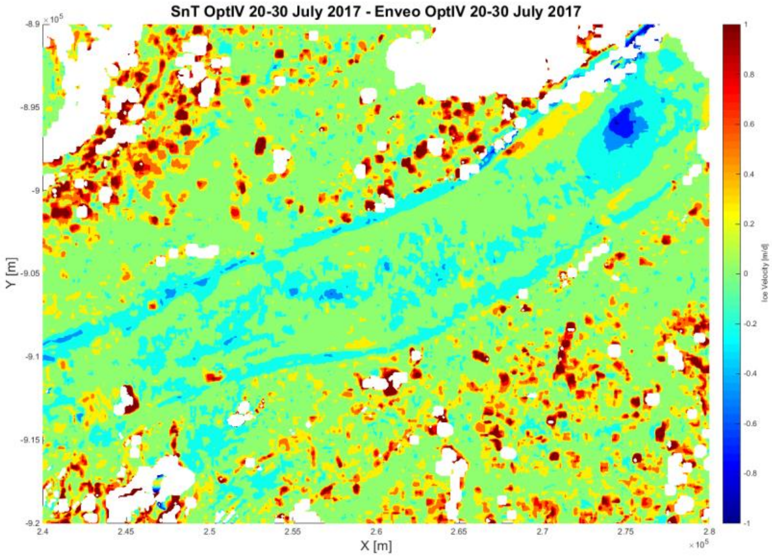

Figure 3-30: Hagen Glacier – Map of the difference of velocity magnitude between S[&]T OptIV and Enveo OptIV for the period 20th -30th July 2017. Δv_{mag} is expressed in m/day.

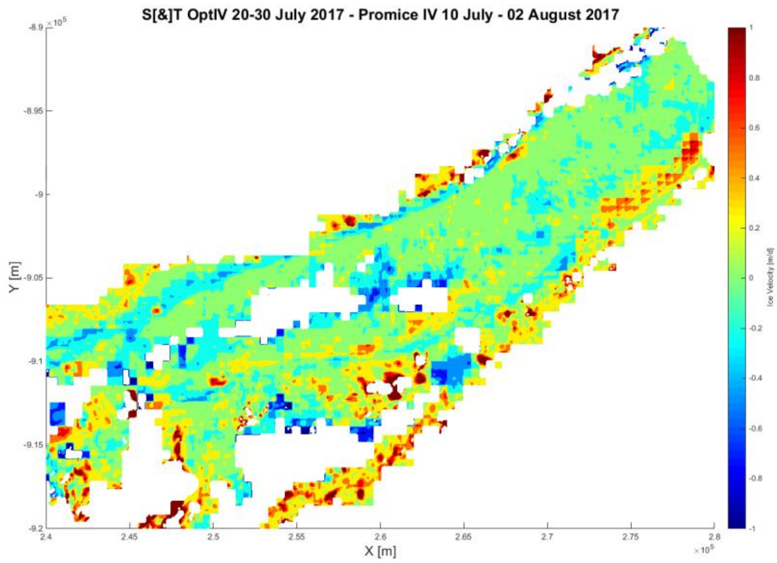

Figure 3-31: Hagen Glacier – Map of the difference of velocity magnitude between S[&]T OptIV (period 20th – 30th July 2017) and PROMICE SAR IV (period 10th July – 2nd August 2017). Δv_{mag} is expressed in m/day.

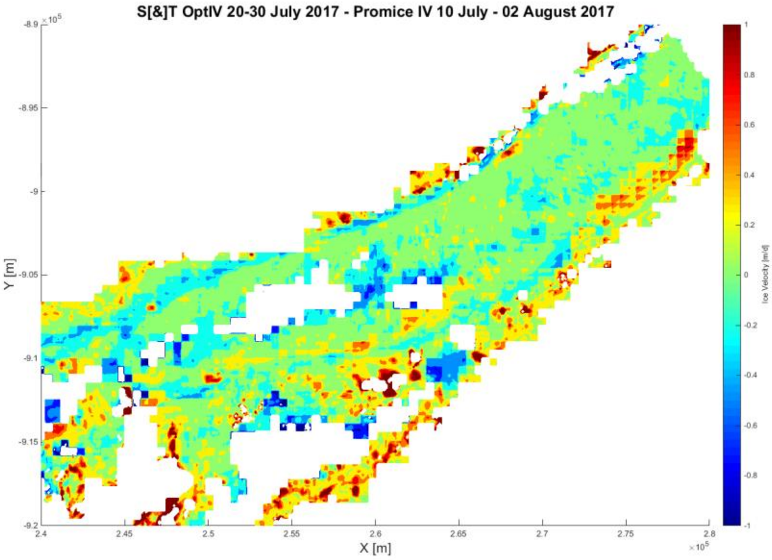

Figure 3-32: Hagen Glacier – Map of the difference of velocity magnitude between S[&]T OptIV (period 20th - 30th July 2017) and PROMICE SAR IV (period 16th July – 08th August 2017). Δv_{mag} **is expressed in m/day.**

The geographic distribution of differences of velocity magnitude between S[&]T OptIV and Enveo OptIV for the data pair 20th-30th July 2017 is presented in Figure 3-30. The two velocities show good agreement along most of the glacier, with the exception of the region near the calving front (blue region in the top left corner of the figure). Indeed, *Δv* between the two products within this region is approximately -1 m/day, due to the fact that Enveo v_{mag} increases, while S[&]T one does not. In order to investigate further the origin of this large discrepancy, the two PROMICE data sets were included in the validation activity. The two datasets cover 20-days intervals (10th July – 02nd August 2017 and 16th July – 08th August 2017), which overlap the validation period previously taken into account (20th-30th July 2017), and were generated using SAR data.

The Δv_{mag} maps comparing the OptIV ECV to the PROMICE SAR IV products are presented in Figure 3-31 and Figure 3-32. It is immediate to notice that the large discrepancy near the calving front clearly visible in Figure 3-30 is not present in neither of the Δv_{mag} maps generated. On the contrary, in both cases the magnitude of PROMICE's and S[&]T's ice velocities are in excellent agreement. Widening the analysis to the whole glacier, it is also noticeable that no large discrepancies are present when comparing the Opt IV data product to the two PROMICE data sets. We can conclude that the outcome of the validation is overall successful, showing good agreement between the products. We recommend performing further validation activity, using other independent sources and selecting a larger sample of glaciers.

3.2.6 Recommendations for product improvement

The validation described in this Section showed that the OptIV ECV can be considered reliable. Nevertheless, few, targeted validation activities should be carried out during the next phase of the project, with the goal of increasing the reliability of the products. The foreseen activities are:

- Validation of OptIV ECV with in-situ GPS data, when available.
- Validation of OptIV ECV with other independent sources, and selecting a larger sample of glaciers.
- Analysis of the estimated errors and of the strength of the correlation.

4 Calving Front Location (CFL)

This chapter gives a complete report of the activities carried out to assess the quality of the CFL products.

4.1 Sources of independent validation data

The available sources of independent validation data for the CFL product are described in the DARD and PVP documents and consist exclusively of satellite imagery, because no suitable aerial photograph, ground based photographs nor or other in situ data exist over the period and glaciers of interest.

The highest detail optical imagery available is from the SPOT IPY SPIRIT campaign. During two years from 2007 to 2009, an archive of SPOT 5 HRS images was compiled over polar land ice masses in order to produce DTMs and ortho-images. The SPIRIT (SPOT 5 stereoscopic survey of Polar Ice: Reference Images and Topographies) products that were made available comprise a panchromatic SPOT HRS orthoimage (5 m spatial resolution). The short temporal coverage of the SPOT IPY SPIRIT campaign and the very few images per year however limit its usefulness.

The next-higher resolution imagery is provided by the Advanced Spaceborne Thermal Emission and Reflection Radiometer (ASTER) instrument onboard the Terra satellite launched in December 1999. Relevant ASTER products are the three optical bands in the visible spectrum, with a nominal ground resolution of 15 m. A drawback of ASTER is the relatively small footprint (60 x 60 km).

The Enhanced Thematic Mapper (ETM+) instrument flying onboard Landsat 7 provides a panchromatic band with 15 m resolution, and three bands in the visible spectrum at 30 m resolution. Landsat 7 was launched in early 1999, and a mechanical issue developed on 31.05.2003 resulting in degraded imagery with gaps of missing data away from the central part of each scene. The Thematic Mapper (TM) sensor onboard Landsat 5, launched in 1984, provides similar products as ETM+ with the omission of the panchromatic band. Landsat 1-5 carried the Multispectral Scanner System (MSS) but its lower spatial resolution (80 m) makes it poorly suited for the purpose of CFL validation. All Landsat products cover a large footprint (185 x 185 km), which makes them particularly convenient to use, and are easily accessible through the USGS Earth Explorer website.

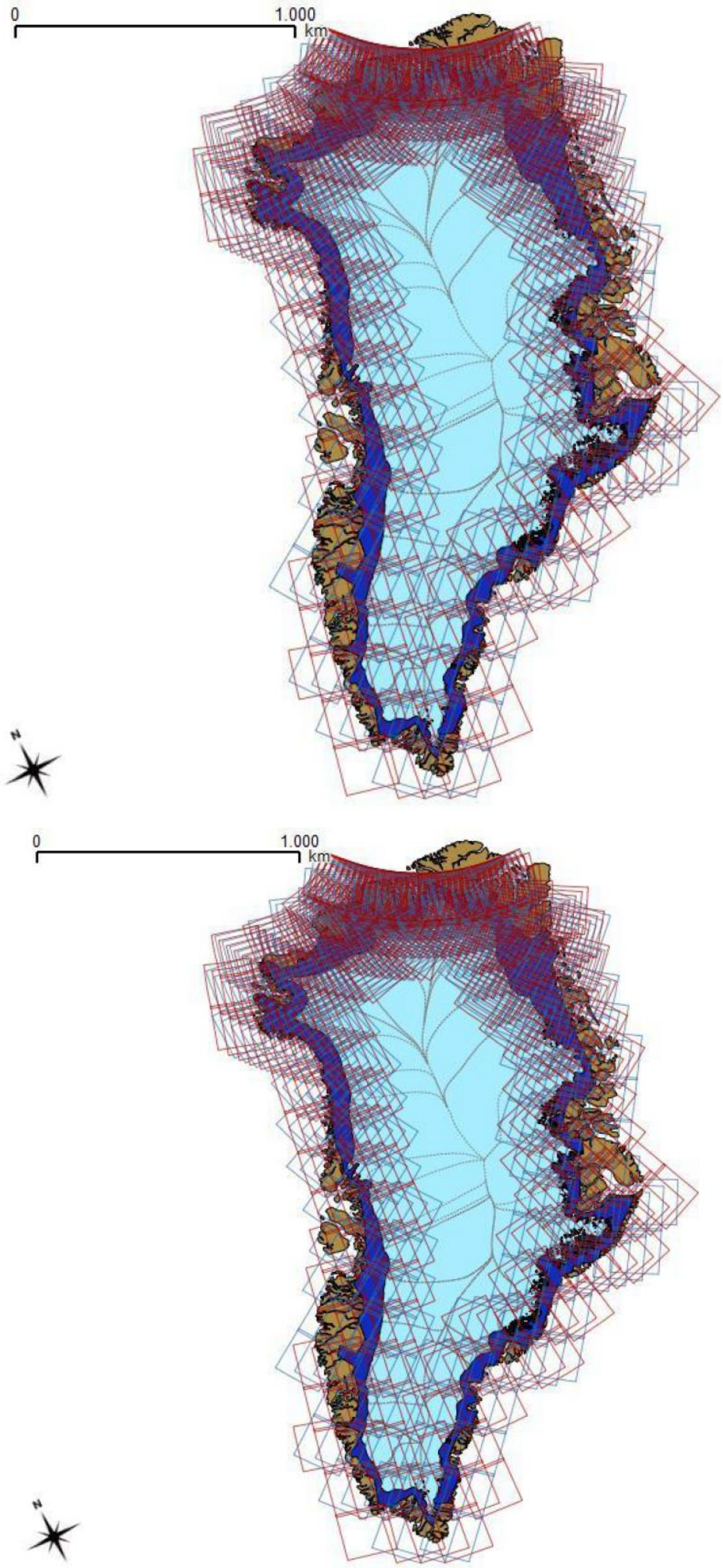

Fig. 4.1.1 – Landsat footprints coverage of the Greenland Ice Sheet margin, with 375 ascending (red squares) and 341 descending (blue squares) footprints (from DARD).

In the validation task of the CFL product, the Landsat 7 ETM+ and Landsat 5 TM products have been used exclusively. The use of these images is well established in the glaciological remote sensing community, they are available in a terrain-corrected format with good geolocation accuracy. Combined, the Landsat 5 TM and Landsat 7 ETM+ archives span the entire 1991-2010 period covered in the production of the CFL product. The dense coverage of Landsat data available at the latitude of Greenland (Figure 4.1.1) allows including in the validation different seasonal and ground conditions which can have an impact on the quality of the CFL products, like the presence of ice melange or sea ice instead of open water in front of the glacier termini.

No SPOT imagery from the IPY SPIRIT campaign has been used because their acquisition dates departed significantly from the dates of the CFL products being validated. With reference to PVP v1.2.1 Tab. 5.4 and Tab. 5.6, the closest pair was 16 days apart: SPIRIT 'CFL-VJ-3 Jakobshavn Isbræ 008 21.06.2008' and ESA-CCI-CFL 'segments_Jakobshavn_20080605_001644.shp', making a comparison meaningless. Given the target spatial accuracy of the CFL product is 250 m as specified in the PSD, using the 15 m Landsat 7 ETM+ panchromatic band in place of the SPOT 5 m resolution panchromatic band makes no practical difference.

ASTER scenes availability as surveyed in the DARD served as a fallback solution in case no suitable Landsat image was available for a given glacier and time. It did not prove necessary to use any ASTER image, the validation dataset being therefore being homogeneous and composed only of Landsat data.

4.1.1 In-situ observational data

As discussed in the DARD and PVP, no suitable in situ observational data is available for use in the validation of the CFL product.

4.1.2 Alternative products

A large collection of 629 very high quality calving front location vectors produced at GEUS during 2013 and 2014 (Schmidt-Jensen, 2014) has been used as an alternative product in the CFL validation task. These vectors have been digitized manually by a trained operator on a selection of the best Landsat images between 1999 and 2013 at 42 calving glaciers in Greenland. All 8 pairs available for comparison within 3 days between this alternative Landsat-derived dataset and the corresponding CFL product were used.

4.2 Selection of independent validation data

The DARD indicates Jakobshavn Isbræ, Kangerlussuaq, Upernavik and Kangia Nunaata Sermia as the 4 CFL priority outlets with quarterly sampling rates. PVP indicates Jakobshavn Isbræ and Kangerlussuaq as CFL validation targets, each with 4 SPIRIT orthoimages as reference for validation.

The number of CFL v.1 products for Kangerlussuaq is small (as is for Kangia Nunaata Sermia), so Upernavik B, Sermeq Avannarleq and Kangigdleq have been included in the validation as well. These three glacier have the larger number of CFL v.1 products, and they are also represented in the alternative Schmidt-Jensen (2014) dataset described in § 4.1.2 above. One CFL product from Kangia Nunaata Sermia was also included.

The need to look for additional validation regions beyond those originally planned in the DARD and PVP required searching the GEUS archive of Landsat imagery, which contains a complete collection of Landsat 1 to Landsat 8 imagery acquired over Greenland, obtained from the USGS through Earth Explorer. Out of the ca. 58,000 Landsat TM and ETM+, 15 scenes were selected based on the criteria as described below.

The resulting set of CFL and validation pairs processed is more varied and almost twice as large as planned in the PVP.

4.2.1 Validation data selection criteria

The main consideration in selecting the validation data was to match as closely as possible the acquisition date of the optical validation data and the SAR CFL product. The typical seasonal fluctuation combined with any multi-annual trend result in a change of the terminus positions during the year of a magnitude up to several kilometres, depending on the glacier. Additionally, the position and shape of the calving front can change on timescales shorter than a day when large calving events take place. Other conditions which can impact the accuracy of the CFL product, like the presence of ice melange or open water in contact with the calving front can also change rapidly. For this, all Landsat images used for validation have been acquired within 4 days of the SAR acquisition used for generating the CFL product, with the exception of one Landsat 5 image from 1996 which is 5 days from the SAR acquisition and was the only suitable scene for validation of a CFL product based on ERS1 SAR. This temporal requirement restricts very much the volume of usable validation data.

The second selection criterion directly derives from the optical nature of the validation data, which is only available during the polar day and can be contaminated by cloud cover. Images with less than 50% cloud cover were preliminarily selected from the GEUS Landsat database and visually inspected to make sure the region of interest at the glacier calving front was cloud-free.

The third criterion is of a purely technical kind and is dictated by the data gaps in the ETM+ after the Scan Line Corrector (SLC) failed on 31.05.2003. The SLC failure degraded the usability of the image away from the ground track, with increasing missing data gaps toward both sides of the image. The validation scenes where selected as much as possible so that the missing data gaps would not interfere with the manual delineation of the calving front. This further reduced the number of suitable scenes.

Finally, the remaining validation candidate pairs where narrowed down to include as far as possible examples from the different SAR missions and from different ground conditions in terms of presence of ice melange and sea ice.

4.2.2 Validation data errors and biases

There are two main error sources from the use of Landsat imagery as validation dataset. The first is the geolocation error of the Landsat scene, the second arises from incorrect or incomplete terrain elevation correction (orthorectification). All the Landsat scenes used were at the L1T processing level, meaning that the geolocation had been tied to ground control points and the topography distortions had been corrected by use of a DEM. The L1T processing is carried out by the data provider and its performance is summarized in the metadata accompanying each Landsat product.

The geolocation error is reported as rms error of the geometric model using a set of ground control points. For the purpose of this validation task, only scenes with reported rms error smaller than 15 m in both x and y directions (referred to the projected coordinates of the image) were used for ETM+ data, corresponding to the size of one pixel in the ETM+ panchromatic band. Older scenes tend to have larger errors and the threshold for Landsat 5 TM products was set to 60 m, corresponding to two TM pixels. The error of the geometric model is also available for each ground control point, but the absolute accuracy of the coordinates of the ground control points lying in the immediate surroundings of the calving front being validated is not known. Because of this, the whole-scene rms geolocation error from the metadata of each L1T processed product has been used in the calculation of the validation data uncertainty.

The errors arising from improper orthorectification are due primarily to the coarse detail and occasional errors in the DEM used in the L1T processing, and to the epoch of the DEM relative to the acquisition date of each scene. Over landforms where the elevation of the surface actually changes over time, as can be especially the case for fast flowing outlet glaciers, larger errors can occur. In order to reduce the impact of this error source, for the purpose of the CFL validation the scenes were selected as close to nadir view as available, and a correction proportional to the local DEM height above sea level, the local deviation from nadir view, and the orientation of the terminus relative to the satellite was applied to the validation calving front vectors. Empirically, the largest orthorectification errors are most commonly found in regions of steep terrain with narrow peaks and deep valleys. The regions of interest for the CFL validation are close to sea level and have relatively low slopes, resulting in corrections between -7.6 to +51.9 m (rms over all validation scenes: 19.2 m).

Finally, a third small error arises from the interaction of the geolocation error with the local slope and aspect of the DEM used in the L1T processing. The geolocation error is very small compared with the length scale of features in the DEM, which are very smooth being derived from coarse elevation information, and as a result we assume this error component to be negligible.

The two main uncertainties (geolocation error and orthorectification error) are independent and the Landsat validation data uncertainty was calculated as their root-squared-sum. Over the entire validation set the validation data uncertainty varies between 30.2 and 74.26 m (average 33.2 m). The combined uncertainty of the CFL and validation datasets (uncertainty of the distance between CFL and validation front positions) is dominated by the uncertainties of the CFL product, which is provided in the CFL shapefiles and ranges between 60 and 120 m depending on the pixel size of the source data.

4.2.3 Validation data uncertainty

The uncertainty inherent in the nature of the validation data is essentially due to changes in the calving front occurring in the intervening time between the acquisition of the SAR and the Landsat image.

Large calving events during this time will result in correspondingly large differences between CFL and validation, localized to a sector of the front if the calving event did not affect the entire width of the terminus. Calving events of any size introduce a time-dependent difference between CFL and validation which grows in magnitude as the lag between acquisition dates of the SAR and Landsat pairs used for validation. To minimize this uncertainty, the time lag between SAR and Landsat acquisitions is the shortest possible (in the order of days) for the pairs chosen for validation.

Competing with terminus changes due to calving, glacier flow tends to continuously bring the terminus forward in between calving events. When calving does not primarily occur as very frequent small events but in the form of relatively large and infrequent events separated by several days or weeks of gradual advance, individual validation comparisons may reflect this terminus advance due to glacier flow more often than the overall seasonal retreat.

Care has been exercised to identify possible hints of recent large calving events from the detailed shape of the calving front in the CFL and validation digitization; however it is not possible to rule out such events entirely, or to estimate their magnitude. It is therefore anticipated that some of the differences found comparing CFL and Landsat images do correspond to real changes of the terminus occurred between the acquisition dates of data pairs.

The uncertainty of the CFL validation (uncertainty of the distance between CFL and validation front positions) is dominated by the uncertainties of the CFL product, which is provided in the CFL shapefiles and ranges between 60 and 120 m depending on the pixel size of the source data. The error sources of the the CFL and validation datasets are independent, and the uncertainty of the CFL validation was calculated as their root-squared-sum and the result reported in Tables 4.4.1 and 4.4.2.

4.3 Validation procedure

The steps followed in the validation procedure were the same for all pairs of control and CFL products, irrespective that validation data came from the Schmidt-Jensen (2014) dataset or were produced specifically for the CFL validation. Geolocated tiff files of the panchromatic band (for ETM+) or band 3 (for TM) were loaded in a desktop GIS application (ArcGIS for the Schmidt-Jensen, 2014 vectors, and QGIS for all other vectors) and the terminus position was manually digitized at high magnification by a trained operator. Manual outlining of clearly recognizable glacier margins is generally found to be accurate within about 1 pixel size (Paul et al, 2013), however we conservatively double this in our uncertainty estimate in view of the higher difficulty in digitizing calving fronts compared with most land-terminating glacier margins.

Digitization of the validation calving fronts is carried out in the same map projection of the Landsat scene, i.e. the local UTM zone. The CFL products are delivered in WGS84 geographic coordinates (EPSG: 4326) and are therefore projected to the same UTM zone as the validation vectors at this step. By working in the local UTM zone we minimize distance errors due to scale variation of the UTM projection, which is less than 0.1% within any zone everywhere on the globe (Snyder, 1987).

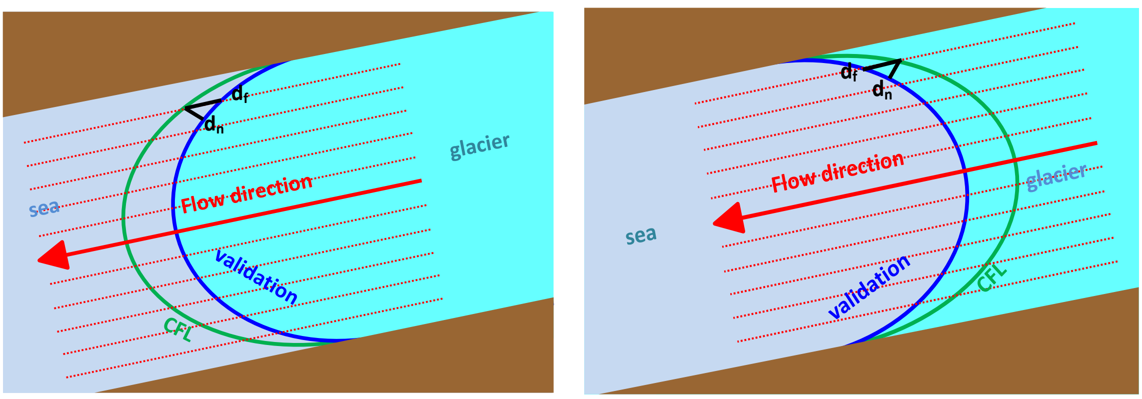

Fig. 4.3.1 – Diagram illustrating the d_n and d_f metrics at convex and concave glacier termini. The two metric would provide identical results for perfectly straight glacier termini.

Once the calving front were digitized on the Landsat image and the CFL product were projected to the same UTM zone, the distance between the two lines was measured every 5 m across the entire length of the calving front and using two different metrics (Fig. 4.3.1):

- distance to the nearest point of the validation dataset (d_n)
- distance along the direction of glacier flow determined at the central flowline (d_f)

A feature of many calving fronts is their curvature, with the faster flowing central sector of the tongue either more advanced or more retreated than where the calving front approaches the fjord sides (Fig. 4.3). Due to this geometry, minor inaccuracies close to the fjord sides can translate into large errors when the metric use to report them is distance along the direction of glacier flow determined at the central flowline. It was therefore decided to exclude the outermost 10% from both ends of the calving front in the calculation of the d_f metric. In order to assess the accuracy of the CFL product over the entire width of the glacier, the d_n metric was instead calculated over the entire front, including the outermost 10%.

The geometric procedure of measuring d_f and d_n was carried out automatically and the results for each CFL and validation pair were output in table format and as a distance plot with error bands.

For both metrics, the following statistics were produced and reported in §4.4, together with plots of the distance and uncertainty: rms distance, mean distance, median distance, minimum distance and maximum distance. Finally, the fraction of measured distances including uncertainties falling outside a ±250 m band was calculated.

4.4 Validation procedure outcome

This section describes the outcome of the validation process comparing the SAR-derived CFL products and Landsat-derived validation products. In addition to the statistics of the d_f and d_n metrics discussed in § 4.3, the dates and sensor of the SAR and Landsat image pairs are also provided, together with fjord conditions at the contact with the calving front which may have an impact on the accuracy of the CFL product. These conditions are the presence of ice melange, sea ice or open water.

glacier name	date			d_n distance from CFP to validation					distance	CFP within	terminus	source	
	CFL	validation	lag	rms	median	min	mean	max	uncertainty	+/- 250 m	conditions	CFL	validation
			days	m	m	m	m	m	m	of validation			
Jakobshavn	2004.09.09	2004.09.08	1	89.9	-19.7	-306.0	-26.3	154.2	67.6	1.00	ice melange	ENVISAT ASAR	Lansat 7 ETM+
Jakobshavn	2004.09.09	2004.09.10	-1	188.0	7.1	-275.8	56.9	576.9	67.2	0.86	ice meange	ENVISAT ASAR	Lansat 7 ETM+
Jakobshavn	2007.06.21	2007.06.22	-1	235.8	-42.1	-774.0	-17.6	767.9	67.2	0.84	ice meange	ENVISAT ASAR	Lansat 7 ETM+
Jakobshavn N	2009.09.03	2009.08.30	4	313.7	65.4	-724.5	-80.9	263.8	67.2	0.75	ice meange	ENVISAT ASAR	Lansat 7 ETM+
Jakobshavn S	2009.09.03	2009.08.30	4	120.9	10.6	-192.8	24.9	355.6	67.2	0.98	ice meange	ENVISAT ASAR	Lansat 7 ETM+
Kangerdlugssuaq	2008.08.12	2008.08.07	5	89.4	45.0	-269.5	24.0	171.6	124.0	1.00	ice meange	ENVISAT ASAR	Lansat 7 ETM+
Upernavik B	2004.09.12	2004.09.09	3	88.4	80.1	9.7	82.4	158.1	67.7	1.00	ice meange	ENVISAT ASAR	Lansat 7 ETM+
Upernavik B	2006.09.17	2006.09.17	0	60.7	56.3	-37.5	53.7	113.4	67.2	1.00	ice melange	ENVISAT ASAR	Lansat 7 ETM+
Upernavik B	2009.08.29	2009.08.31	-2	38.4	30.1	-90.0	20.9	68.7	67.2	1.00	ice melange	ENVISAT ASAR	Lansat 7 ETM+
Kangia Nunaata S.	1993.04.19	1993.04.15	4	5627.3	5458.4	4608.4	5613.7	6345.0	141.1	0.00	sea ice	ERS1 SAR	Lansat 5 TM
Sermeq Avannarleq	2006.08.13	2006.08.13	0	94.8	-90.9	-155.1	-90.6	0.9	123.9	1.00	open water	ENVISAT ASAR	Lansat 7 ETM+
Kangigdleq N	2006.08.10	2006.08.13	-3	249.9	253.0	167.0	245.9	330.2	123.8	1.00	open water	ENVISAT ASAR	Lansat 7 ETM+
Kangigdleq N	2008.08.14	2008.08.16	-2	249.0	252.5	168.8	244.9	323.1	123.9	1.00	open water	ENVISAT ASAR	Lansat 7 ETM+
Kangigdleq N	2010.08.15	2010.08.16	-1	374.7	381.9	275.3	370.0	509.1	123.8	0.41	open water	ENVISAT ASAR	Lansat 7 ETM+
Kangigdleq S	2006.08.10	2006.08.13	-3	125.9	-71.6	-257.4	-85.6	93.5	123.8	1.00	open water	ENVISAT ASAR	Lansat 7 ETM+
Kangigdleq S	2008.08.14	2008.08.16	-2	158.1	-137.9	-245.9	-117.0	260.8	123.9	1.00	open water	ENVISAT ASAR	Lansat 7 ETM+
Kangigdleq S	2010.08.15	2010.08.16	-1	176.8	-164.2	-272.4	-139.5	226.0	123.8	1.00	open water	ENVISAT ASAR	Lansat 7 ETM+

Table 4.4.1 – Validation results using the d_n metric (distance to the nearest point of the validation dataset).

glacier name	date			d_f distance from CFP to validation					distance	CFP within	terminus	source	
	CFL	validation	lag	rms	median	min	mean	max	uncertainty	+/- 250 m	conditions	CFL	validation
			days	m	m	m	m	m	m	of validation			
Jakobshavn	2004.09.09	2004.09.08	1	121.0	0.7	-210.6	8.8	600.5	67.6	0.97	ice meange	ENVISAT ASAR	Lansat 7 ETM+
Jakobshavn	2004.09.09	2004.09.10	-1	240.9	55.1	-333.9	115.3	669.7	67.2	0.76	ice meange	ENVISAT ASAR	Lansat 7 ETM+
Jakobshavn	2007.06.21	2007.06.22	-1	380.2	-42.6	-1032.1	13.9	1014.5	67.2	0.75	ice meange	ENVISAT ASAR	Lansat 7 ETM+
Jakobshavn N	2009.09.03	2009.08.30	4	369.6	74.9	-764.2	-83.4	1013.7	67.2	0.70	ice meange	ENVISAT ASAR	Lansat 7 ETM+
Jakobshavn S	2009.09.03	2009.08.30	4	294.8	-6.1	-221.2	94.7	1028.0	67.2	0.83	ice meange	ENVISAT ASAR	Lansat 7 ETM+
Kangerdlugssuaq	2008.08.12	2008.08.07	5	158.5	66.8	-725.5	31.9	247.5	124.0	0.96	ice meange	ENVISAT ASAR	Lansat 7 ETM+
Upernavik B	2004.09.12	2004.09.09	3	97.2	88.1	21.3	92.0	162.3	67.7	1.00	ice meange	ENVISAT ASAR	Lansat 7 ETM+
Upernavik B	2006.09.17	2006.09.17	0	72.0	67.0	14.2	68.3	127.0	67.2	1.00	ice melange	ENVISAT ASAR	Lansat 7 ETM+
Upernavik B	2009.08.29	2009.08.31	-2	47.5	35.5	-93.2	33.8	103.5	67.2	1.00	ice melange	ENVISAT ASAR	Lansat 7 ETM+
Kangia Nunaata S.	1993.04.19	1993.04.15	4	6217.3	5899.2	5650.2	6188.5	7500.8	141.1	0.00	sea ice	ERS1 SAR	Lansat 5 TM
Sermeq Avannarleq	2006.08.13	2006.08.13	0	112.9	-108.6	-225.0	-108.6	2.1	123.9	1.00	open water	ENVISAT ASAR	Lansat 7 ETM+
Kangigdleq N	2006.08.10	2006.08.13	-3	311.3	288.6	178.4	303.2	409.4	123.8	0.69	open water	ENVISAT ASAR	Lansat 7 ETM+
Kangigdleq N	2008.08.14	2008.08.16	-2	321.3	330.4	174.6	311.6	429.9	123.9	0.71	open water	ENVISAT ASAR	Lansat 7 ETM+
Kangigdleq N	2010.08.15	2010.08.16	-1	444.4	448.1	284.3	437.2	532.4	123.8	0.22	open water	ENVISAT ASAR	Lansat 7 ETM+
Kangigdleq S	2006.08.10	2006.08.13	-3	148.0	-108.4	-299.3	-109.7	32.5	123.8	1.00	open water	ENVISAT ASAR	Lansat 7 ETM+
Kangigdleq S	2008.08.14	2008.08.16	-2	177.9	-157.5	-272.6	-170.8	-59.2	123.9	1.00	open water	ENVISAT ASAR	Lansat 7 ETM+
Kangigdleq S	2010.08.15	2010.08.16	-1	209.1	-200.8	-336.3	-203.9	-114.1	123.8	1.00	open water	ENVISAT ASAR	Lansat 7 ETM+

Table 4.4.2 – Validation results using the d_f metric (distance along the direction of glacier flow determined at the central flowline).

Of the 17 CFL and validation pairs considered, the calving fronts are entirely within ±250 m of each other for 11 pairs according to the d_n metric, and for 7 pairs according to the d_f metric, once allowing for the combined uncertainties of the CFL and the validation datasets (Tables 4.4.1 and 4.4.2).

Furthermore, 15 and 12 pairs respectively for the d_n metric and the d_f metric have at least 75% of their calving fronts within ±250 m of each other, once allowing for the combined uncertainties of the CFL and the validation datasets.

Of the remaining pairs, the most problematic one is from Kangia Nunaata Sermia in 1993 (§ 4.4.1.9), where it is clear that the CFL product, based on ERS1 SAR, misinterpreted sea ice features in the fjord for the glacier terminus, resulting in errors of several kilometres. Due to the very limited opportunities to validate CFL from older dates and from fjord conditions with sea ice, it is not possible to univocally explain this issue in terms of fjord conditions or lower quality of ERS1 SAR data compared to ENVISAT ASAR.

The CFL appears to consistently map the northern terminus of Kangigdleq in a position a few hundreds of metres too advanced. At this site it was possible to find three validation pairs (in 2006, 2008 and 2010), and they all show this bias. The southern terminus of the same glacier from the very same CFL and Landsat dates show smaller and opposite errors (§§ 4.4.1.10 – 4.4.1.16), making the bias difficult to explain as incorrect geolocation of either the CFL or validation products.

As expected, the d_f metric results in the largest difference between CFL and validation at all glaciers, even after excluding the outermost 10% at both ends of the calving fronts (§4.3). Ice melange in contact with the terminus doesn't seem linked to larger CFL errors, even though the validation sample is rather limited due to the availability of matching dates in the CFL and validation datasets. When studying the sites of largest d_f and d_n it is clear that rapid changes of the terminus, resulting both from fast glacier flow and from strong calving activity, are responsible for some of the observed differences between CFL and validation. This was anticipated and it cannot be avoided entirely (§4.3.2). A particularly favourable case is provided by Jakobshavn Isbræ in September 2004, when two Landsat 7 ETM+ are available from the day before and the day after the ENVISAT ASAR acquisition used for the CFL product (§ 4.4.1.1). A relatively large calving event occurred within these three days at the southern flow unit and gave rise to a large localized difference between CFL and validation (Fig. 4.4.1.1.2), both for the d_f as well as for the d_n metric.

A limitation of the current validation results is the need to include validation data from a few days before or after the date of CFL data in order to have a sufficient number of validation pairs. To investigate the impact of this temporal lag, a scatter plot of median d_n vs. lag expressed in days between SAR and Landsat acquisition is shown in Fig. 4.4.1. In the figure, positive lags correspond to SAR acquired at a later date than Landsat, consistently with Tables 4.4.1 and 4.4.2. The points in Fig. 4.4.1 include all pairs of CFL and validation calving fronts after excluding the problematic points from Kangia Nunaata Sermia and the northern terminus of Kangigdleq, which have larger errors as discussed above.

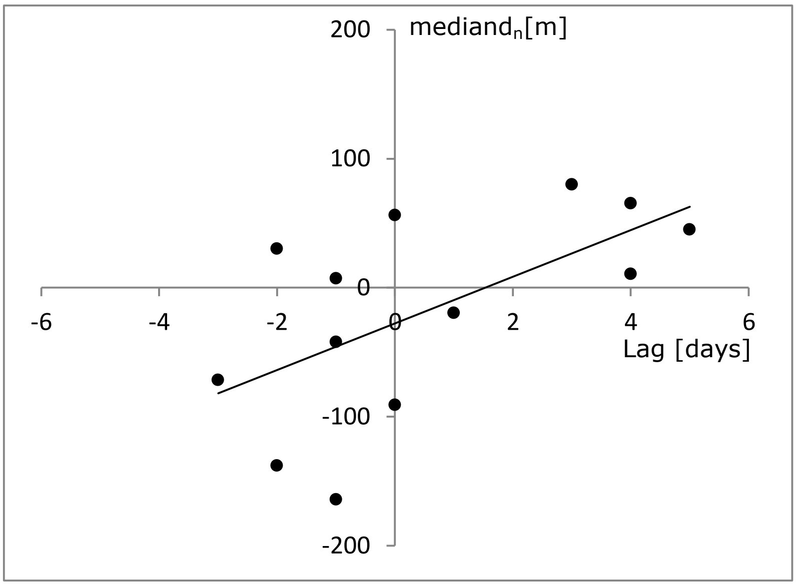

Fig. 4.4.1 - median d_n vs. lag expressed in days between SAR and Landsat acquisition. The trend line shows the least squares linear fit, neglecting that the points represent different glaciers.

The processes discussed in § 4.2.3 act over temporal and spatial scales which are characteristic for each glacier (and may in general change over time even at the same site), while Fig. 4.4.1 mixes points belonging to 5 glaciers. From a statistical point of view the points in Fig. 4.4.1 are samples known to derive from different populations. Consequently, it is not meaningful to analyse Fig. 4.4.1 and the apparent trend it shows quantitatively. With this in mind, it is nevertheless useful to visually inspect and qualitatively discuss Fig. 4.4.1.

In terms of the processes discussed in § 4.2.3, the positive slope of the apparent trend in Fig. 4.4.1 is consistent with glacier flow gradually bringing forward the terminus in-between large calving events. Some d_n scatter may be explained by calving events in the intervening time between SAR and Landsat acquisition. However, median d_n values are rather insensitive to calving events affecting only a sector of the entire terminus, and very large calving events affecting the entire terminus are relatively rare, therefore other uncertainties in the CFL and validation products are likely responsible for most observed d_n scatter. Closer inspection of the three largest negative differences (i.e. CFL terminus less advanced than Landsat terminus) show that these points refer to the southern terminus of Kangigdleq in 2010 and 2008, and to Sermeq Avannarleq in 2006. The Sermeq Avannarleq CFL product appears clearly shifted compared to the same-day validation reference (Fig. 4.4.1.16). As to Kangigdleq, a glacier velocity in the order of 200 m/day in 2010 and 100 m/day in 2008 would be needed to justify the difference between CFL and validation, which is unrealistic. It is possible these differences result from different layover and shadow characteristics that can affect the appearance of the calving cliff in the SAR image. The three validation pairs at Upernavik B may also indicate a similar effect, albeit of a much smaller magnitude. Finally, the dispersion of median d_n values appears roughly comparable in Fig. 4.4.1 with the effect of 5 days of lag between SAR and Landsat acquisition, which is the maximum allowed within the validation pairs.

Further discussion of validation results is most conveniently combined with the images and plots of each validation pair and is provided below in § 4.4.1

4.4.1 Validation results by glacier

The following sections § 4.4.1.1 – 4.4.1.16 details the validation outcomes for each of all CFL and validation pair analysed. In all distance plots, the horizontal axis is oriented such that the glacier flows from the bottom toward the top of the chart. Consequently, the horizontal coordinate is expressed as metres from the orographic left side of the glacier tongue.

The width of the error bands on either side of the red and blue distance lines corresponds to the 'distance uncertainty' column in Tables 4.4.1 and 4.4.2 for the d_f and d_n metrics, respectively.

4.4.1.1 JakobshavnIsbræ, 2004

The fjord in front of Jakobshavn Isbræ shows a dense and coarse ice melange in direct contact with the terminus. This CFL product date provides a rare opportunity of validation against Landsat ETM+ imagery acquired both on the previous and on the following day from the ENVISAT acquisition.

Comparing Fig. 4.4.1.1.1 and 4.4.1.1.2 shows how rapidly the terminus of fast flowing outlets can change, and the corresponding impact on the validation results.

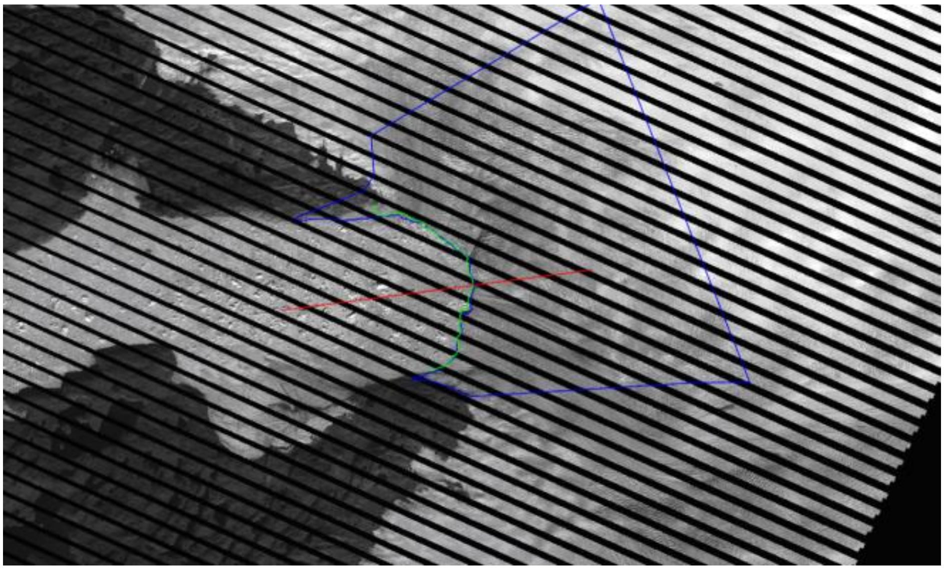

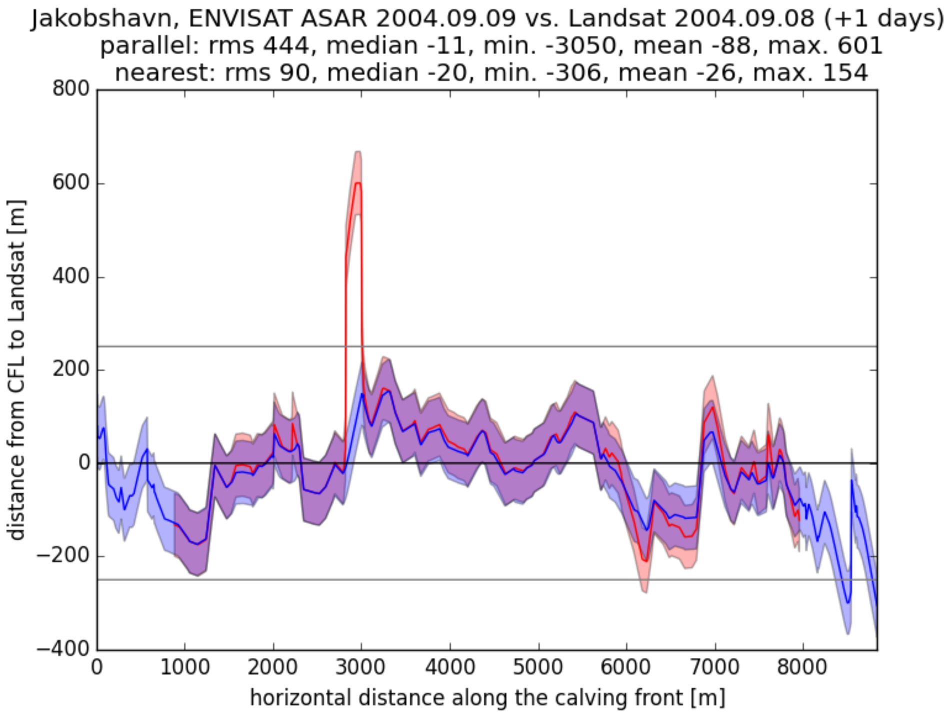

Fig. 4.4.1.1.1 –Jakobshavn, 2004. Top: CFL (green line) based on ENVISAT ASAR, validation data based on Landsat ETM+ from one day earlier (blue line) and flow direction (red), plotted on the Landsat panchromatic band. Bottom: distances measured parallel to glacier flow are plotted in red, distances from the CFL vector to the nearest validation vector are plotted in blue. Positive distances indicate the front is more advanced in the CFL than in the validation dataset. Grey lines mark the ±250 m range.

The largest discrepancy between Fig. 4.4.1.1.1 and 4.4.1.1.2 coincides with the most active part of the southern flow unit, where a large iceberg was still connected to the terminus on the day before the ENVISAR acquisition (Fig. 4.4.1.1.1), and it had barely detached on the day after the ENVISAR acquisition (Fig. 4.4.1.1.2).

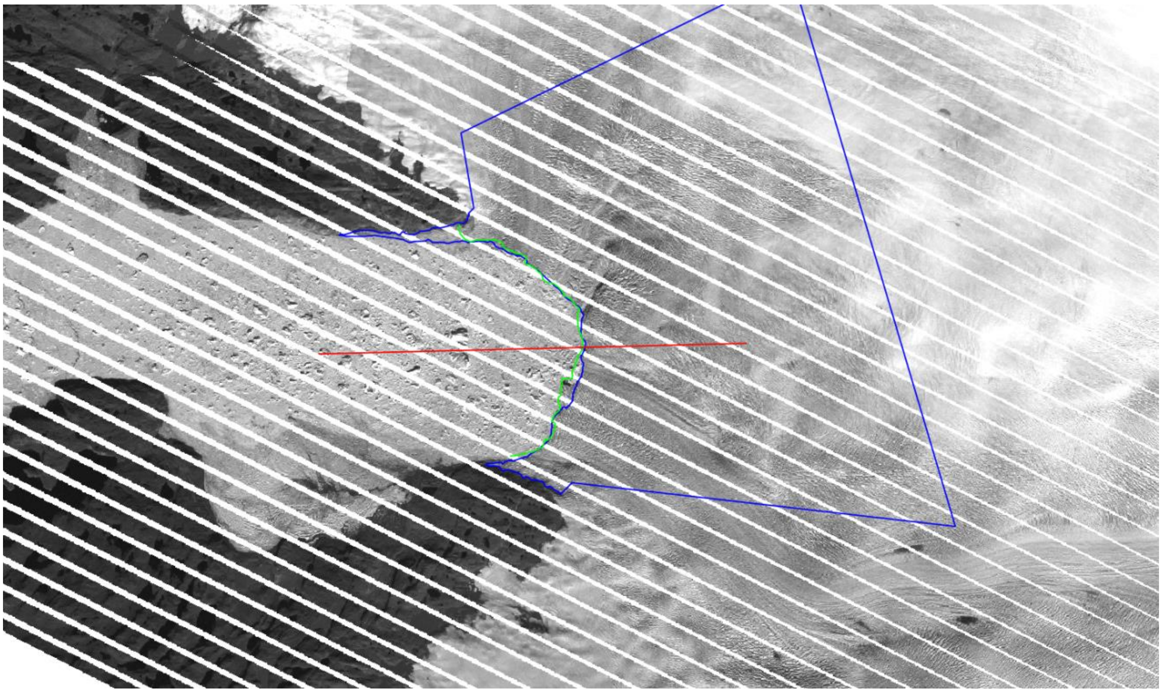

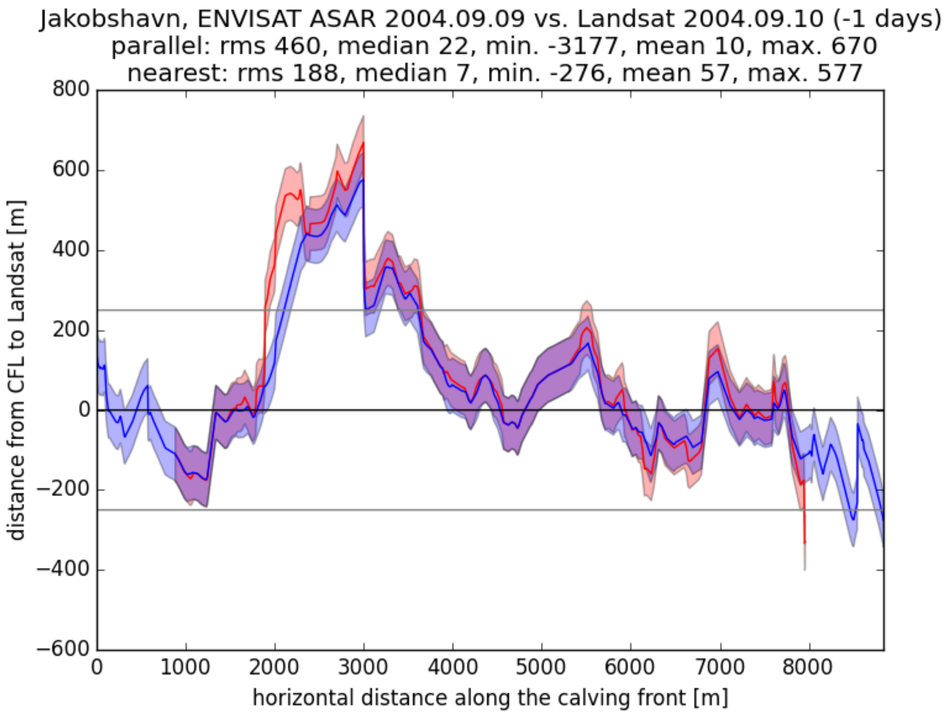

Fig. 4.4.1.1.2 –Jakobshavn, 2004. Top: CFL (green line) based on ENVISAT ASAR, validation data based on Landsat ETM+ from one day later (blue line) and flow direction (red), plotted on the Landsat panchromatic band. Bottom: distances measured parallel to glacier flow are plotted in red, distances from the CFL vector to the nearest validation vector are plotted in blue. Positive distances indicate the front is more advanced in the CFL than in the validation dataset. Grey lines mark the ±250 m range.

4.4.1.2 JakobshavnIsbræ, 2007

The fjord in front of Jakobshavn Isbræ shows a dense and coarse ice melange in direct contact with the terminus.

The large discrepancy between CFL and validation data corresponds to a chaotic area, part of which is not easily mapped from Landsat as well.

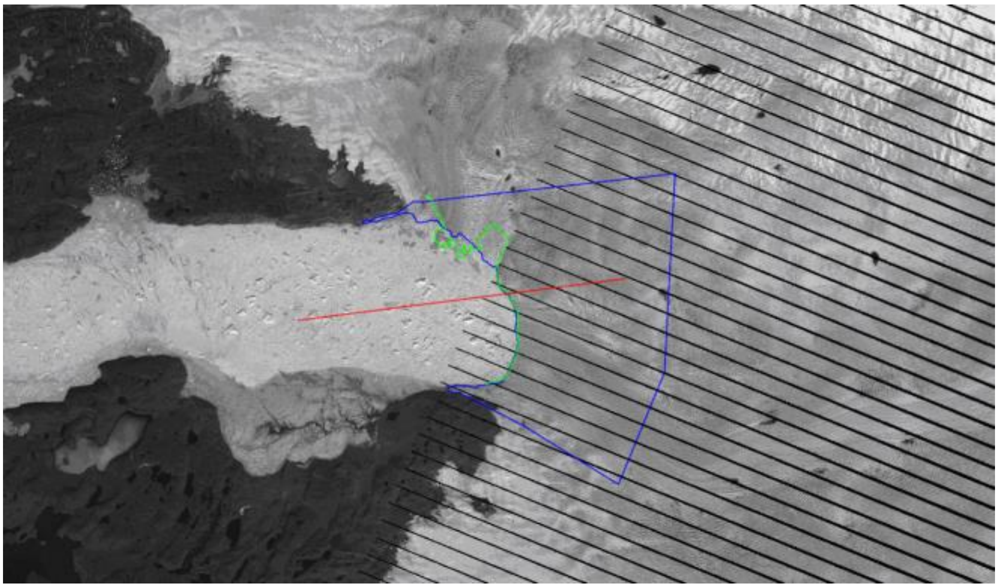

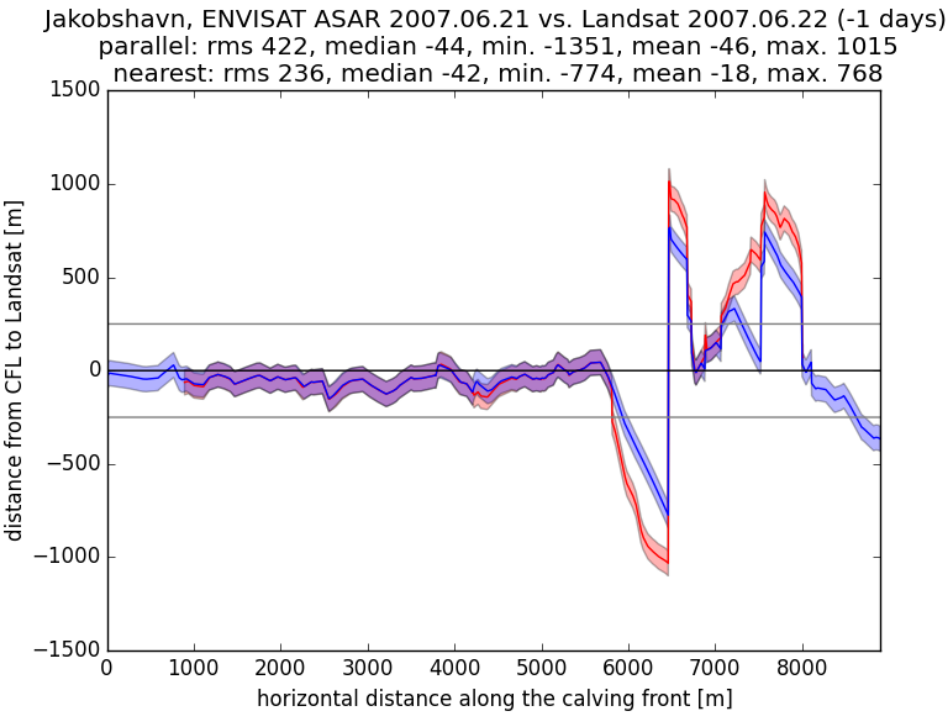

Fig. 4.4.1.2 –Jakobshavn, 2007. Top: CFL (green line) based on ENVISAT ASAR, validation data based on Landsat ETM+ (blue line) and flow direction (red), plotted on the Landsat panchromatic band. Bottom: distances measured parallel to glacier flow are plotted in red, distances from the CFL vector to the nearest validation vector are plotted in blue. Positive distances indicate the front is more advanced in the CFL than in the validation dataset. Grey lines mark the ±250 m range.

4.4.1.3 JakobshavnIsbræ, northern sector, 2009

The calving front in 2008 of Jakobshavn Isbræ was processed as two separate sectors with different flow directions.

The large discrepancy in the northern sector corresponds to the same chaotic area which was also problematic in the 2007 product (§ 4.4.1.2).

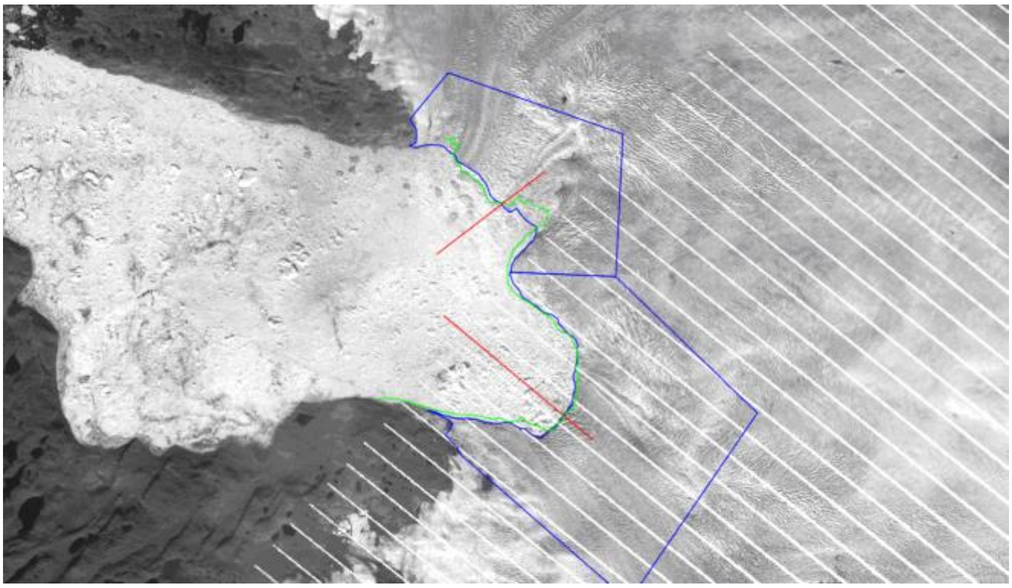

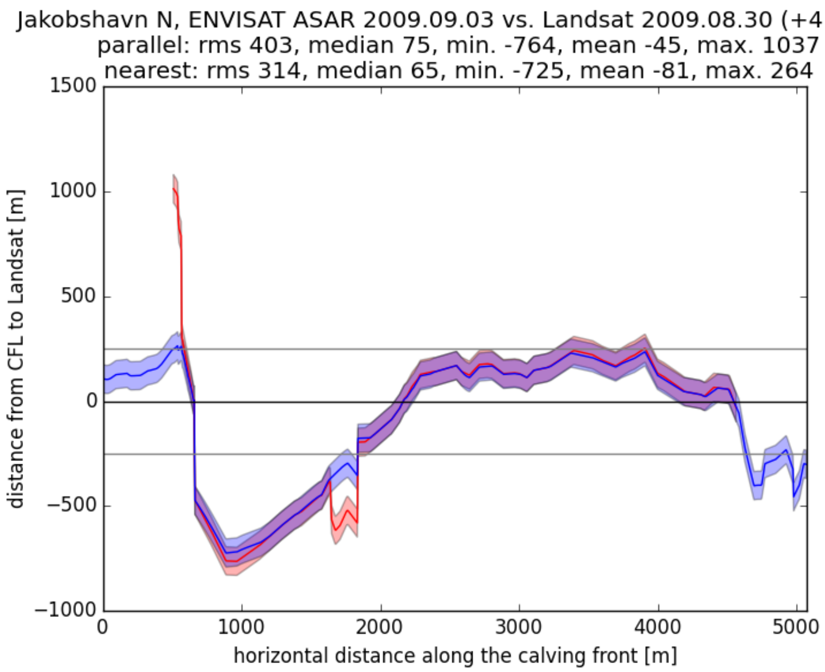

Fig. 4.4.1.3 –Jakobshavn, northern sector, 2009. Top: CFL (green line) based on ENVISAT ASAR, validation data based on Landsat ETM+ (blue line) and flow direction (red), plotted on the Landsat panchromatic band. Bottom: distances measured parallel to glacier flow are plotted in red, distances from the CFL vector to the nearest validation vector are plotted in blue. Positive distances indicate the front is more advanced in the CFL than in the validation dataset. Grey lines mark the ±250 m range.

4.4.1.4 Jakobshavn Isbræ, southern sector, 2009

The calving front in 2008 of Jakobshavn Isbræ was processed as two separate sectors with different flow directions. The southern sector in the CFL product shows a large localized discrepancy with the validation dataset when measurement is conducted parallel to the direction of glacier flow, with a significantly smaller difference when measuring to the nearest point of the validation dataset.

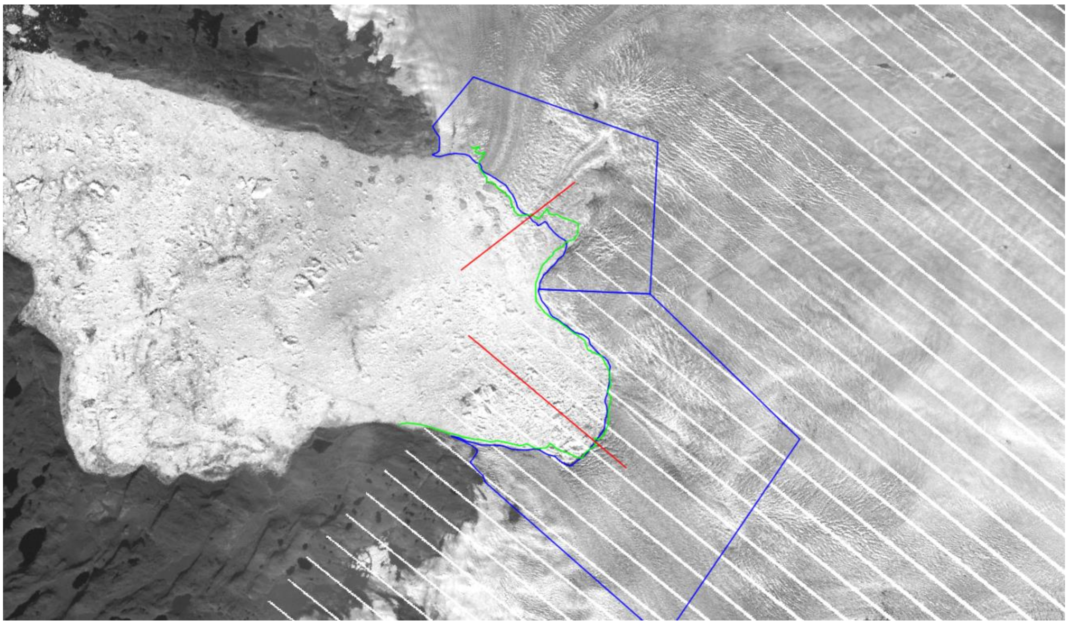

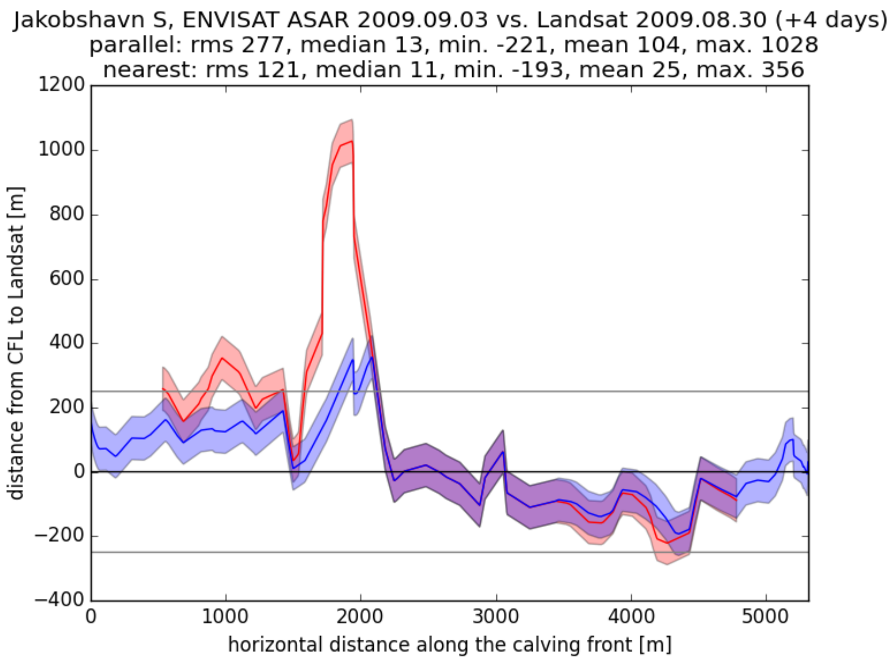

Fig. 4.4.1.4 – Jakobshavn, southern sector, 2009. Top: CFL (green line) based on ENVISAT ASAR, validation data based on Landsat ETM+ (blue line) and flow direction (red), plotted on the Landsat panchromatic band. Bottom: distances measured parallel to glacier flow are plotted in red, distances from the CFL vector to the nearest validation vector are plotted in blue. Positive distances indicate the front is more advanced in the CFL than in the validation dataset. Grey lines mark the ±250 m range.

4.4.1.5 Kangerdlugssuaq, 2008

Only one suitable pair of CFL and Landsat images could be found, and it provides a good example of ice melange in direct contact with the calving front.

The large discrepancy between the datasets when distance is measured along the direction of glacier flow is due to the curvature of the calving front, showing that the 'nearest' metric is more meaningful in this case.

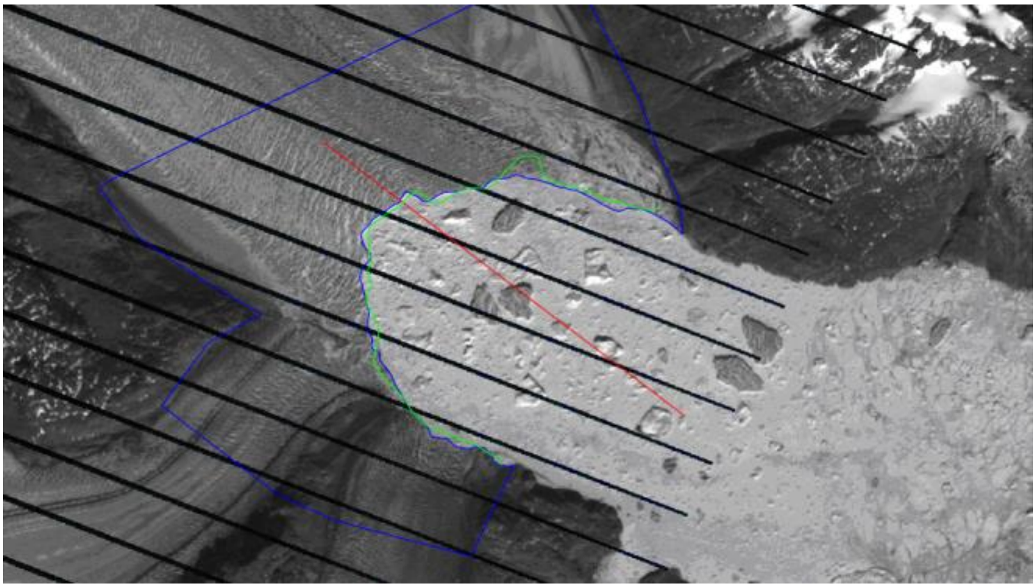

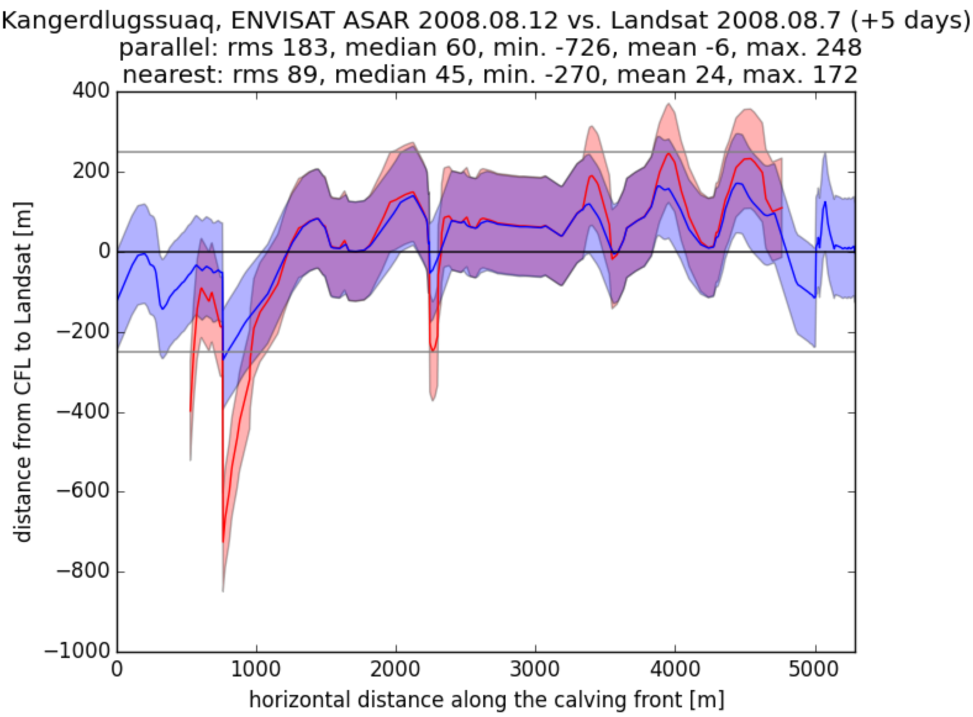

Fig. 4.4.1.5 –Kangerdlugssuaq, 2008. Top: CFL (green line) based on ENVISAT ASAR, validation data based on Landsat ETM+ (blue line) and flow direction (red), plotted on the Landsat panchromatic band. Bottom: distances measured parallel to glacier flow are plotted in red, distances from the CFL vector to the nearest validation vector are plotted in blue. Positive distances indicate the front is more advanced in the CFL than in the validation dataset. Grey lines mark the ±250 m range.

4.4.1.6 Upernavik B, 2004

The calving front of the Upernavik B ice stream has a dense temporal coverage of CFL products, allowing validation intercomparisons in three different years. In all years there the calving front in the CFL products appears more advanced than in the Landsat validation dataset.

Even though the 2004 CFL product is based on SAR data acquired 3 days later than the Landsat image used for validation (the largest lag in the Upernavik pairs), it shows the largest positive difference.

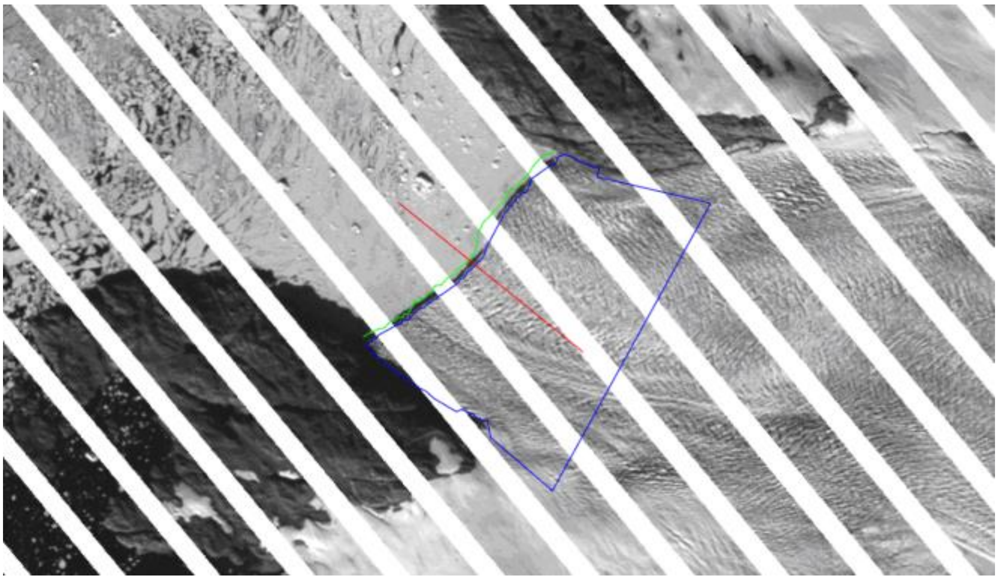

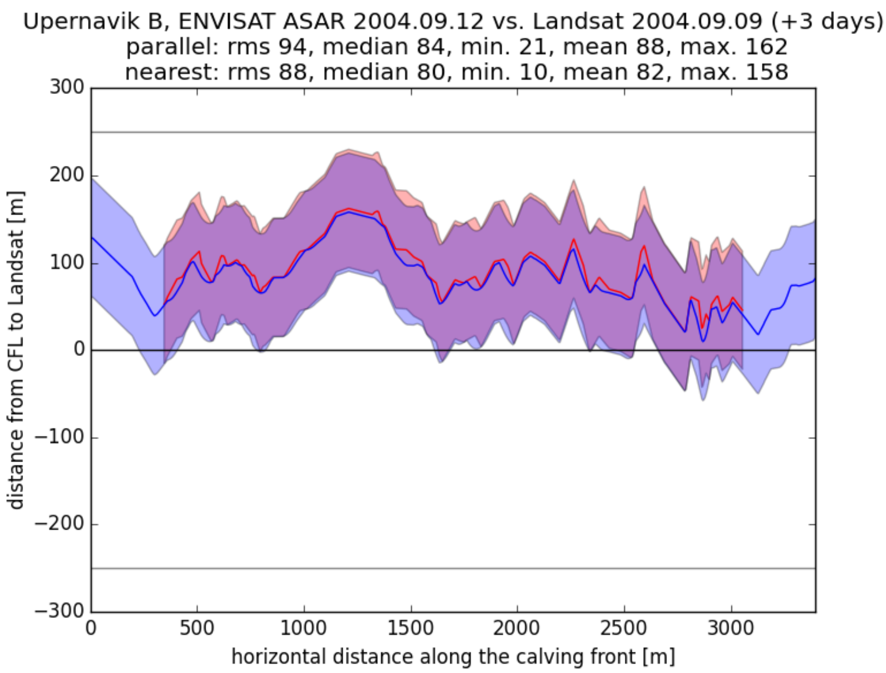

Fig. 4.4.1.6 –Upernavik B, 2004. Top: CFL (green line) based on ENVISAT ASAR, validation data based on Landsat ETM+ (blue line) and flow direction (red), plotted on the Landsat panchromatic band. Bottom: distances measured parallel to glacier flow are plotted in red, distances from the CFL vector to the nearest validation vector are plotted in blue. Positive distances indicate the front is more advanced in the CFL than in the validation dataset. Grey lines mark the ±250 m range.

4.4.1.7 Upernavik B, 2006

The 2006 CFL product is based on SAR data acquired on the same day as the Landsat image used for validation. While the shape of the terminus is captured accurately and the distance between CFL and validation is smaller than in the 2004 pair, there is a clear bias toward more advanced terminus in the CFL compared with Landsat.

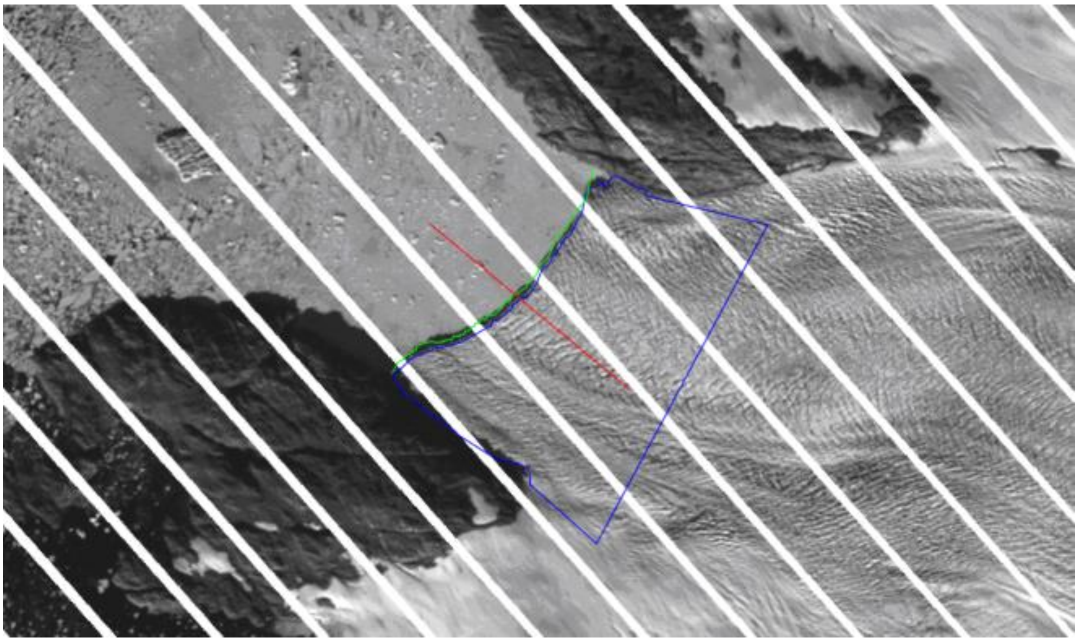

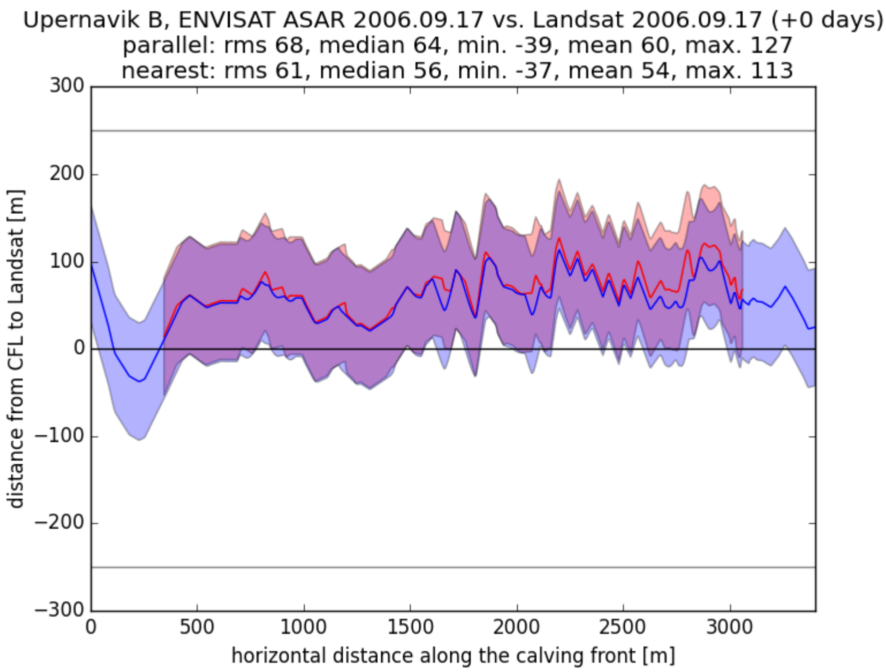

Fig. 4.4.1.7 –Upernavik B, 2006. Top: CFL (green line) based on ENVISAT ASAR, validation data based on Landsat ETM+ (blue line) and flow direction (red), plotted on the Landsat panchromatic band. Bottom: distances measured parallel to glacier flow are plotted in red, distances from the CFL vector to the nearest validation vector are plotted in blue. Positive distances indicate the front is more advanced in the CFL than in the validation dataset. Grey lines mark the ±250 m range.

4.4.1.8 Upernavik B, 2009

The 2009 Upernavik B CFL product again captures the shape of the terminus accurately, and this example has the smallest error observed of all validation pairs analysed. In 2009, SAR was acquired two days before Landsat at a time of the year when the terminus is probably still retreating, which could justify a more advanced CFL terminus. However, the same was observed for 2006 and 2004, when Landsat was acquired on the same day or even a few days earlier than SAR.

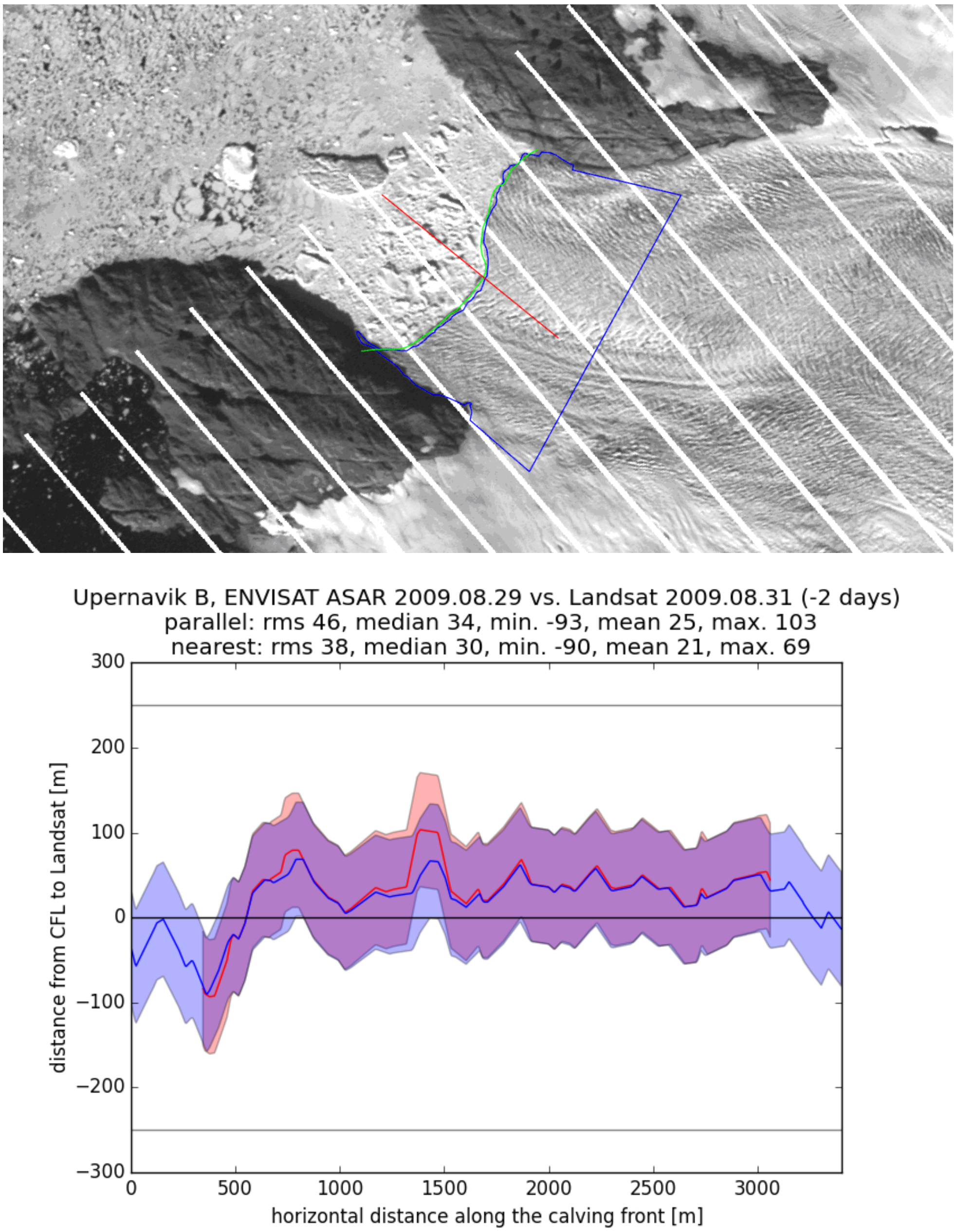

Fig. 4.4.1.8 –Upernavik B, 2009. Top: CFL (green line) based on ENVISAT ASAR, validation data based on Landsat ETM+ (blue line) and flow direction (red), plotted on the Landsat panchromatic band. Bottom: distances measured parallel to glacier flow are plotted in red, distances from the CFL vector to the nearest validation vector are plotted in blue. Positive distances indicate the front is more advanced in the CFL than in the validation dataset. Grey lines mark the ±250 m range.

4.4.1.9 Kangia Nunaata Sermia, 1993

Kangia Nunaata Sermia provides the only Landsat 5 TM image suitable for comparison with CFL products derived from ERS1 SAR data. It also provides by far the largest error within this validation subset of the CFL products, due to features of sea ice in the fjord having been interpreted as the calving front which was in reality more than 5 km away.

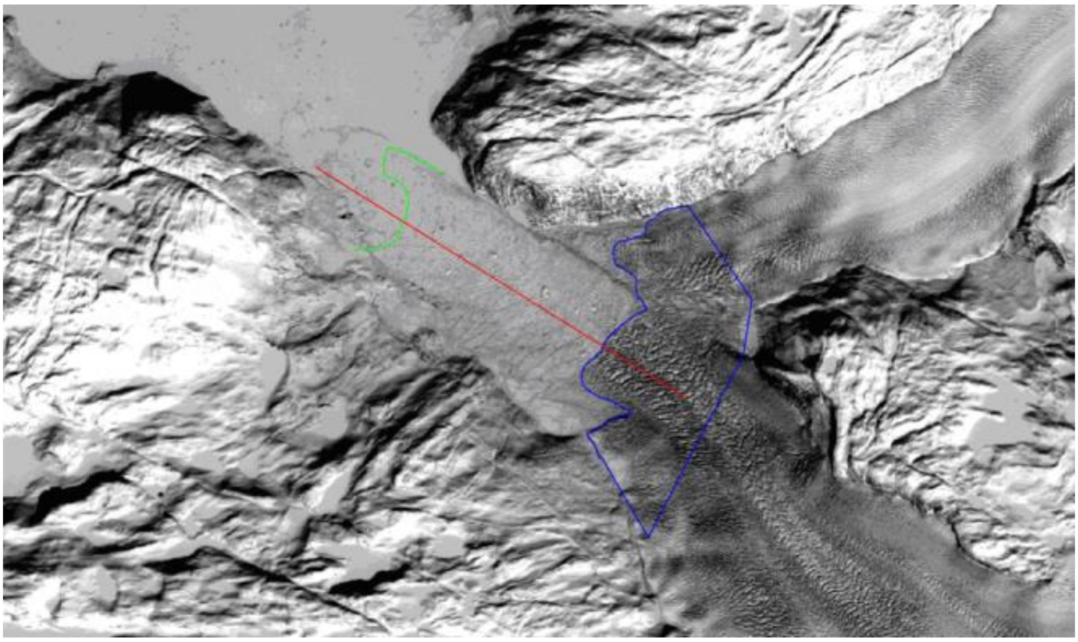

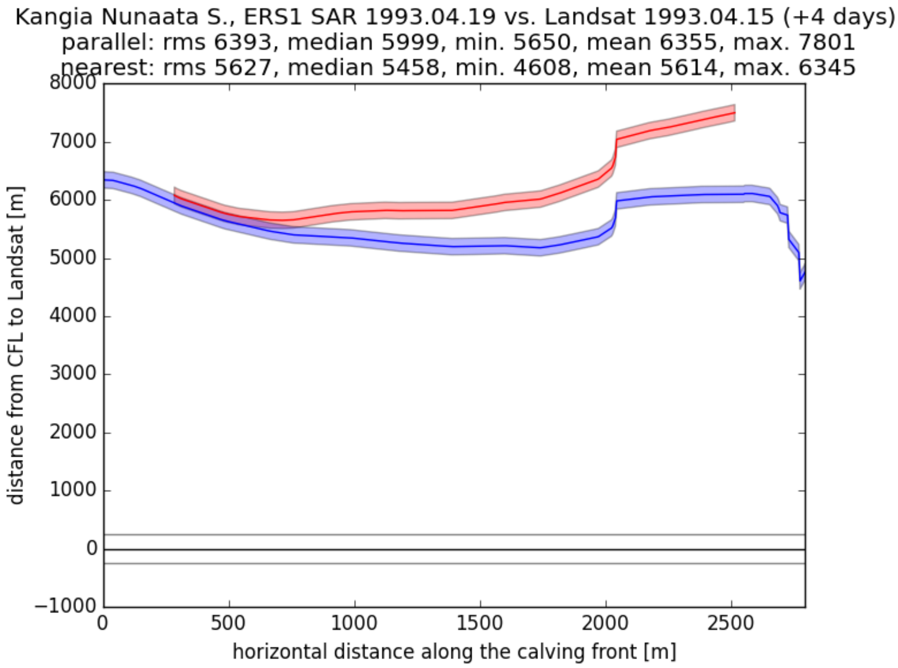

Fig. 4.4.1.9 –Kangia Nunaata Sermia, 1993. Top: CFL (green line) based on ERS1 SAR, validation data based on Landsat TM (blue line) and flow direction (red), plotted on Landsat band 3. Bottom: distances measured parallel to glacier flow are plotted in red, distances from the CFL vector to the nearest validation vector are plotted in blue. Positive distances indicate the front is more advanced in the CFL than in the validation dataset. Grey lines mark the ±250 m range.

4.4.1.10 Kangigdleq, northern terminus, 2010

Kangigdleq has two termini in contact with the fjord which have been validated separately. The dense CFL temporal coverage allows comparison with Landsat in 2010, 2008 and 2006.

The errors observed at this glacier are difficult to interpret: the northern terminus is consistently too advanced by hundreds of meters while the southern terminus is consistently behind the Landsat position.

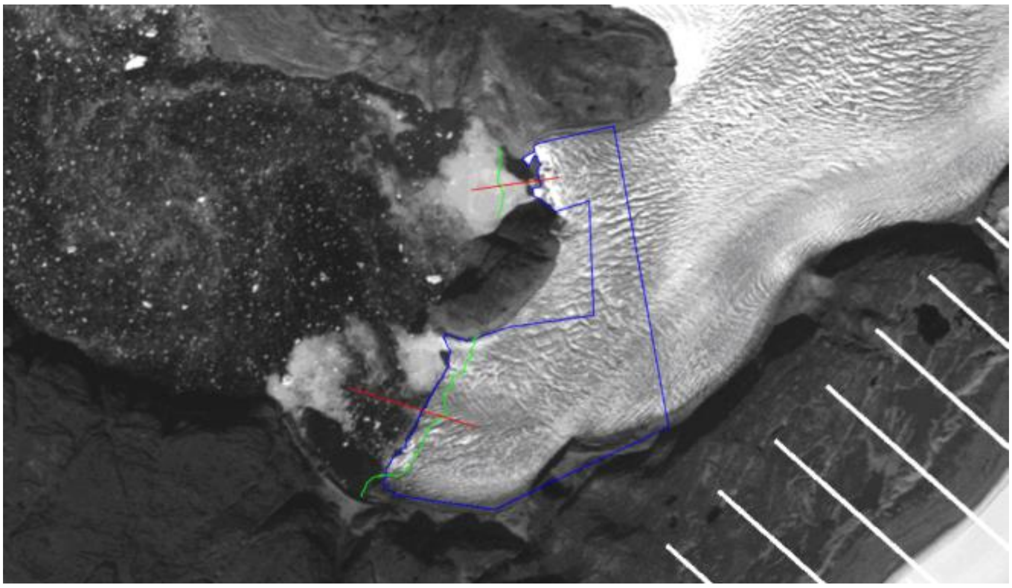

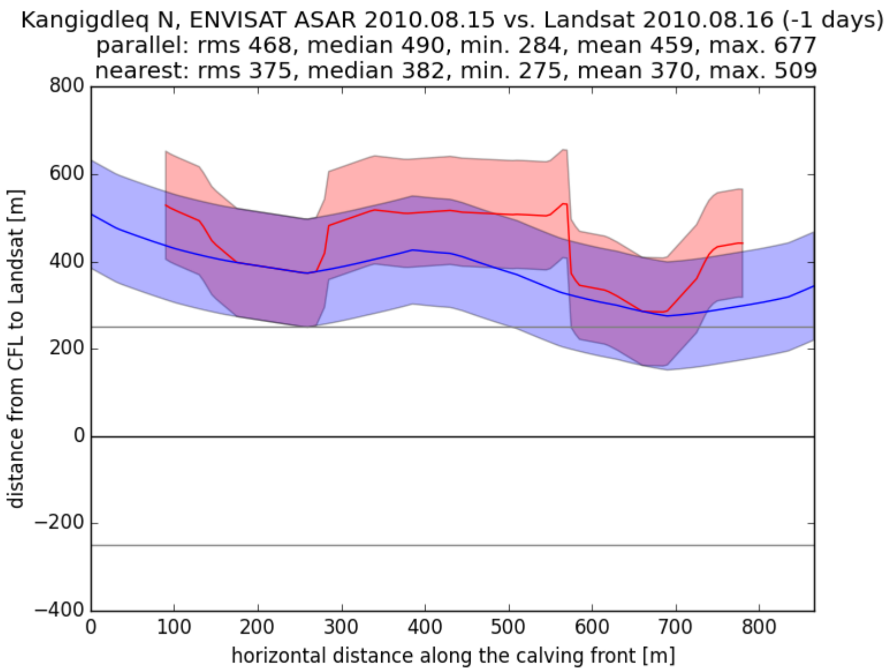

Fig. 4.4.1.10 –Kangigdleq, northern terminus, 2010. Top: CFL (green line) based on ENVISAT ASAR, validation data based on Landsat ETM+ (blue line) and flow direction (red), plotted on the Landsat panchromatic band. Bottom: distances measured parallel to glacier flow are plotted in red, distances from the CFL vector to the nearest validation vector are plotted in blue. Positive distances indicate the front is more advanced in the CFL than in the validation dataset. Grey lines mark the ±250 m range.

4.4.1.11 Kangigdleq, southern terminus, 2010

Kangigdleq has two termini in contact with the fjord which have been validated separately. The dense CFL temporal coverage allows comparison with Landsat in 2010, 2008 and 2006.

The errors observed at this glacier are difficult to interpret: the northern terminus is consistently too advanced by hundreds of meters while the southern terminus is consistently behind the Landsat position.

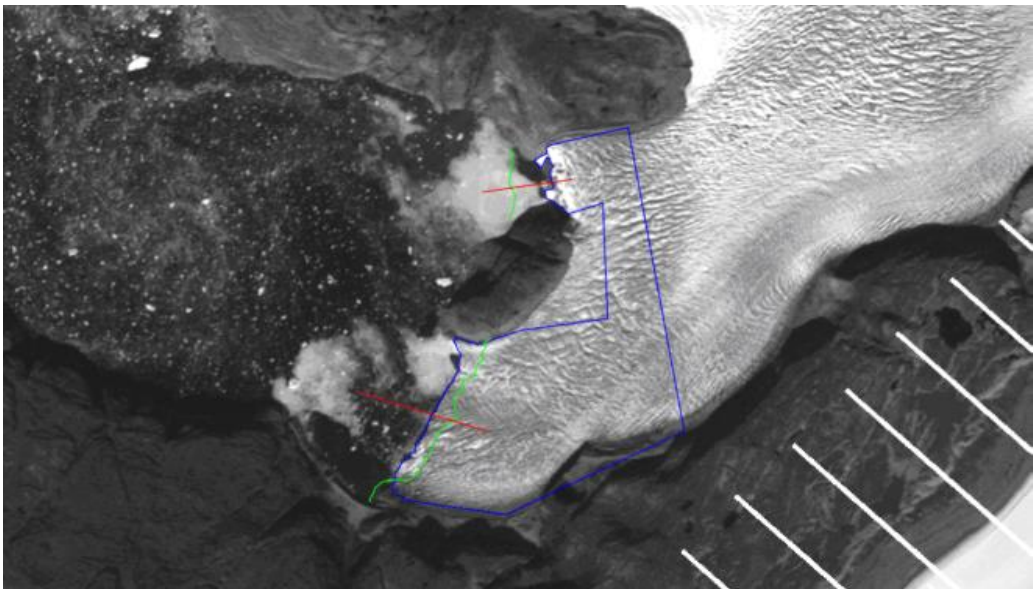

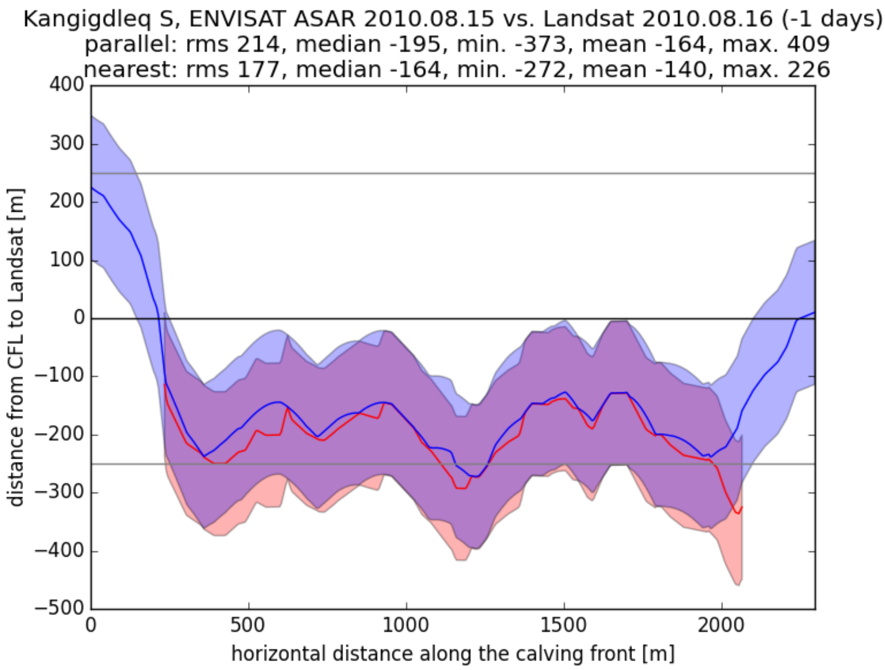

Fig. 4.4.1.11 –Kangigdleq, southern terminus, 2010. Top: CFL (green line) based on ENVISAT ASAR, validation data based on Landsat ETM+ (blue line) and flow direction (red), plotted on the Landsat panchromatic band. Bottom: distances measured parallel to glacier flow are plotted in red, distances from the CFL vector to the nearest validation vector are plotted in blue. Positive distances indicate the front is more advanced in the CFL than in the validation dataset. Grey lines mark the ±250 m range.

4.4.1.12 Kangigdleq, northern terminus, 2008

Kangigleq has two termini in contact with the fjord which have been validated separately. The dense CFL temporal coverage allows comparison with Landsat in 2010, 2008 and 2006.

The errors observed at this glacier are difficult to interpret: the northern terminus is consistently too advanced by hundreds of meters while the southern terminus is consistently behind the Landsat position.

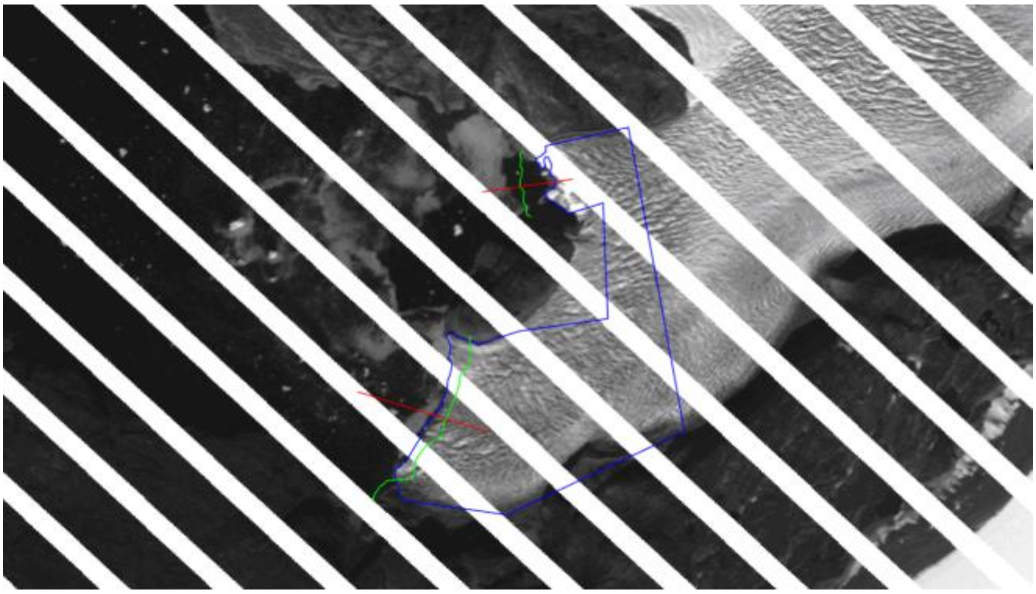

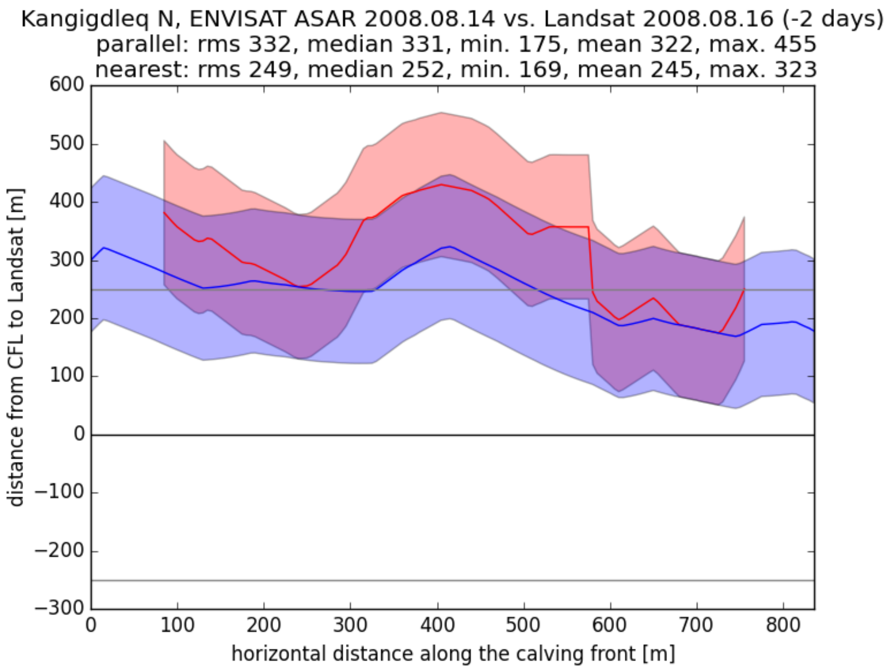

Fig. 4.4.1.12 –Kangigdleq, northern terminus, 2008. Top: CFL (green line) based on ENVISAT ASAR, validation data based on Landsat ETM+ (blue line) and flow direction (red), plotted on the Landsat panchromatic band. Bottom: distances measured parallel to glacier flow are plotted in red, distances from the CFL vector to the nearest validation vector are plotted in blue. Positive distances indicate the front is more advanced in the CFL than in the validation dataset. Grey lines mark the ±250 m range.

4.4.1.13 Kangigdleq, southern terminus, 2008

Kangigleq has two termini in contact with the fjord which have been validated separately. The dense CFL temporal coverage allows comparison with Landsat in 2010, 2008 and 2006.

The errors observed at this glacier are difficult to interpret: the northern terminus is consistently too advanced by hundreds of meters while the southern terminus is consistently behind the Landsat position.

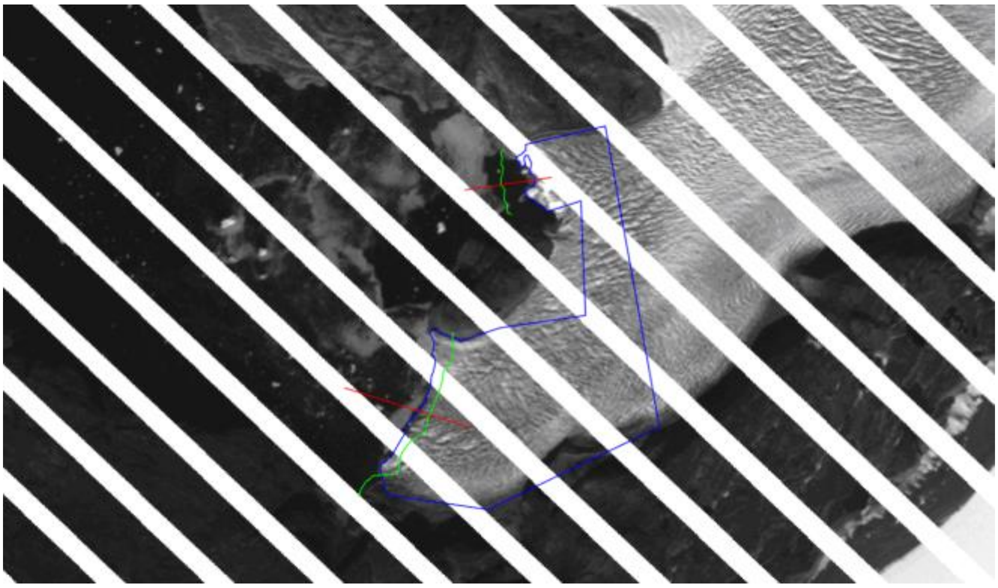

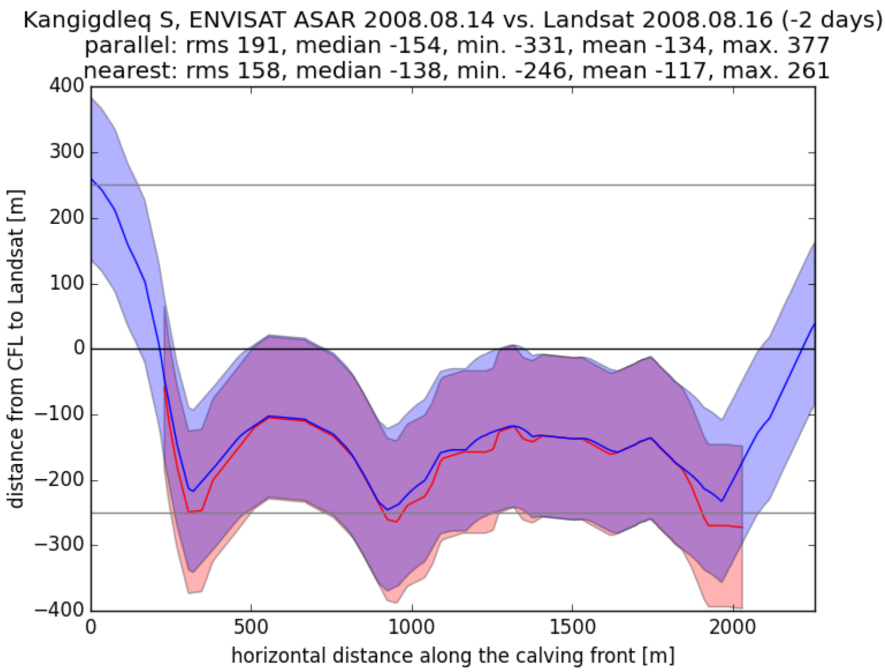

Fig. 4.4.1.13 –Kangigdleq, southern terminus, 2008. Top: CFL (green line) based on ENVISAT ASAR, validation data based on Landsat ETM+ (blue line) and flow direction (red), plotted on the Landsat panchromatic band. Bottom: distances measured parallel to glacier flow are plotted in red, distances from the CFL vector to the nearest validation vector are plotted in blue. Positive distances indicate the front is more advanced in the CFL than in the validation dataset. Grey lines mark the ±250 m range.

4.4.1.14 Kangigdleq, northern terminus, 2006

Kangigleq has two termini in contact with the fjord which have been validated separately. The dense CFL temporal coverage allows comparison with Landsat in 2010, 2008 and 2006.

The errors observed at this glacier are difficult to interpret: the northern terminus is consistently too advanced by hundreds of meters while the southern terminus is consistently behind the Landsat position.

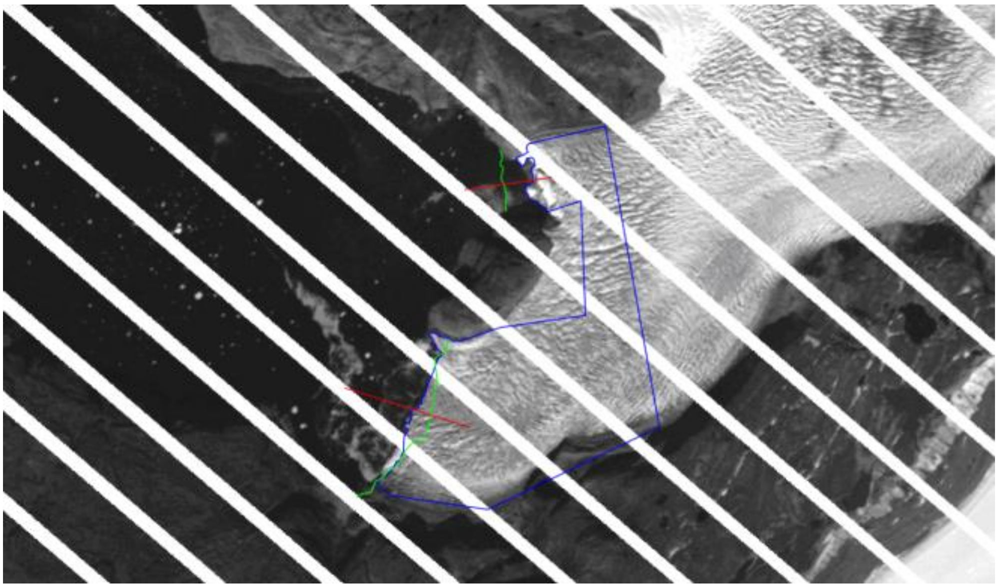

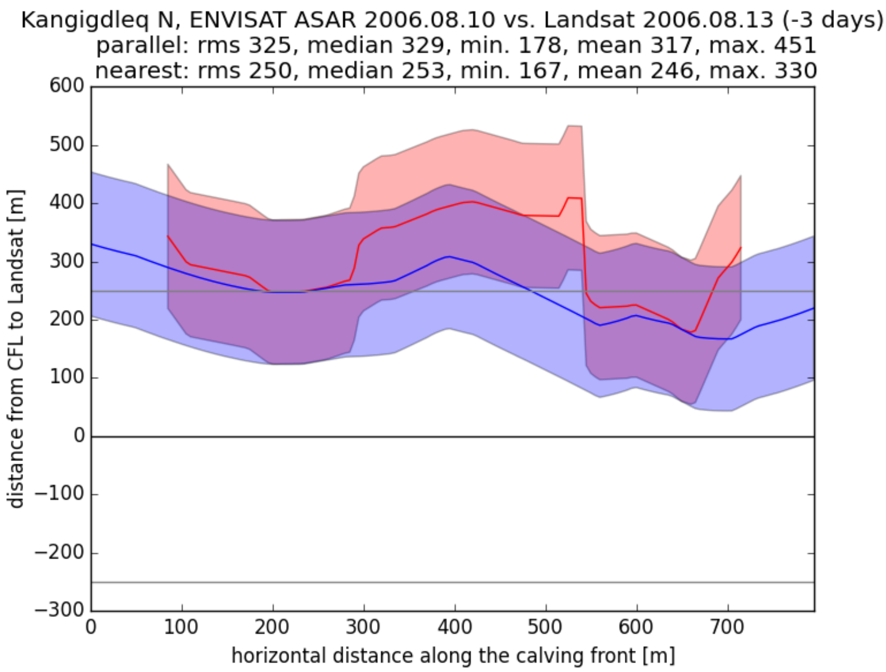

Fig. 4.4.1.14 –Kangigdleq, northern terminus, 2006. Top: CFL (green line) based on ENVISAT ASAR, validation data based on Landsat ETM+ (blue line) and flow direction (red), plotted on the Landsat panchromatic band. Bottom: distances measured parallel to glacier flow are plotted in red, distances from the CFL vector to the nearest validation vector are plotted in blue. Positive distances indicate the front is more advanced in the CFL than in the validation dataset. Grey lines mark the ±250 m range.

4.4.1.15 Kangigdleq, southern terminus, 2006

Kangigleq has two termini in contact with the fjord which have been validated separately. The dense CFL temporal coverage allows comparison with Landsat in 2010, 2008 and 2006.

The errors observed at this glacier are difficult to interpret: the northern terminus is consistently too advanced by hundreds of meters while the southern terminus is consistently behind the Landsat position.

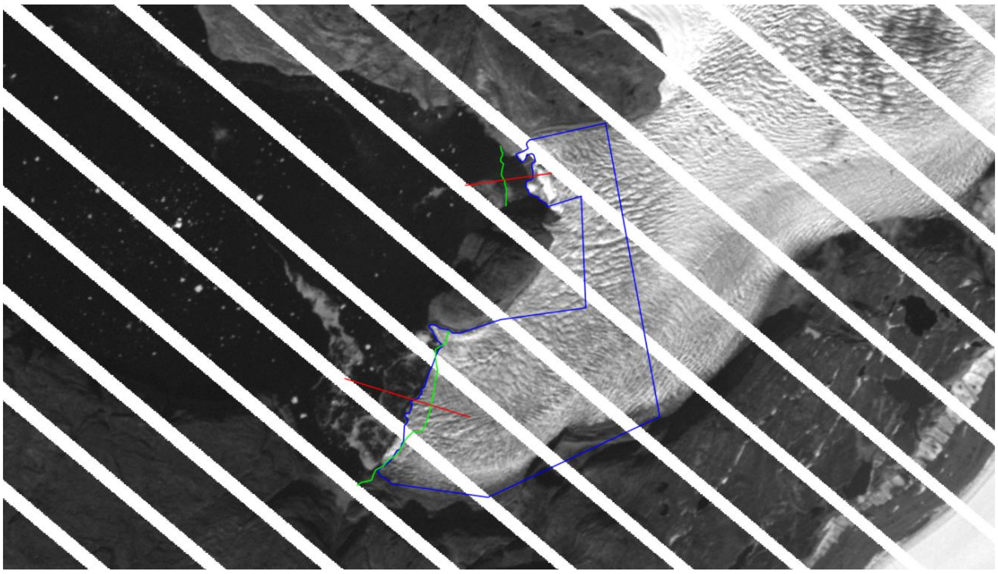

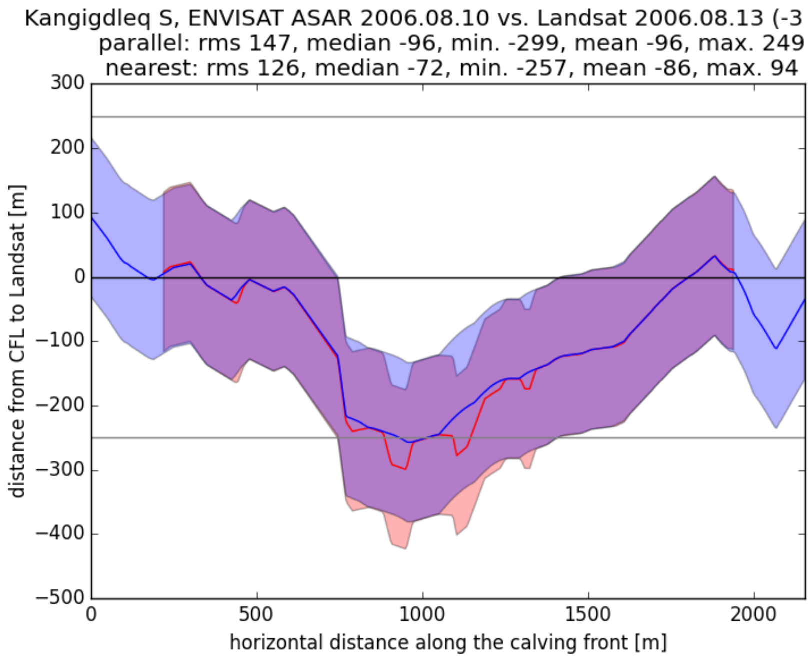

Fig. 4.4.1.15 –Kangigdleq, southern terminus, 2006. Top: CFL (green line) based on ENVISAT ASAR, validation data based on Landsat ETM+ (blue line) and flow direction (red), plotted on the Landsat panchromatic band. Bottom: distances measured parallel to glacier flow are plotted in red, distances from the CFL vector to the nearest validation vector are plotted in blue. Positive distances indicate the front is more advanced in the CFL than in the validation dataset. Grey lines mark the ±250 m range.

4.4.1.16 Sermeq Avannarleq, 2006

SermeqAvannarleq in 2006 provides a same-day pair of CFL and Landsat validation data. The shape of the terminus is accurately captured by the CFL product.

An offset is clearly visible and it may result from different layover and shadow characteristics that can affect the appearance of the calving cliff in the SAR image

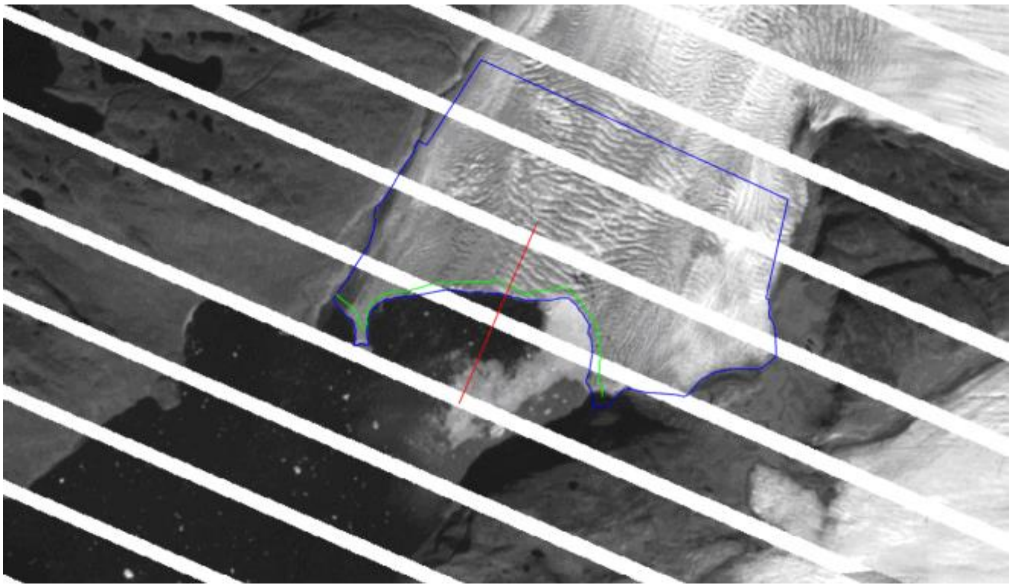

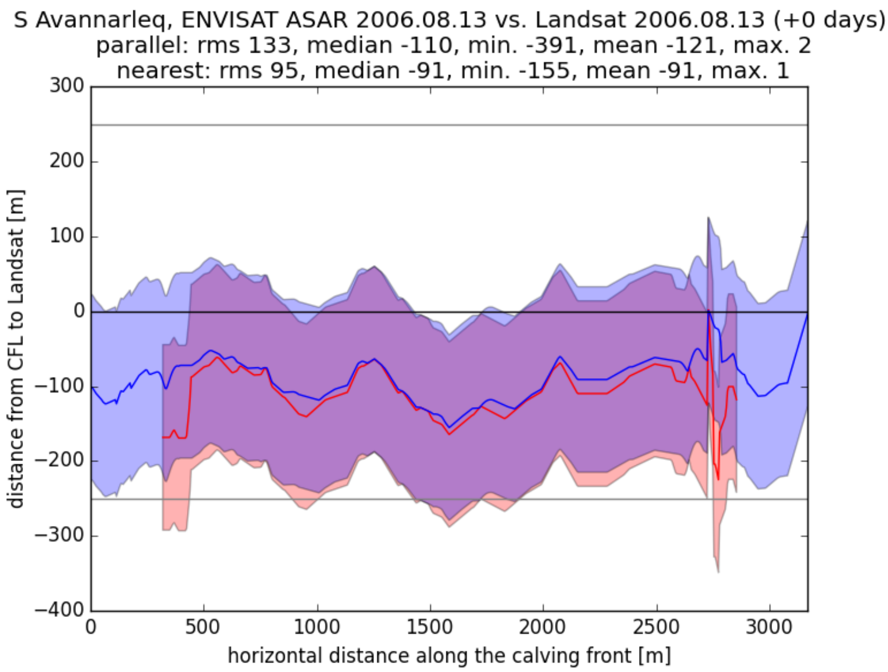

Fig. 4.4.1.16 –Sermeq Avannarleq, 2006. Top: CFL (green line) based on ENVISAT ASAR, validation data based on Landsat ETM+ (blue line) and flow direction (red), plotted on the Landsat panchromatic band. Bottom: distances measured parallel to glacier flow are plotted in red, distances from the CFL vector to the nearest validation vector are plotted in blue. Positive distances indicate the front is more advanced in the CFL than in the validation dataset. Grey lines mark the ±250 m range.

4.5 Recommendations for product improvement

The current CFL products based on ENVISAT ASAR data generally meets the specified accuracy of 250 m, including under difficult conditions like presence of ice melange at the front of the glacier. Within the specified accuracy, biases seem site-dependent. It is therefore recommended to investigate and characterize biases arising from different layover and shadow characteristics at each glacier, because they seem to introduce small but systematic biases.

It is also recommended to focus future work on recent sensors with resolution and quality comparable to ENVISAT ASAR, because large errors have been observed in a CFL product derived from ESR1 SAR. There are however too few validation pairs to conclusively rule out the possibility of producing reliable CFL products from older sensors. If this is attempted, it is recommended to focus initially on years with good coverage of optical imagery suitable for calibration.

In order to make the CFL easier to use, it is recommended to consistently digitize them all the way to the fjord sides. In case the interpretation of the image is uncertain at those locations, it may be useful to introduce a 'reliability' field in the shapefile table and label dubious segments as such.

Finally, while most of the validation effort dealt with the mapping accuracy of the CFL location, metadata was also inspected and it is recommended to be more consistent in the classification of the material in contact with the terminus. In particular, ice melange (IM in the 'pro_mat' field) was classified as sea ice ('SI').

5 Grounding Line Location (GLL)

This chapter gives a complete report of the activities carried out to assess the quality of the GLL products.

5.1 Sources of independent validation data

The grounding line location of an outlet glacier with a floating tongue is not immediately observable. Therefore, validation of grounding line/grounding zone location is challenging due to the lack of available observations and methodology.

A qualitative comparison with two studies of North Greenland grounding line locations can be carried out. Grounding line locations of North Greenland glaciers "Petermann Glacier" and "79 Fjord Glacier" (see map in Figure 5.1) are described in the literature in Reeh et al., 2001 and Rignot et al., 1997, respectively.

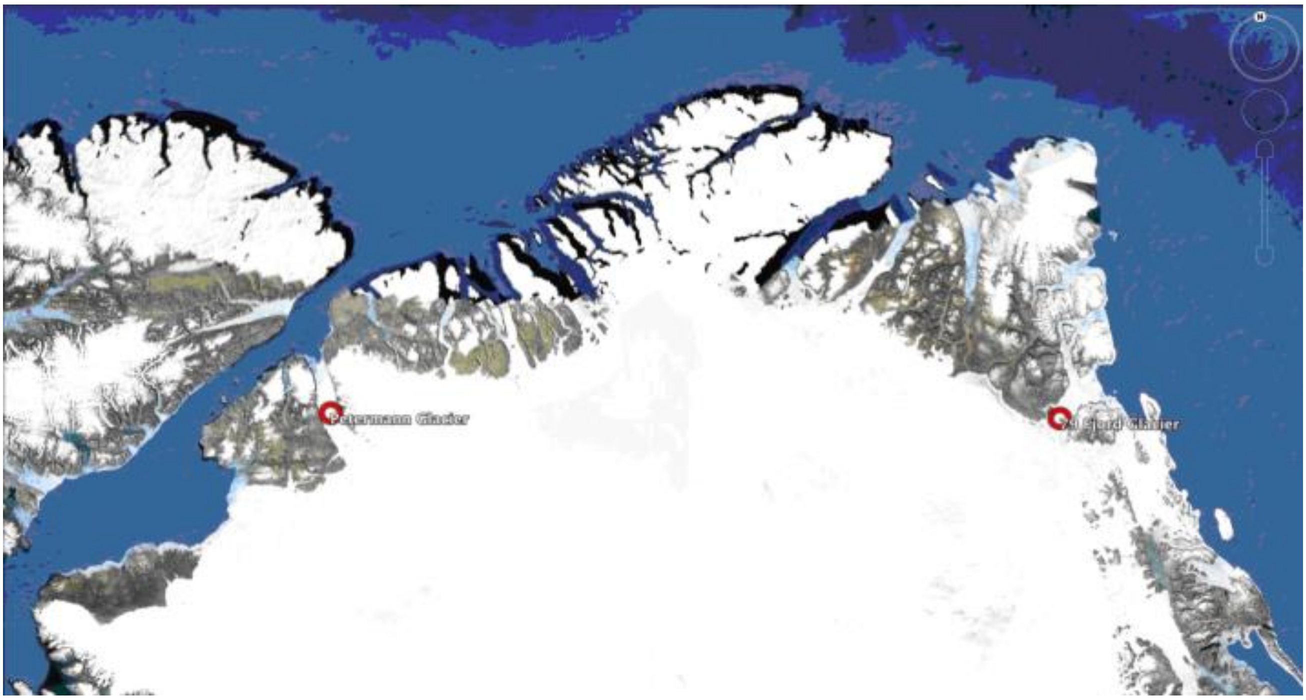

Figure 5-1: Location of Petermann Glacier and 79 Fjord Glacier. Image: Google Earth

5.1.1 In-situ observational data

None available.

5.1.2 Alternative products

A theoretical grounding line location of a floating ice shelf can be modelled using a tidal flexure model in which the glacier is assumed fixed to the bed at one end, and floating freely only affected by vertical tidal buoyancy forces at the other end. While the tide can be modelled fairly well, this exercise requires exact knowledge of ice shelf thickness, lateral drag and the internal strength properties of the ice body. These parameters are not well known for the North Greenland glaciers.

5.2 Selection of independent validation data

5.2.1 Validation data selection criteria

None available.

5.2.2 Validation data errors and biases

None available.

5.2.3 Validation data uncertainty

None available.

5.3 Validation procedure

In order to perform a qualitative comparison of the ESA GLL product to the literature, we carry out the following steps:

5.3.1 Register images/figures from the literature

From the relevant publications, we retrieve a digital copy of the figure on which the grounding line is indicated.). The GIS software package "QGis" was used for this task. Ground Control Points were acquired from terrain features identified in georeferenced Landsat images presented with the Google Earth application.

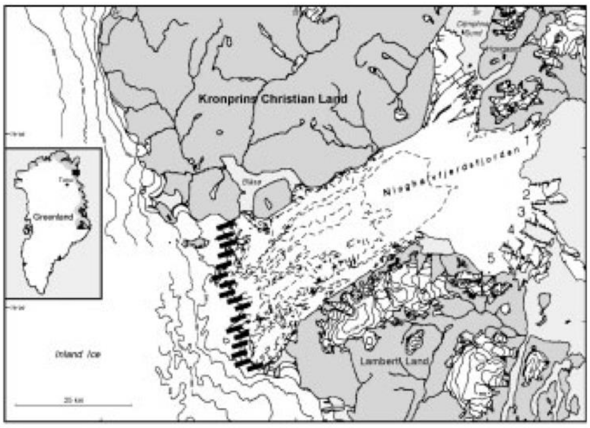

Figure 5-2: Original figure from Reeh et al., 2001 (Figure 1). Grounding zone is indicated with black bars.

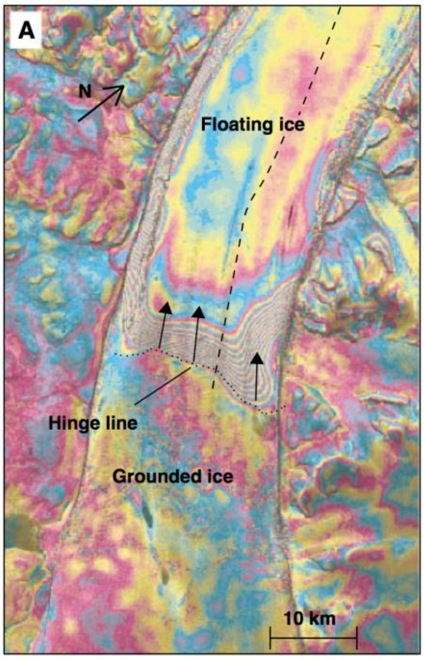

Figure 5-3: Original figure from Rignot et al., 1997 (Figure 2A). Grounding line is indicated with a dashed line.

5.3.2 Digitize grounding line and insert ESA GLL product

Using QGis, the grounding line was traced by hand, following the indication in the georeferenced figure, see Figure 5-4 and Figure 5-5 for results. The ESA GLL product grounding lines for the two relevant glaciers were added to the same project for comparison.

5.3.3 79 Fjord Glacier

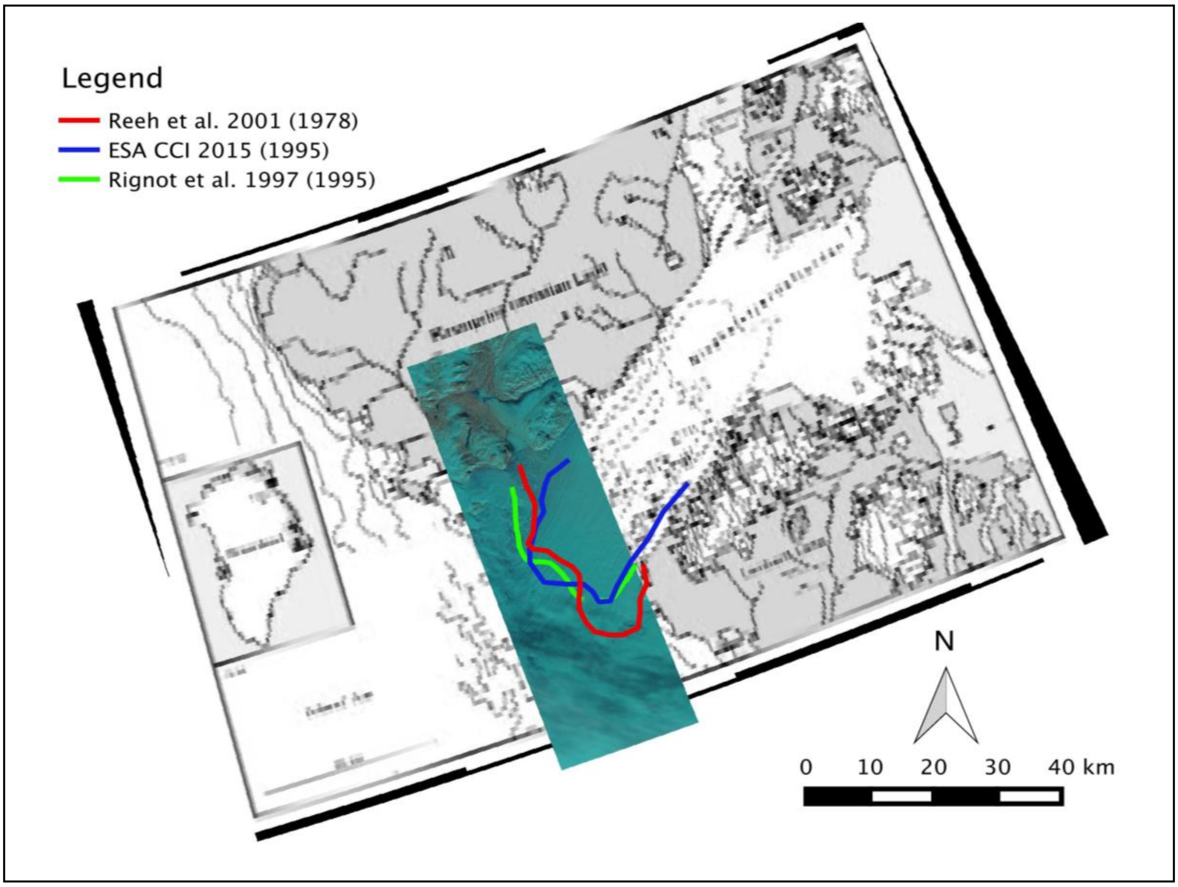

Figure 5-4: Location of 1978, 1995 and 1995 grounding lines, respectively, from three different sources: Reeh et al., 2001; Rignot et al., 1997, and ESA CCI 2015. Background monochrome image is a georeferenced version of Figure 1 from Reeh et al., 2001, serving as the basis for digitalization of the 1978 grounding line (red). Rignot 1995 grounding line is digitized from Rignot et al., 1997 (image not shown). Green image area of grounding zone is a Landsat 8 image recorded on April 27 2013. Arrow indicates polar stereographic grid north.

5.4 Petermann Glacier

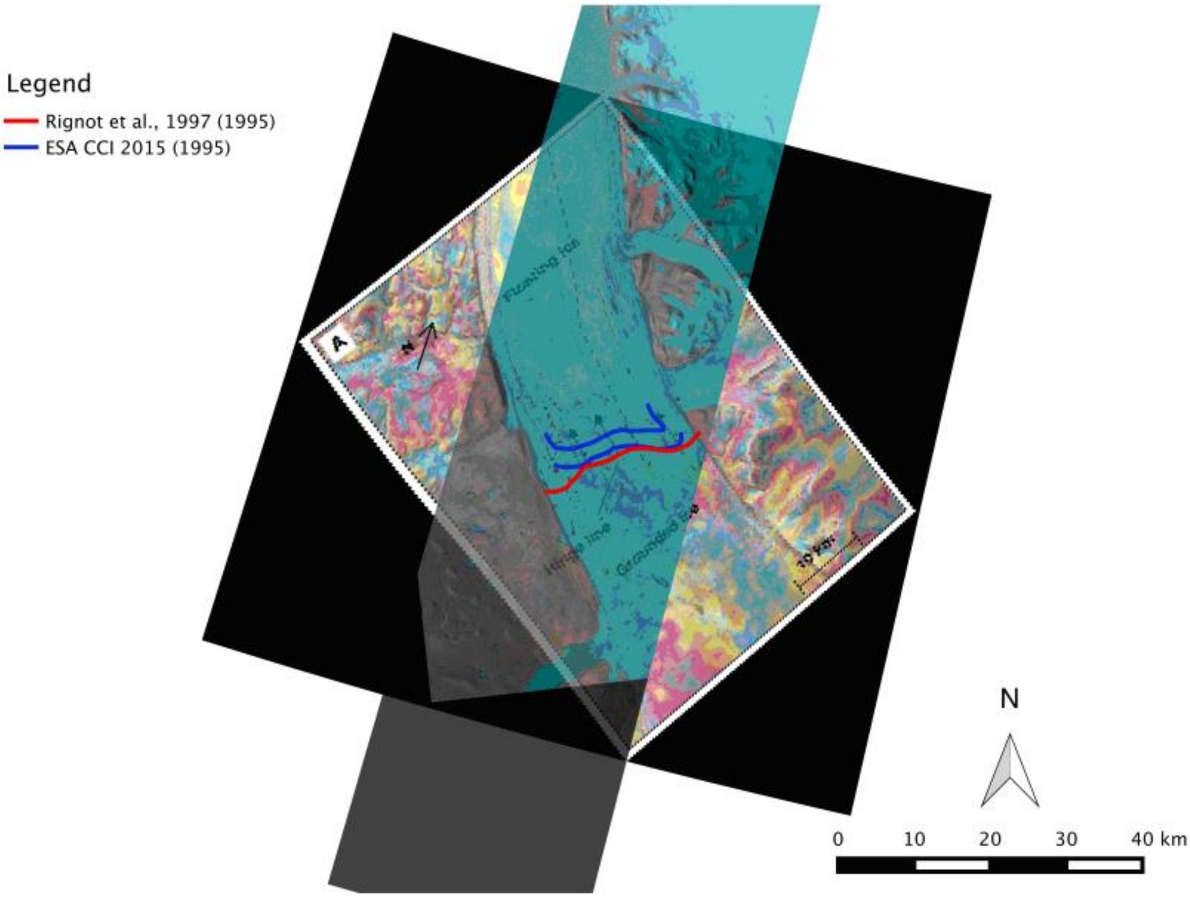

Figure 5-5: Location of 1995 grounding lines from two different sources: Rignot et al., 1997, and ESA CCI 2015. Background interferometry image is a georeferenced version of Figure 2 A from Rignot et al., 1997, serving as the basis for digitalization of the 1995 grounding line (red). Transparent green image area of grounding zone is a Landsat 8 image recorded on July 6 2014. Arrow indicates polar stereographic grid north.

5.5 Validation procedure outcome

Figure 5-4 and Figure5-5 show the grounding lines digitized from the literature along with the ESA GLL product grounding lines.

On 79 Fjord Glacier (Fig. 5-4) there is good correspondence between the ESA GLL shape and the Rignot et al., 1997 line. The Reeh et al., 2001 grounding line matches well in the north-western part, but then diverges further south than the ESA GLL line and the Rignot et al., 1997 line. The maximum deviation is ~6.4 km.

On Petermann Glacier (Figure 5-5), correspondence is better than at 79 Fjord Glacier, with maximum deviation ~1 km between the Rignot et al., 1997, and the zone delineated by the two ESA GLL lines.

One minor caveat to consider in this qualitative comparison is the acquisition time of the lines. The Reeh et al. 2001 line on 79 Fjord Glacier is based on 1978 aero-photos, whereas the Rignot et al., 1997 lines are based on inSAR scenes acquired in 1995. Since the Reeh et al., 2001 line on 79 Fjord Glacier is positioned further back than the 1995 lines, this suggests a grounding line advance in the years 1978-1995. This contradicts the expectation of grounding line retreat as a consequence of climate change. The 1995 lines from Rignot et al., 1997 are consistent with the ESA GLL 1995 line at both 79 Fjord Glacier and Petermann Glacier.

5.6 Recommendations for product improvement

In Greenland only a very few large outlet glaciers are still floating, e.g. Petermann glacier. Most of the outlet glaciers were already retreated beyond the grounding line.

To apply InSAR, the most suitable method for mapping GLL, coherence of SAR images is needed. Repeat cycles of current SAR satellites available for Ice Sheet CCI are too long (Sentinel-1A: 12 days; RSAT-2: 24 days; TSX/TDX: 11days) and coherence over major outlet glaciers is in general lost due to variable surface conditions and/or too high ice motion. The Sentinel-1A and 1B constellation with 6 days repeat in combination with an improved GLL processing technique, which takes ice velocity from offset tracking in the interferometric processing into account, will open a new option for GLL mapping.

6 Gravimetric Mass Balance (GMB)

This chapter gives a summary of the activities carried out to assess the quality of the GMB products.

There has been no direct validation of the GMB products have been carried out simply because no independent data set for this exists. Instead some inter-comparisons have been carried out to assess the variability of these products arising from the use of different methods and data sets.

Previously, several inter-comparison exercises have been carried out. The results of these together with further investigations made on the specific CCi products are presented here.

6.1 (Inter-) comparison procedure

There are several (inter-)comparison strategies to follow. We focus on the mass change time series (and the trend in this) product and describe the following:

1. Comparison to other methods for regional and ice sheet mass balance. These are the Input-output method (or mass budget method) and volume change method.

2. Inter-comparison of the results from different methods for deriving mass changes from the same GRACE data

3. Inter-comparison of the results from using the same method but different data sets.

6.2 (Inter-) comparison procedure outcome

1. A comparison of GRACE-derived mass changes to other methods for regional and ice sheet mass balance is a major task to undertake, and outside the scope of this document. Several of such studies have been published, and here we highlight a few. The IMBIE (international mass balance intercomparison experiment) was an ambitious project including numerous methods and data sets.

The overall mass balance for ice sheets from different methods is seen in Fig 6-1. These are the Input-output method (or mass budget method) and volume change method.

It can be seen that the gravimetry method predicts mass balance results that agree with the two other methods within the error bars. The point mass inversion method which is used for generating the GIS CCI GMB products (see PSD v.2.2) also provided to the IMBIE study.

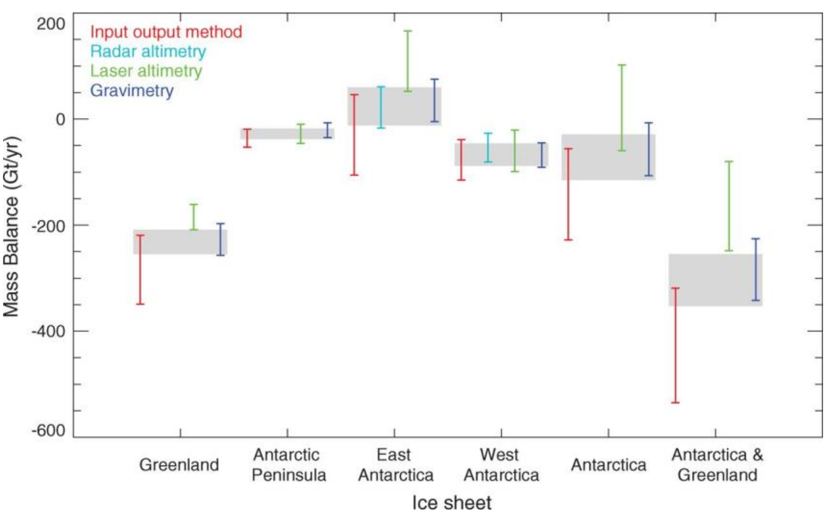

Figure 6-1: Mass balance of the ice sheets from different methods. From Shepherd et al., 2012

2. A detailed inter-comparison of the results from different methods for deriving mass changes applied on the same GRACE data was undertaken in the CCI GMB RR. The procedure and the results are described in detail in the ATBD Annex. The point mass inversion method that is used in the GIS CCI in the GMB production was included in this and showed good agreement with other submissions.

The RR participants were anonymized, but Fig. 6-2 shows the good agreement between the GIS CCI GBM product and that derived at TU Dresden (for the entire GIS). Figure 6-2 also shows two examples of the drainage basin mass change time series for basin number 1 and 6. The difference between the solutions can be the result of differences in e.g. how leakage is treated (see ATBD).

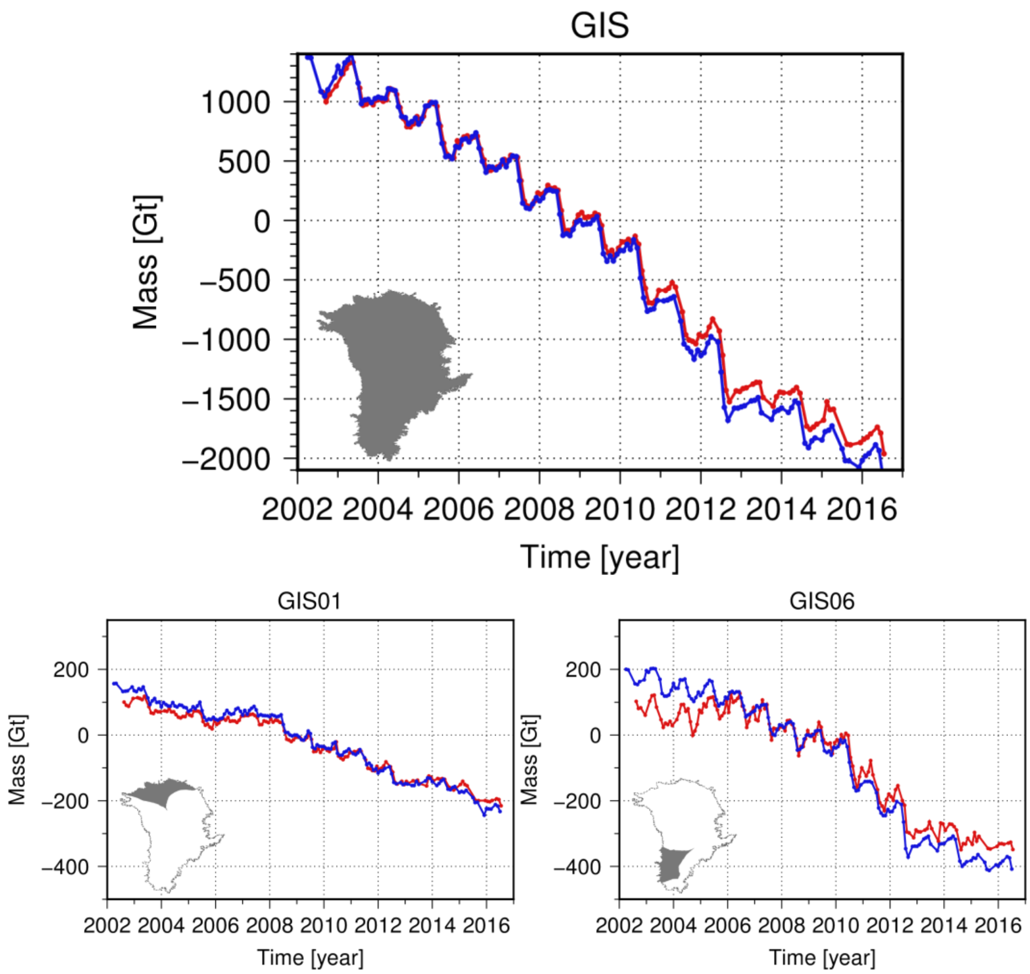

Figure 6-2 : Mass change time series of the entire GIS, basin 1 and basin 6 from the GIS CCI GMB product (blue) shown together with the one derived in TU Dresden (red).

3. The third strategy is the inter-comparison of results from using the same method but different data sets. Figure 6-3 shows the mass change time series based on two data sets: CSR05 and ITSG2016. From this comparison no significant differences are seen between the two data sets.

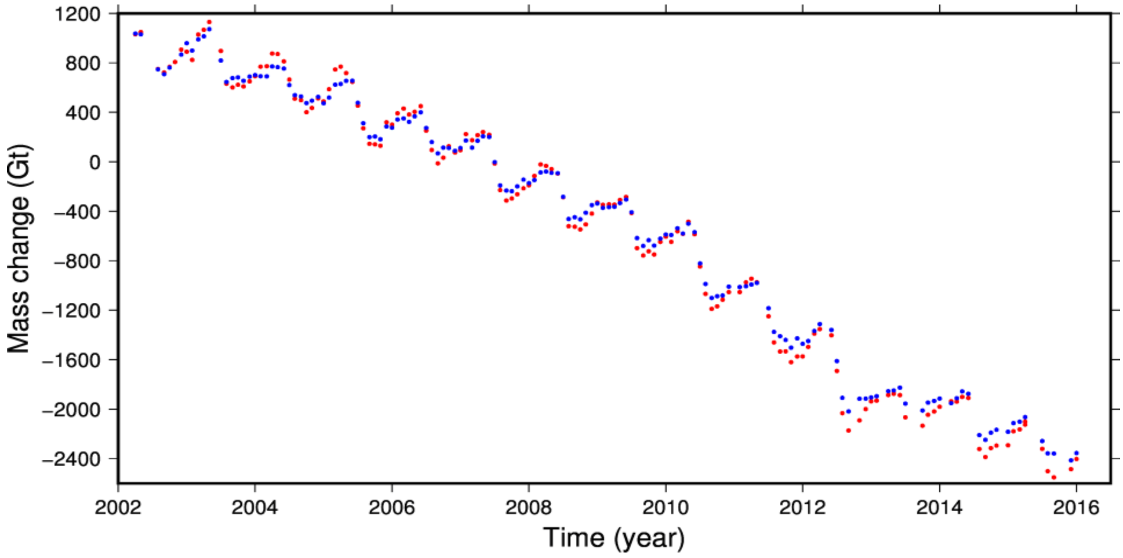

Figure 6-3: Mass change time series derived from CSR05 data (red) and ITSG2016 (blue)

6.3 Recommendations for future product improvements

Better models for GIA, degree one, and ocean model correction will lead to future improvement in the products. Studies targeted on these corrections could lead to improvements in the products.

Integrated CryoSat, GRACE and Sentinel-1 data.

One issue with the GRACE-only products is the low spatial resolution and therefore one recommendation is to produce products with increased resolution. This could be done from integrated CryoSat, GRACE and Sentinel-1 data, combined with firn compaction and snow surface density meteorological models.

The mass changes of the Greenland ice sheet are measured directly with GRACE, but only with limited spatial resolution, and relatively large errors associated with leakage from oceans, land and other ice caps. Combining CryoSat and GRACE data, supplemented with a firn density and compaction model, an integrated mass solution can be obtained with high spatial resolution. Noting that rapid temporal changes of the ice sheet is primarily driven by rapid changes in velocities of outlet glaciers, which can now be monitored at weekly resolution by Sentinel-1, the combination of all three EO data sources – GRACE, CryoSat altimetry and Sentinel-1 ice velocities – into a unified mass product, will give a new enhanced experimental ECV product, superior to the existing CCI SEC, IV and GMB products. This enhanced product will represent an operational product following the IMBIE principles, and can easily be extended to Antarctica as well at a later stage. The first concept demonstration results of such activities, for both Greenland and Antarctic, has been published in Forsberg et al. 2017.

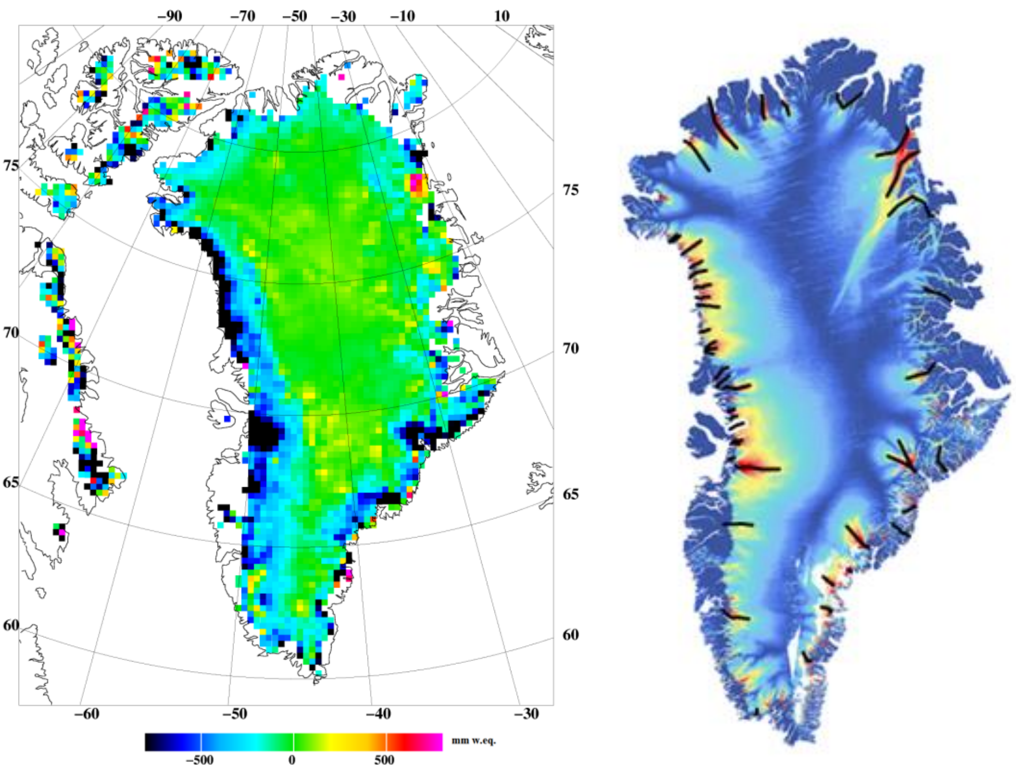

Fig. 6-4. GRACE/CryoSat mass balance grid of Greenland (left, low-resolution demonstration product) will be combined with Sentinel 1-A (and later –B) ice velocities from the Greenland ice sheet (right) in the proposed CCN/CCI+ action. Current S-1 acquisition scheme allow sub-monthly estimation of essentially all Greenland outlet glaciers.

7 References

Ahlstrøm, A.P, S.B. Andersen, C. Tijm-Reijmer, M.L. Andersen, H. Machguth, F.M. Nick, R.S.W. van de Wal, R.S. Fausto, D. van As, M. Citterio, J.P. MerrymanBoncori, 2013. Seasonal velocities of six major outlet glaciers from the Greenland ice sheet from continuous *in situ* GPS. Earth Systems Science Data, 5, 277-287

Blair, B. and Hofton, M.: IceBridge LVIS L2 Geolocated Surface Elevation Product. Boulder, Colorado USA: NASA DAAC at the National Snow and Ice Data Center. http://nsidc.org/data/docs/daac/icebridge/ilvis2/, 2012.

Den Ouden, M. A. G., Reijmer, C. H., Pohjola, V., Van de Wal, R. S. W., Oerlemans, J., and Boot, W.: Stand-alone single-frequency GPS ice velocity observations on Nordenskiöldbreen, Svalbard, The Cryosphere, 4, 593–604, doi:10.5194/tc-4-593-2010, 2010.

Brenner, A. C., Bindschadler, R. A., Thomas, R. H. and Zwally, H. J.: Slope-induced errors in radar altimetry over continental ice sheets, J. Geophys. Res. - Oceans, vol. 88, no.C3, pp. 1617–1623, 1983.

Brenner, A. C., DiMarzio, J. P., and Zwally, H. J.: Precision and Accuracy of Satellite Radar and Laser Altimeter Data Over the Continental Ice Sheets, IEEE T. Geosci. Remote., 45(2):321–331, doi: 10.1109/TGRS.2006.887172, 2007.

Forsberg, R. and Tscherning, C. C.: An overview manual for the GRAVSOFT Geodetic Gravity Field Modelling Programs. Technical Report 2, DTU Space; University of Copenhagen, August 2008.

Forsberg, R., Sørensen, L. & Simonsen, S: Greenland and Antarctica Ice Sheet Mass Changes and Effects on Global Sea Level. Surveys in Geophysics (2017) 38: 89. doi:10.1007/s10712-016-9398-7

eological Survey of Denmark and Greenland: PROMICE, Programme for Monitoring of the Greenland Ice Sheet. http://www.promice.org/home.html, 2015.

Howat, I. M., Ahn, Y., Joughin, I., van den Broeke, M. R., Lenaerts, J. T. M., and Smith, B.: Mass balance of Greenland's three largest outlet glaciers, 2000–2010, Geophys. Res. Lett., 38(12). doi: 10.1029/2011GL047565, 2011.

Krabill, W. B.: IceBridge Level-4 ATM Surface Elevation Rate of Change. Boulder, Colorado USA: NASA DAAC at the National Snow and Ice Data Center. http://nsidc.org/data/idhdt4.html, 2014.

Krabill, W. B.: IceBridge ATM L1B Elevation and Return Strength. Boulder, Colorado USA: NASA DAAC at the National Snow and Ice Data Center. http://nsidc.org/data/ilatm1b.html, 2010.

Krabill, W. B., Abdalati, W., Frederick, E., Manizade, S., Martin, C., Sonntag, J., Swift, R., Thomas, R. and J. Yungel, J.: Aircraft laser altimetry measurement of elevation changes of the Greenland Ice Sheet: technique and accuracy assessment, J. Geodyn., 34:357–376. doi: 10.1016/S0264-3707(02)00040-6, 2002.

Khvorostovsky, K.: Merging and analysis of elevation time series over Greenland ice sheet from satellite radar altimetry, IEEE Trans. Geosc. Remote Sens., 50, 1:23–36.doi: 10.1109/TGRS.2011.2160071, 2012.

Legresy, B., Papa, F., Remy, F., Vinay, G., van den Bosch, M. and Zanife, O.-Z.: ENVISAT radar altimeter measurements over continental surfaces and ice caps using the ICE-2 retracking algorithm, Remote Sens. Environ., 95(2):150–163. doi: 10.1016/j.rse.2004.11.018, 2005.

Levinsen, J. F., Khvorostovsky, K., Ticconi, F., Shepherd, A., Forsberg, R., Sørensen, L. S., Muir, A., Pie, N., Felikson, D., Flament, T., Hurkmans, R., Moholdt, G., Gunter, B., Lindenbergh, R., and Kleinherenbrink, M.: ESA ice sheet CCI: derivation of the optimal method for surface elevation change detection of the Greenland ice sheet – round robin results, Int. J. Remote Sens., 36(2):551–573. doi: 10.1080/01431161.2014.999385, 2015a.

Levinsen, J. F., Smith, B. E., Sørensen, L. S., Khvorostovky, K., Simonsen, S. B., and Forsberg, R.: A Digital elevation Model of the Greenland Ice Sheet based on Envisat and CryoSat-2 radar altimetry, Earth and Space Science, in review, 2015b.

Paul, F., N.E. Barrand, S. Baumann, E. Berthier, T. Bolch, K. Casey, H. Frey, et al. 2013: On the Accuracy of Glacier Outlines Derived from Remote-Sensing Data. Annals of Glaciology 54, no. 63: 171–82.

Reeh, N., H. H. Thomsen, A. K. Higgins, A. Weidick, 2001. Sea ice and the stability of north and northeast Greenland floating glacies. Annals of Glaciology 33, p 474-480

Rignot, E., S. P. Gogineni, W. B. Krabill, S. Ekholm, 1997. North and Northeast Greenland Ice Discharge from Satellite Radar Interferometry. Science, vol. 276., p 934-937.

Roemer, S., Legresy, B., Horwath, M., and Dietrich, R.: Refined analysis of radar altimetry data applied to the region of the subglacial Lake Vostok/Antarctica, Remote Sens. Environ., vol. 106, no. 3, pp. 269–284, 2007.

Schmidt-Jensen, T., 2014: Area changes of Greenland marine terminating glaciers. M.Sc. Thesis, Niels Bohr Institute, Copenhagen University.

Shepherd, A., Ivins, E. R., Geruo, A., Barletta, V. R., Bentley, M. J., Bettadpur, S., ... &Horwath, M. (2012). A reconciled estimate of ice-sheet mass balance. *Science*, *338*(6111), 1183-1189.

Simonsen, S. B. and Sørensen, L. S. (2017): Implications of changing scattering properties on Greenland ice sheet volume change from Cryosat-2 altimetry. Remote Sensing of Environment, 190, p. 207-216, 2017.

Skourup, H., Barletta, V., Einarsson, I., Forsberg, R., Haas, C., Helm, V., Hendricks, S., Hvidegaard, S. M., and Sørensen, L. S.: ESA CryoVEx 2011: Airborne field campaign with ASIRAS radar, EM induction sounder and laser scanner. DTU Space, National Space Institute, Technical University of Denmark, 1st edition, 2011.

Snyder, J. P. 1987: Map Projections--A Working Manual..US Geological Survey Professional Paper.vol. 1395.

Sørensen, L. S., Simonsen, S. B., Nielsen, K., Lucas-Picher, P., Spada, G., Adalgeirsdottir, G., Forsberg, R., and Hvidberg, C. S.: Mass balance of the Greenland ice sheet (2003 – 2008) from ICESat data – the impact of interpolation, sampling and firn density, The Cryosphere, 5(1):173–186. doi: 10.5194/tc-5-173-2011, 2011.

Sørensen, L. S., Simonsen, S. B., Meister, R., Forsberg, R., Levinsen, J. F., and Flament, T.: Envisat-derived elevation changes of the Greenland ice sheet, and a comparison with ICESat results in the accumulation area, Remote Sens. Environ., 160:56–62. doi: 10.1016/j.rse.2014.12.022, 2015.

Wingham, D. J., Rapley, C. G., and Griffiths, H. D.: New techniques in satellite altimeter tracking systems. Proceedings of the IGARSS Symposium, Zurich SP-254, European Space Agency, September 1986. Edited by T. D. Guyenne and J. J. Hunt.